THE FORMATION AND EVOLUTION OF THE STOCKTON ISLAND TOMBOLO,

REFINED BY OSL GEOCHRONOLOGY

A Thesis
Submitted to the Graduate Faculty
of the
North Dakota State University
of Agriculture and Applied Science

By

Sara Skye Gibbs Schnucker

In Partial Fulfillment of the Requirements
for the Degree of
MASTER OF SCIENCE

Major Program:
Environmental and Conservation Sciences

November 2022

Fargo, North Dakota

North Dakota State University
Graduate School

Title

THE FORMATION AND EVOLUTION OF THE STOCKTON ISLAND
TOMBOLO, REFINED BY OSL GEOCHRONOLOGY

By

Sara Gibbs Schnucker

The Supervisory Committee certifies that this ***disquisition*** complies with North Dakota

State University's regulations and meets the accepted standards for the degree of

MASTER OF SCIENCE

SUPERVISORY COMMITTEE:

Dr. Ken Lepper

Chair

Dr. Stephanie Day

Dr. Anthony Flood

Approved:

November 18, 2022

Date

Dr. Craig Stockwell

Department Chair

ABSTRACT

Past research conducted on strandplain sequences has shown strandplains can record Holocene lake level changes. The Stockton Island tombolo, of the Apostle Islands National Lakeshore, holds such a record within its eastern and western strandplains; however, its data is at risk of being erased due to its position in a region of subsiding glacial isostatic adjustment. The objectives of this study were to provide geologic dates to evaluate the formation and evolution of the tombolo, as well as assess an apparent truncation of the western strandplain by the eastern. 19 samples were collected along transects from ridges within each strandplain. Samples were dated using Optically Stimulated Luminescence (OSL) techniques. These age results will provide useful geochronological context for future ecological and archaeological research on the tombolo; they will also provide a more robust understanding of past lake level variations which may enhance public education on water resources and climate change.

ACKNOWLEDGEMENTS

readiness to celebrate my successes, and thank you to my late Grandpa Bob who was beyond proud of me for continuing my academic career. He never was quite sure what I was studying, and would often tell family members that I was getting my Ph.D. in archaeology – I will delight in this precious misconception, and I hope he won't be too disappointed to learn that I am, in fact, not studying anything related to humans.

I would like to dedicate my final acknowledgement to my partner, Parker John. He has been my greatest cheerleader and my strongest confidant. He has endured significant vicarious stress as he's watched me experience graduate school, and he has never ceased to advocate for my intelligence or capabilities. I attribute a great deal of my success to his encouragement and the grace with which he has shown me love, kindness, and undying support. I would never have been able to go as far as I have without him by my side. Thank you, Parker, you have contributed more than you will ever know.

TABLE OF CONTENTS

LIST OF TABLES

LIST OF FIGURES

LIST OF APPENDIX TABLES

LIST OF APPENDIX FIGURES

1. INTRODUCTION

Stockton Island is one of several islands present within the context of the Apostle Islands National Lakeshore, in Lake Superior (Fig. 1A). Approximately 5000 years ago (Booth et al., 2021), a tombolo began forming between Stockton Island and a smaller body near its shore named Presque Isle (Fig. 1B). As more sediment was deposited and the tombolo's topography began to evolve two strandplains, constructed of a series of beach ridges with intervening swales, were formed bracketing the eastern and western aspects of the landform. Strandplains can serve as useful tools to understanding Holocene lake level changes; however, the Stockton Island tombolo's strandplains may eventually be submerged underwater. Research conducted by Thompson et al. (2014) suggests the glacial isostatic adjustment near the Apostle Islands National Lakeshore is at a negative rate of approximately -1 to -3cm/century. If the Stockton Island tombolo is submerged, the geologic record its strandplains hold will be erased. By dating the eastern and western strandplains, the currently preserved record of tombolo evolution may be understood and interpreted.

This research focuses on dating the Stockton Island tombolo strandplains using Optically Stimulated Luminescence (OSL) dating techniques. OSL dates the time since deposition of quartz grains by measuring the amount of light that is given off following natural and laboratory applied radiation. In contrast to radiocarbon dating, OSL offers a dating technique that allows data to be collected from a sequence of beach ridges, regardless of the presence or condition of organic matter in the swales, unless the sequence is topographically interrupted (for example, by water or a lack of visible ridge and swale topography).
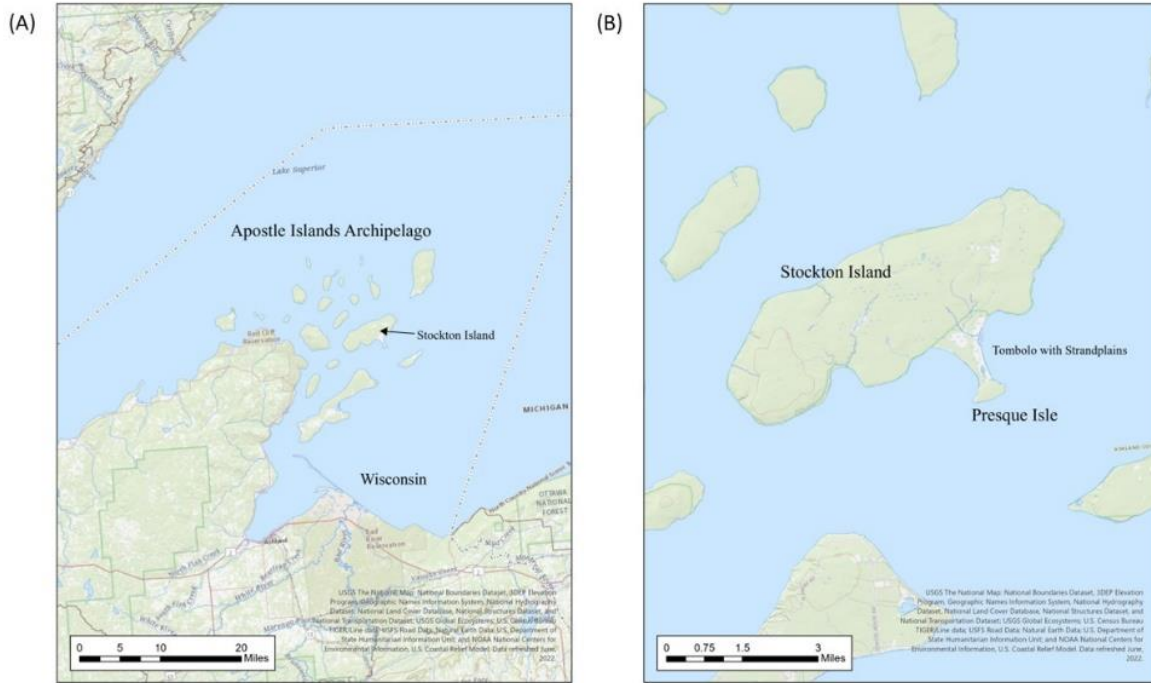
Figure 1. Project site location. (A) USGS topographic map with a scale of 1:500,000 showing the location of Stockton Island within the Apostle Islands Archipelago. (B) USGS topographic map with a scale of 1:80,000 showing Stockton Island and Presque Isle connected by the Stockton Island tombolo. (USGS. "TNM Topo Base Map" [basemap]. https://basemap.nationalmap.gov/arcgis/rest/services/USGSTopo/MapServer

In developing the objectives for the project, there were two primary questions that were considered foundational to resolve. The first involved the evolution of the tombolo and what geologic and/or hydrogeologic circumstances led to the western strandplain's truncation by the eastern. Tombolos more typically form in a symmetrical pattern, so the truncation visible both topographically and on Lidar images suggests the depositional pattern of the beach ridges was altered. The second was a broader inquiry as to whether the ridge with the highest elevation, present along the eastern strandplain, would correlate to a high water level event called the Nipissing phase of the Great Lakes. The Nipissing phase resulted in a distinct shoreline feature that may be seen throughout the Great Lakes region. If the Stockton Island tombolo recorded this

event in its beach ridges, then the tombolo could be correlated to other Great Lakes strandplain sequences, further contributing to the knowledge of Holocene lake level change.

The objective of this research is to investigate the previously mentioned guiding questions to provide geochronological constraints for the Stockton Island Tombolo before the geologic record of the tombolo is erased by increasing relative lake levels. In addition, the chronology will benefit archaeological work by providing an age framework for the strandplains, which include various sites of Indigenous activity. This work may also be useful in enhancing public education relating to water resources, hydrologic processes within the Great Lakes, and climate change.

2. LITERATURE REVIEW

2.1. Geologic History of the Apostle Islands

2.1.1. Deep Time History

The Lake Superior basin area contains some of the oldest rock formations in North America (Thornberry-Ehrlich, 2015). The history of these rock types provides context for the active sediment present along the Apostle Islands National Lakeshore.

Beginning in the Archean Eon, specifically between 3.5-2.6 billion years ago, granites, gneisses, and volcanogenic sedimentary rocks were deposited as a continental margin assemblage of the Superior Province (Figure 2; Schultz and Cannon, 2007). By the Paleoproterozoic era, approximately 2.3 billion years ago, this margin collided with an oceanic arc which created a subduction zone, resulting in the accretion of magmatic bodies and sulfide deposits. A pause in the subduction zone's activity allowed an ocean to form (Figure 2; Schultz and Cannon, 2007). From 1.88 billion years to approximately 1.85 billion years ago, the combination of a shallow marine environment, sulfide deposits, and oscillating O_2 concentrations in the atmosphere contributed to the creation of the banded iron formation; iron-rich strata were deposited in thin beds, laminated between quartz-arenite, conglomerates, dolomite, and quartz-rich siltstones (Figure 2; Schultz and Cannon, 2007; Morey and Southwick, 1995). Following this depositional period, 1.85 billion years ago, the Superior Province's continental margin shifted to a compressional phase, which accumulated formerly independent microcontinents and created Laurentia, the North American craton (Figure 2; Schultz and Cannon, 2007). This also marked the end to the first of a three-stage sequence: an intracratonic basin, followed by a rift stage, and finally, a post-breakup stage (Morey and Southwick, 1995). A geologic timescale is available in Appendix A to aid in the following discussion.
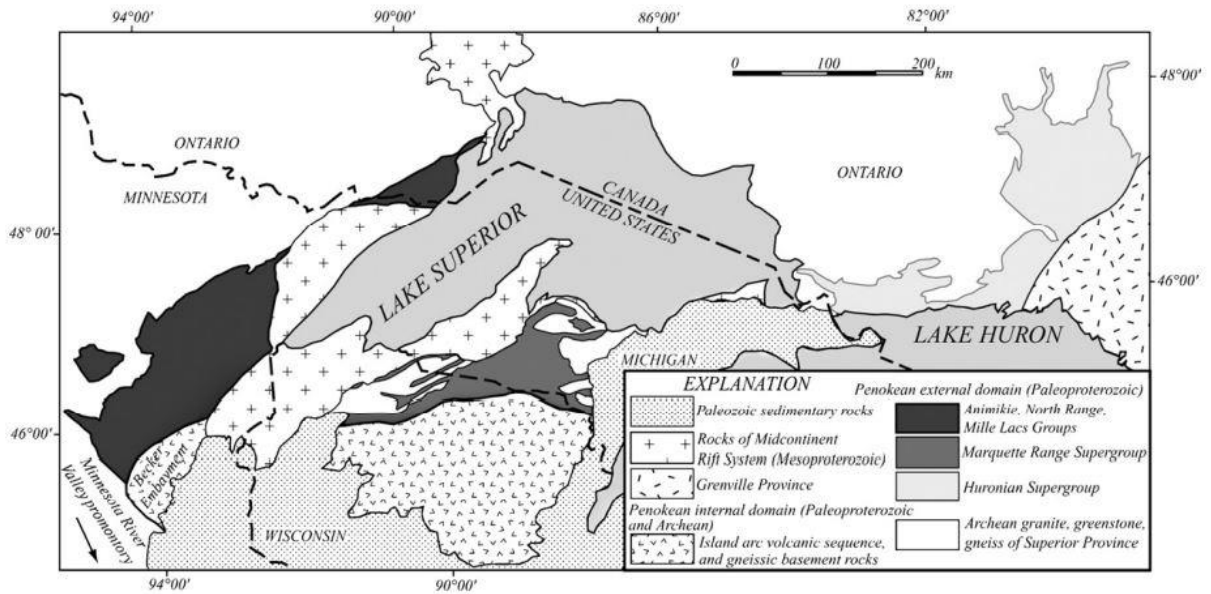
Figure 2. Geologic map showing a Paleoproterozoic distribution of volcanic and sedimentary formations related to the continental margin (Schultz and Cannon, 2007).

Approximately 1.1 billion years ago, Laurentia began to rift apart, commencing the second stage of the sequence. A rising mantle plume, caused by widespread magmatism, breached the continually thinning continental crust (Fairchild et al., 2017; Thornberry-Ehrlich, 2015). This process created the midcontinental rift. After approximately 25 million years (Fairchild et al., 2017), the rift failed, leaving behind the Lake Superior Basin (Thornberry-Ehrlich, 2015). The magmatic formations of the exposed mantle plume may be seen today as bluffs and rocky beaches along the shores of Lake Superior.

By 1.086 billion years ago, the midcontinental rift's tectonic activity ceased, beginning the third and final stage of the sequence. The basin floor began to depress, and the external margins of the rift subsided, which eroded the exposed magmatic formations. This, coupled with stream activity, supplied the basin with sediment that was then deposited in thick sedimentary layers (Thornberry-Ehrlich, 2015).

2.1.2. Regional Lithology

There are three main categories of rocks in the Lake Superior basin area. First are the quartz sandstones and iron-rich strata that formed during the Paleoproterozoic era. Second are the 1.1 billion-year-old igneous rocks from the failed midcontinental rift that formed massive bodies of basalt, gabbro, and granite (volcanic and intrusive rocks in Fig. 3).
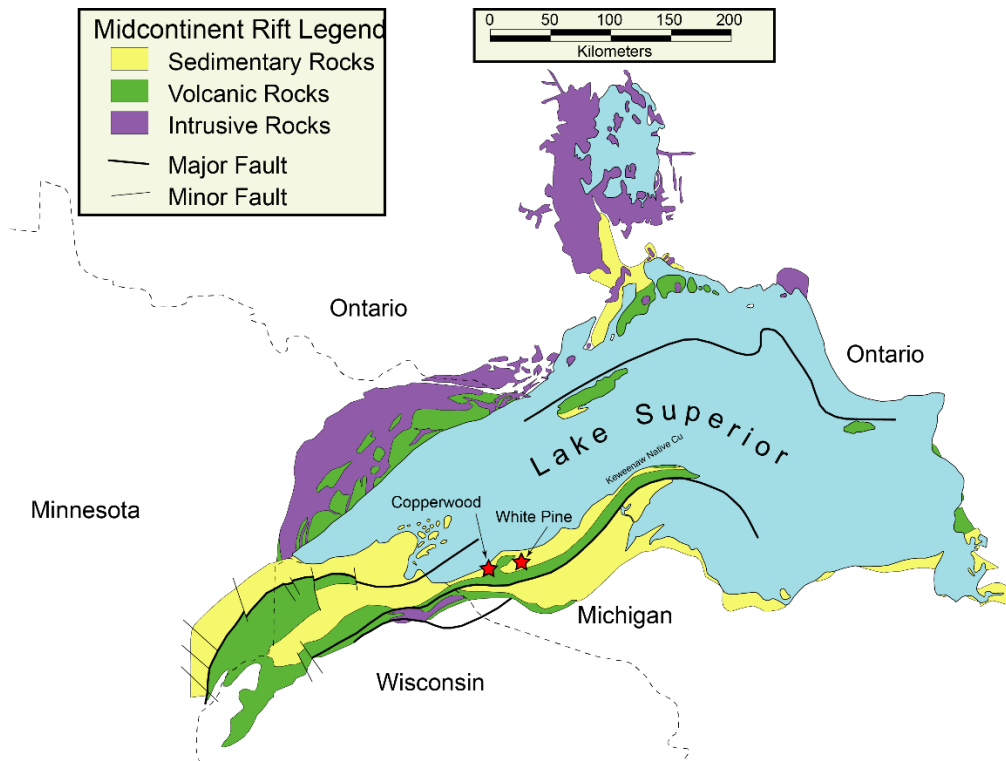
Figure 3. General geologic map of Lake Superior showing bedrock near and around the shores of present-day Lake Superior (USGS, 2019).

Third are sedimentary rocks that formed following the rifting event (sedimentary rocks in Fig. 3) (Ojakangas and Matsch, 1982). Approximately 1.0 billion years ago, chemical and physical weathering began eroding the exposed granite (rich in feldspar and quartz) formations. Since feldspar is less durable than quartz, its available concentration decreased relative to quartz, resulting in heavily quartz-dominated sediment. The eroded rift sediment lithified, creating the

Bayfield Group of sedimentary rocks (Fig. 4). This group includes the Orienta Sandstone, the

Devils Island Sandstone, and the Chequamegon Sandstone (Thornberry-Ehrlich, 2015;

Ojakangas and Matsch, 1982). The Devils Island Sandstone, a fine-grained, nearly pure quartz

formation, is prominent throughout the Apostle Islands National Lakeshore (Thornberry-Ehrlich,

2015).

Age			Map Unit (Symbol)	Geologic Description
MESOPROTEROZOIC ERA	Keweenawan Supergroup	Bayfield Group	Chequamegon Sandstone (PCch)	Arkose is a feldspar-rich sandstone. PCch contains red, brown, and white arkosic sandstone. Scant beds of red shale and conglomerate occur locally. Feldspar grains are common. Sedimentary bedding is generally thick. PCch is about 150 m (490 ft) thick. PCch dominates the bedrock within the park, and is mapped on all islands except Eagle, Sand, and Devils.
			Devils Island Sandstone (PCdi)	PCdi consists of white to tan quartz sandstone arenite (consolidated sedimentary rock composed of sand-sized fragments). Individual beds within PCdi are generally thin. PCdi is about 100 m (330 ft) thick. PCdi crops out at Devils and Sand islands, and along the shoreline in the mainland unit of Apostle Islands National Lakeshore.
			Orienta Sandstone (PCo)	Arkose is a feldspar-rich sandstone. PCo is red, brown, and white, arkosic sandstone. Scant beds of red shale and conglomerate occur locally. Feldspar grains are common. PCo is approximately 1,000 m (3,300 ft) thick. PCo is mapped at Eagle and Sand islands.
		Oronto Group	Freda Sandstone (PCf)	PCf contains fine- to medium-grained, red, brown, and tan sandstone arenite (consolidated sedimentary rock composed of sand-sized fragments) with lesser shale and conglomerate layers. Feldspar and mica flakes are common. Bedding is well defined. PCf is not mapped within Apostle Islands National Lakeshore.

Figure 4. Stratigraphic units of sedimentary formations present on and near the Apostle Islands National Lakeshore (modified from Thornberry Ehrlich, 2015).

A disconformity exists between the Precambrian bedrock and sedimentary formations,

and the igneous, metamorphic, and eventual sedimentary, formations that were deposited

following the midcontinental rift. This is due to millions of years of erosion by ancient streams and Pleistocene glacial activity. Subsequently, this erosion left behind hills of exposed bedrock and durable quartz sandstone features that would continue to be sculpted into the present-day Apostle Islands (Thornberry-Ehrlich, 2015).

2.1.3. Glacial History and Glacial Isostatic Adjustment

Like deep time history, Pleistocene glaciations contributed to the geological context of the Lake Superior region. Their lingering effects play a significant role in crustal behavior and relative lake level in and around the Apostle Islands National Lakeshore.

During the Pleistocene Epoch, 2.5 Ma-10 ka, the Laurentide Ice Sheet (LIS) covered approximately half of the North American continent, with various ice lobes extending as far north as the Arctic Circle and as far south as Missouri and Kansas (Fig. 5) (Ojakangas and Matsch, 1982). The epoch itself was dominated by alternating cold and warm periods. This allowed the massive glaciers to traverse the continent in numerous successions of glacial advances and retreats (Thornberry and Ehrlich, 2015).
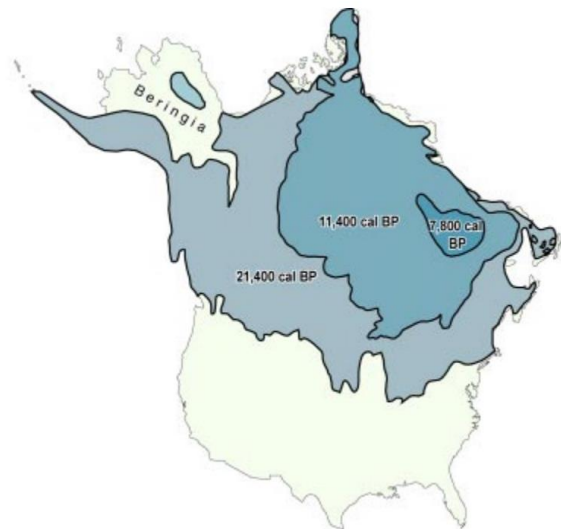
Figure 5. Map showing the extent of the Laurentide Ice Sheet at various times in the past (Payette et al., 2002).

Approximately 15,000 years ago the annual mean temperature of the earth rose, and the LIS began melting faster than snow could accumulate. The last glacial advance over the Apostle Islands occurred approximately 12,300 years ago (Thornberry-Ehrlich, 2015). It was followed by further climate warming, which resulted in the southernmost lobes retreating to Canada (shown through the color gradient and shifting boundaries in Fig. 5). In their wake, they left a large volume of glacial meltwater in the Lake Superior basin. This formed a series of short-lived glacial lakes which, by 12,000 years ago, coalesced into Lake Duluth (Fig. 6). Approximately 10,000 years ago, the last remaining lobe retreated, and the Great Lakes region was no longer covered by ice (Ojakangas and Matsch, 1982).
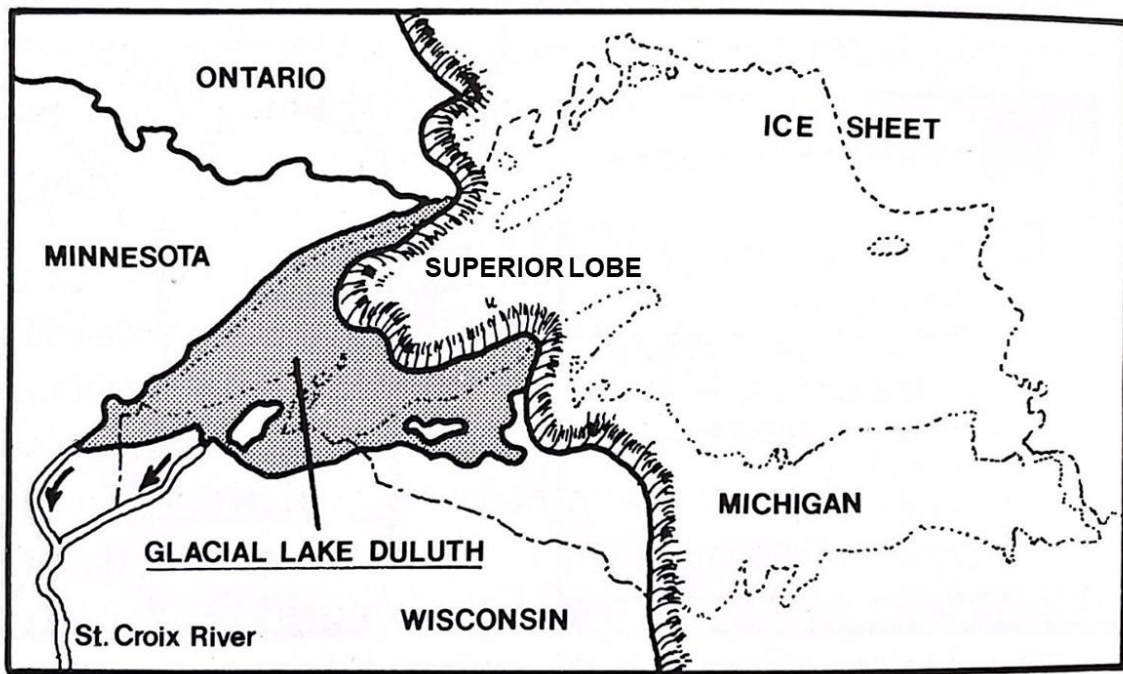
Figure 6. Map locating Glacial Lake Duluth and its proximity to the Superior Lobe, a lobe associated with the Laurentide Ice Sheet (modified from Ojakangas and Matsch, 1982).

As glaciers move, they scour the earth's crust and leave behind glacial till which is eroded and redeposited sediment that may range in size from clay to large rocks and boulders. In the Lake Superior basin area, the LIS eroded bedrock from the Canadian Shield and sedimentary

9

formations like the Devils Island Sandstone. Along with stream erosion and other lake processes, the till associated with the LIS contributed much of the sediment found on the contemporary shorelines of Lake Superior (Ojakangas and Matsch, 1982).

Glacial isostatic adjustment (GIA) occurs following crustal compression from glaciers (Sella et al., 2007). When a glacier is present, its mass compresses the Earth's lithosphere and asthenosphere (crust and upper mantle). Thus, once it has receded, the lithosphere may move upward again, restoring isostatic equilibrium (Huggett, 2011). This movement follows the directional trend of the glacier's mass (Fig. 7), showing rebound as vertical movement in a gradient.
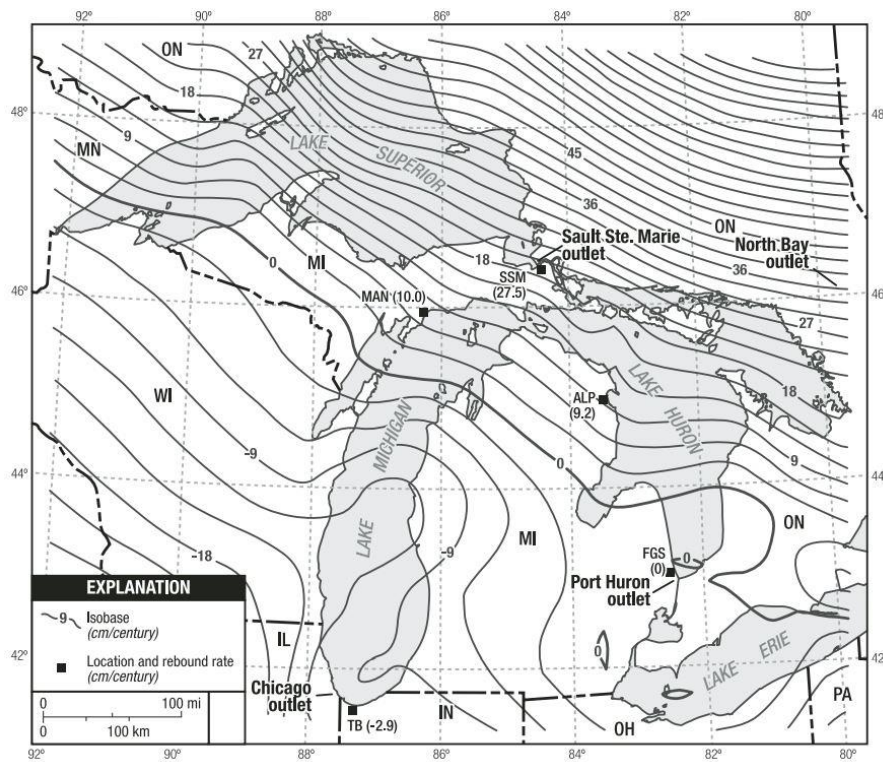
Figure 7. Map indicating the present day regional rates of glacial isostatic adjustment near and around the Great Lakes Region (Thompson et al., 2014). Negative isobase lines indicate areas of crust that are currently subsiding.

Approximately 12,000 years ago (Sella et al., 2007), when the smaller glacial lakes joined and created Lake Duluth, the LIS overlaid the northern portion of the Lake Superior basin with up to 3km of ice (Mainville and Craymer, 2005). This caused the southern part of the basin to rise, making water drain into Ontario. Once the ice completely retreated, exposing the Great Lakes region entirely, GIA began correcting the tilting effect caused by the ice. Currently, it is causing the northern shore of Lake Superior to rise while the southern shore is sinking, rebounding at a negative rate. As shown in Figure 7, the Apostle Islands are currently moving approximately -1 to -3 cm/century (Thompson et al., 2014). This means the Stockton Island tombolo's Holocene record may eventually be submerged underwater and destroyed by erosive lake processes. In fact, some of the shoreline record is already experiencing partial submersion, resulting in large marshes on either side of the tombolo.

2.1.4. Lake Level History of Lake Superior

When Glacial Lake Duluth formed, its northern portion was pocketed between the southern margin of the Lake Superior basin and the last lobe to have affected the area, the Superior Lobe (Fig. 6). The water level had elevations of 323-335 m and existed for a few thousand years before its drainage system emptied its water level to 60 m below present-day Lake Superior (Ojakangas and Matsch, 1982). Following this low water stage, the lake level rapidly increased until approximately 6000 years ago. Between 6000 and 4500 years, the lake level rose more gradually to a peak level; this level is called the Nipissing phase (Thompson et al., 2014).

The Nipissing phase was the last pre-modern high-water stage of the Great Lakes and dates to 4500 years ago (Thompson et al., 2014; Thompson et al., 2011). When Lakes Michigan, Superior, and Huron were connected, the Nipissing's high water elevation left a prominent beach

ridge throughout the system that is presently recognizable topographically. Following its steady

rise, the water level fell drastically over the next 500 years and was succeeded by more phases

(Thompson et al., 2014). Figure 8 shows that the Algoma phase occurred from 2800-2000 cal.

BP, the Sault phase from 2000-1000 cal. BP, and the sub-Sault phase from 1000 cal. BP to

present-day (Johnston et al., 2012).
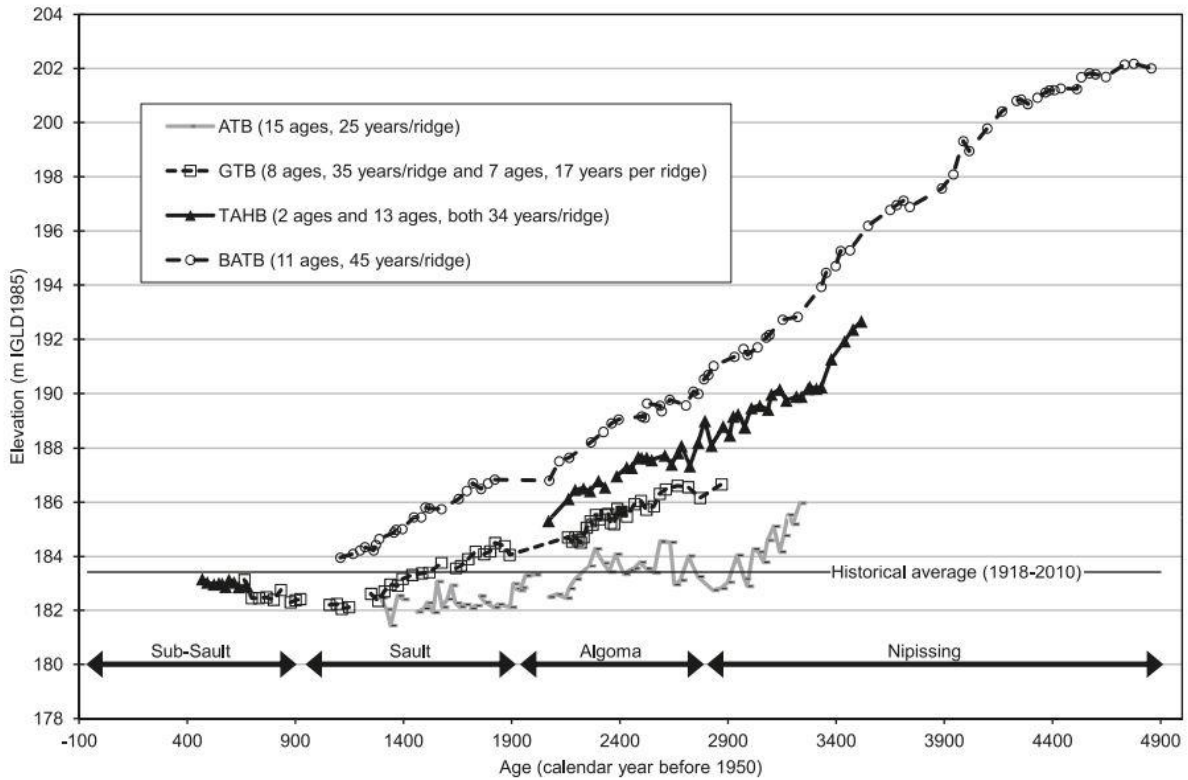
Figure 8. Paleohydrograph showing trends observed at four different locations, relative to the Sault outlet in Lake Superior. Trends support previous literature related to the identification of four lake level phases, the Nipissing, Algoma, Sault, and Sub-Sault phases (Johnston et al., 2012).

2.2. Shoreline Processes and Features

2.2.1. Tombolos, Strandplains, and Strandplain Internal Architecture

Beach ridges, and their formation and evolution, differ depending on water level change

and available sediment supply. Since this study focuses on dating beach ridges, it is imperative to

understand their basic architecture, potential variations, and the conditions from which they may form.

Beach ridges are "curvilinear ridges of sand that are parallel or sub-parallel to the modern shoreline." (Baedke et al., 2004). Constructive waves transport sediment shoreward and deposit it at the water's edge (the swash zone) (Huggett, 2011). This deposition zone, called the foreshore (Fig. 9), shows paleo-water level elevations. These sediments are mixed by wave activity before they are deposited beneath other sediment. This mixing increases the likelihood of charge trap resetting (explained further in Section 2.3.1.), which makes foreshore deposits potentially optimal for OSL dating. They also demarcate the sediments last exposed to light in the swash zone; after they are deposited and other sediments cover them, they begin to record their exposure to ionizing radiation.
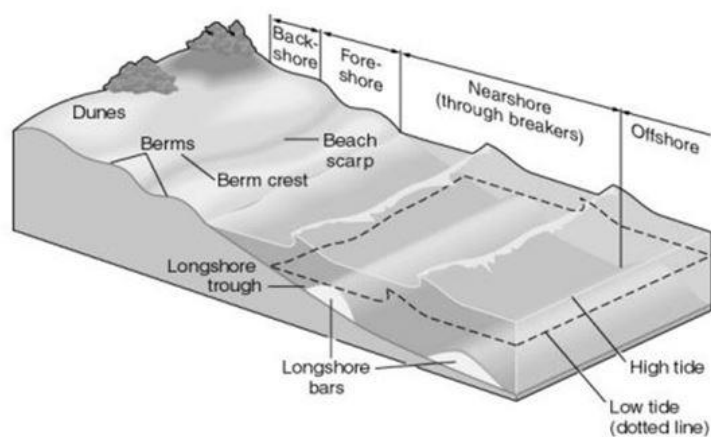
Figure 9. Diagram showing the different zones of a shoreline, including shoreline features and their associated areas of deposition (© 2002 Brooks/Cole a division of Thomson Learning, Inc.).

As the sediment in the foreshore accumulates, a berm is created. Berms are the most inland point of a beach, marking the landward limit of wave activity (Huggett, 2011). Waves will continually wash more sediment to shore, contributing to the berm, and as the water level drops, this build-up will expose a fully formed beach ridge, indicative of where the water's edge

(foreshore) used to be (Huggett, 2011). Thus, once beach ridges develop, and unless erosion

destroys them, they will record paleo-lake levels. Strandplains are a collection of closely spaced

beach ridges and intervening swales that form in embayments of the shore (Huggett, 2011).

Tombolos (Fig. 10) "are wave-built ridges of beach material [sand] connecting islands to

the mainland or islands to islands." (Huggett, 2011). Like beach ridges, their initiation begins

with a transport of sediment; waves refract around the smaller island and converge, depositing

sediment between the two landmasses. If shoreline dynamics favor strandplain development,

then the sediment builds up, first creating the foundation of the sand bar in the center and then

building beach ridges outward; these will eventually form two sets of strandplains that will shape

the outer boundaries of the tombolo.
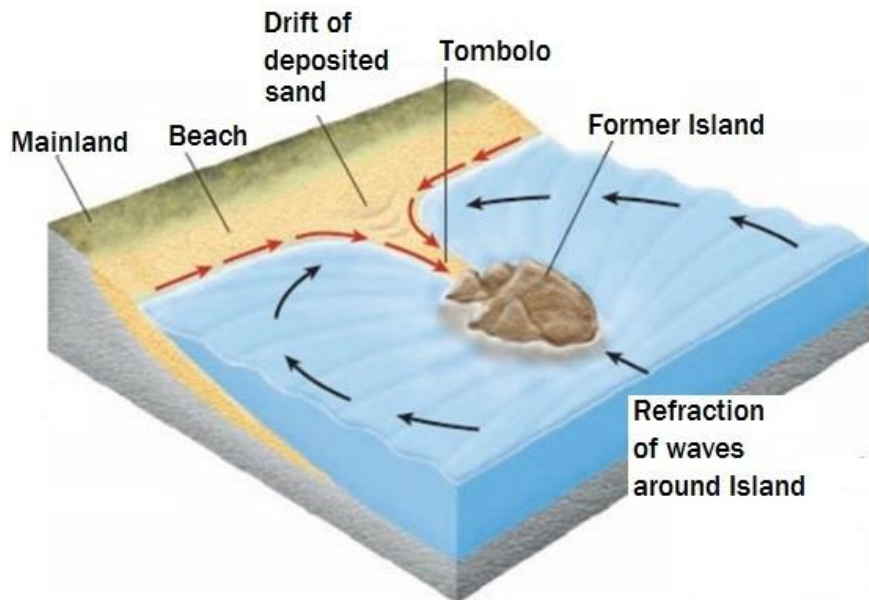
Figure 10. Diagram showing the causal relationship between wave refraction around a smaller island, and the formation of a tombolo between that smaller island and a nearby larger body (https://www.geocaching.com/geocache/GC7ZB60_grotta-tombolo-d-leslie-a-122?guid=10674dc5-bef5-4b6d-8218-9d0c6d7834ca, accessed 10-20-21).

As shown in Figure 11 from Thompson and Baedke (1995), there is an interaction between the rate of water level change and the rate of sediment supply, which results in variations of beach ridge internal architecture. If the rate of water level change decreases while the sediment supply is high, then a beach ridge will form, with a second forming on its lakeward aspect; this is called progradation (Fig. 11) (Thompson and Baedke, 1995). If the water level itself rises while the sediment supply remains the same or decreases, the wave action will erode any ridges in contact with the water; in contrast, a relative rise in water level with a high or increase in sediment supply will allow ridges to form, stacking the newest on top of the oldest while moving farther inward (landward); this is called a depositional transgression (specifically along or above the aggradation line in Fig. 11).
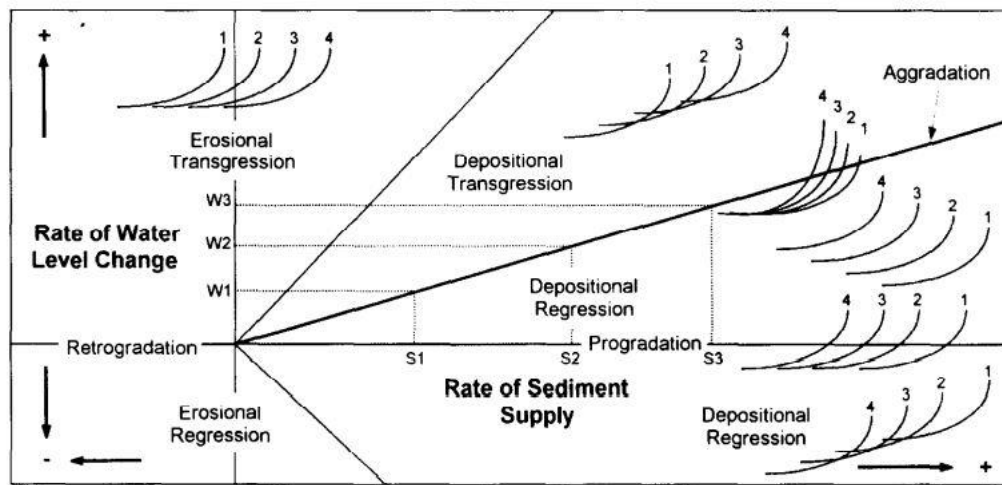
Figure 11. Curray (1964) diagram showing the varying shoreline behaviors that can occur depending on the rate of sediment supply and the rate of water level change (from Thompson and Baedke, 1995).

GIA can also influence beach ridge formation. In areas where the rate of GIA is positive, the water level will appear to be falling, and where GIA is negative, the water level will seem as though it is rising. This shows that as water level affects the placement of the beach ridge, GIA can affect water level, which in turn also affects beach ridge placement.

15

Aside from influencing active beach ridge formation, GIA can impact beach ridge paleo-records by superimposing vertical movement onto the crust after the ridges have formed (Johnston et al., 2012). To develop paleohydrographs that show the true lake level change, GIA must be subtracted from the elevation of the strandplain sequence. This results in a residual lake level curve, which can then be used to correlate dates of phases to accurate lake level elevations (Baedke and Thompson, 2000), such as Figure 8 from Johnston et al. (2012) in section 2.1.4.

2.3. Optically Stimulated Luminescence (OSL) Dating

2.3.1. Basic Concepts of OSL

Optically stimulated luminescence is based on principles of solid state physics. First, a quartz crystal's parent rock erodes before being transported from its original formation (Fig. 12). Once deposited, the crystal is exposed to environmental radiation (which is proportional to time after deposition).
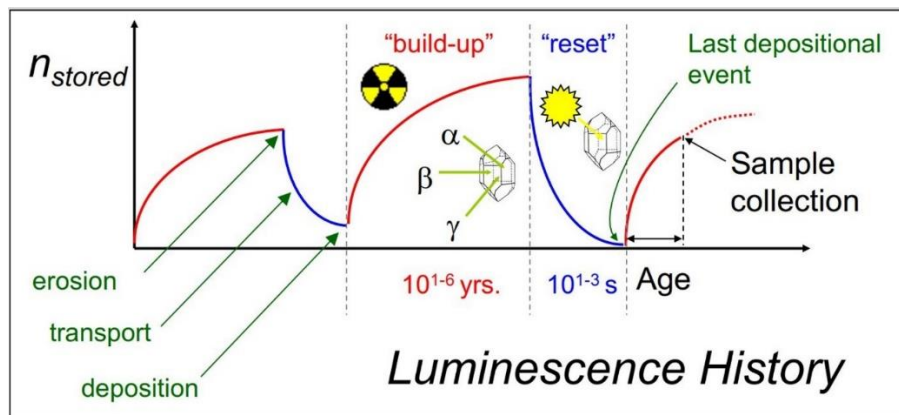
Figure 12. Diagram showing the response of a quartz grain before, during, and after environmental irradiation (modified from Lepper, 2001).

In a perfect setting, the crystal would have no impurities or defects within its mineral matrix. However, in nature, this is never the case. The defects act as traps for electrons. This can be represented in a band gap diagram (Fig. 13), where ionizing radiation (alpha, beta, and gamma) imparts electrons with enough energy to separate from their original (ionized) atom and

16

move from a valence band to a conduction band ("build up" stage in Fig. 12; Fig. 13A). In the

conduction band, electrons can move in physical space, although not indefinitely. The electrons

encounter traps, where they may remain until the charge traps are saturated or stimulated by light

or heat (Fig. 13B).
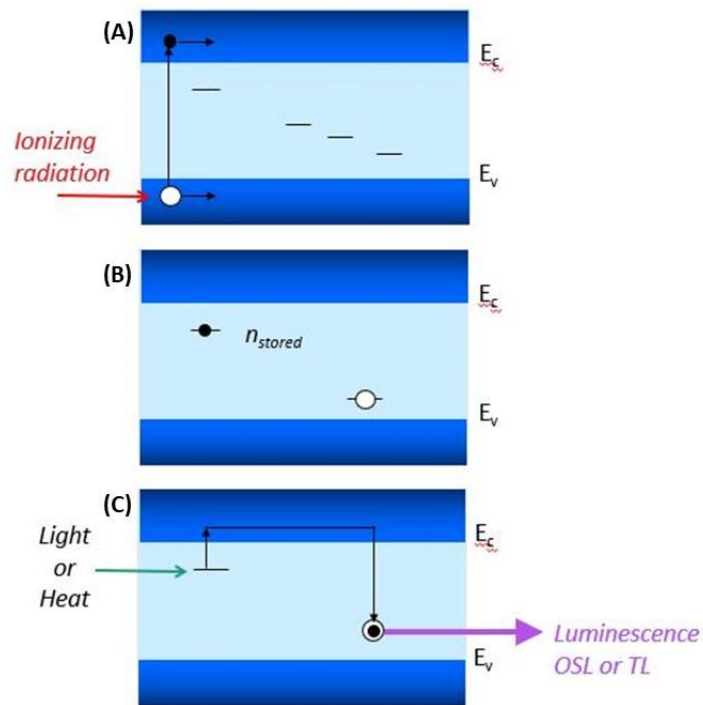
Figure 13. Band gap diagram. (A) An electron, separated from its original ionized atom, moves from the valence band to the conduction band. (B) This electron fills a trap within the band gap where it will remain until stimulated by light or heat. (C) The electron moves back into the conduction band, where it can then recombine with an ionized atom. Once combined, the atom will become excited but will then relax, releasing energy in the form of light (modified from Lepper, 2001).

Upon this stimulation, the electrons have enough energy to move back into the

conduction band, where they will then be able to recombine with an ionized atom (Fig. 13C).

Joined, the electron and ionized atom form an excited state. In the process of relaxing from its

excited state, the atom will release energy in the form of a photon (light) before settling into the

valence band (Fig. 13C). The intensity of the emitted light is proportional to the number of filled

traps within the crystal; the more intense the light, the longer the crystal, and thus the sample, has

been buried.

Following its release of photons, the crystal's traps will be reset ("reset" stage in Fig. 12).

As shown in Figure 12, the resetting stage ends as the next depositional phase begins. The crystal

is once again buried, and electrons begin to refill the now empty traps. If a crystal is exposed to

less light or heat than what is necessary to complete its resetting, then its charge traps will be

only partially reset (this is common in sediment deposited in littoral settings). If an incompletely

reset crystal is reburied and its traps are refilled, the prior partial resetting will result in an

overestimate of time since deposition. This will be discussed further in Section 2.3.2.

In its simplest form, the equation used to find an OSL age is

$$t_{osl}=D_e/D' \qquad\qquad [Eq.1]$$

where t_{osl} is time since deposition, D_e is the equivalent dose (Grays), and D' is the dose rate

(Grays/year). The equivalent dose is determined from the amount of light that a sample emits

following laboratory measurements. However, it is not directly representative of a sample's age.

To calculate a true age, the amount of environmental radiation must be known. This is

represented as the dose rate, which is the rate at which a crystal is irradiated by naturally

occurring radioisotopes of K, Rb, U, and Th, as well as cosmic rays (Duller, 2008; supplement to

Lepper et al., 2007).

2.3.2. Single Aliquot Regeneration Procedure

When the energy from an ionized atom is released, the crystal's dosimetric properties

may be altered within a predictable range. This is called a sensitivity change, and when OSL was

first invented, an aliquot (a 1 cm diam. stainless steel disk that contains the crystals) could only

be exposed to applied radiation once, which further means its emitted light could also only be

measured once. Multiple rounds of applied radiation, on separate aliquots, were necessary to measure a D_e, and it took 40-48 aliquots to calculate one age (Lepper, K., *pers. comm.*). Single Aliquot Regeneration (SAR) procedures account for quartz' sensitivity change via experimental correction so that an age can be determined from one individual aliquot (Murray and Wintle, 2000; Wintle and Murray, 2006). SAR gives a larger D_e data set, which provides better statistics and allows for the analysis of a D_e distribution (Duller, 2008; supplement to Lepper et al., 2007; Lepper et al., 2000).

SAR uses regenerative (regen) doses of applied radiation to construct a calibration curve for each aliquot (Fig. 14); this calibration curve is then used to determine the equivalent dose for each aliquot of a sample. First, the natural signal is measured, followed by a measurement of a signal from a uniform test dose. The first data point in the calibration process is from the natural signal divided by the test dose signal ("N" in Fig. 14). Then, regen doses are applied to the same aliquot in four stages, with each dose increasing incrementally. A test dose is given between each regen dose so that the final data set is comprised of ratios (Murray and Wintle, 2000; Wintle and Murray, 2006). Once the fourth regen dose has been administered and measured, a check dose is given ("C" in Fig. 14), followed by a final test dose. The check dose is the mean of the applied regen dose values (Lepper et al., 2000). Plotting these ratios creates an aliquot's calibration curve (Fig. 14). Each aliquot has its own calibration curve, which means it also has its own D_e value.
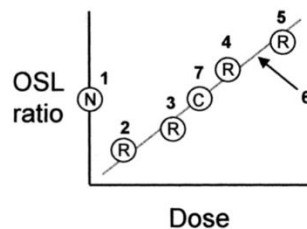
Figure 14. SAR calibration curve of one aliquot. "N" is the natural signal divided by the test dose signal. "R" are different regenerative doses that increase with each dose. "C" is a check dose administered following all regenerative doses (Lepper et al., 2000).

Once a D_e data set has been collected for a sample, its mean D_e (M) and median (m) are determined as a gauge of the distribution's symmetry or asymmetry, which in turn indicates which of two analytical approaches may be most appropriate for further calculations. The mean median ratio (M/m) is determined from a sample's distribution (D_e data set). If the distribution is symmetric (0.95-1.05), then the mean D_e and its standard error are appropriate for calculating an age. However, if the distribution is asymmetric (1.10 or higher), then an approach called Leading Edge (D_{LE}) must be used to determine the sample's representative D_e and appropriate error (supplement to Lepper et al., 2007).

As introduced in Section 2.3.1., if a crystal's traps are not entirely reset, then calculating a sample's age with its mean D_e would result in an overestimate of actual time since deposition. Mathematically, partial resetting is represented in a sample's M/m distribution as positively asymmetric (as noted above, 1.10 or higher). Leading Edge analysis corrects for this asymmetry, which lowers the calculated age of a sample to its accurate age range. If a sample's M/m is between 1.05 and 1.09, then its distribution is within a "gray zone." In cases where a sample falls within the gray zone, its age is calculated using both its mean D_e and Leading Edge representative D_e. The two results are then compared to the entire data set of collected field samples, and the age that aligns most consistently within the sample's geologic context is used (supplement to Lepper et al., 2007; Lepper, K., *pers. comm.*).

2.4. Previous Application of OSL in the Great Lakes Region

2.4.1. Studies in Lake Superior

Argyilan et al. (2005) evaluated the accuracy and precision of OSL and radiocarbon (C^{14}) techniques in dating Lake Superior strandplain sequences. They discussed how hydrophilic plants grow well in ridge and swale topography since groundwater typically accumulates in

between the swales. These plants become peat, which can be dated using C^{14}; however, C^{14} ages do not always show consistent results, and the occurrence of organic material is unreliable. OSL offered their study a more appropriate alternative. They also discussed the benefits of eolian systems in relation to charge trap resetting, explaining that eolian saltation provides the crystals with sufficient sun exposure before re-deposition. Overall, they showed that OSL offers reliable age data, and that it is the appropriate dating technique for Lake Superior strandplain sequences.

By using OSL as a dating technique, researchers are able to create a chronologic record of the evolution of strandplains, since sample collection may be done along a transect. Johnston et al. (2012) created relative paleohydrographs (Fig. 8) from basal foreshore elevations and OSL ages to corroborate new GIA rates with previously calculated rates. By studying ridge and swale topography, and dating strandplain sequences, Johnston and colleagues were able to better understand past water level change in Lake Superior. Furthermore, and similar to Argyilan et al. (2005), Johnston et al. (2012) compared their OSL results to prior data obtained through C^{14} dating of peat. They found that by using OSL, they were able to sample along their site's strandplains, targeting upper foreshore deposits which provided deposition-specific ages.

2.4.2. Studies in the Surrounding Great Lakes (Michigan and Huron)

Argyilan et al. (2014) used OSL to correlate stabilized parabolic dunes to wetland development in the Great Lakes region along the shores of Lake Michigan. In doing so, they succeeded in their two stated purposes. The first was to assess the use of OSL in determining when the landforms stabilized versus their initial deposition. The second was to investigate various sample collection methods and whether there was an impact on the resultant OSL data. They were able to discern between the migration and stabilization of the dunes during eolian activity, and this, coupled with a critical analysis of dune formation in relation to the Nipissing

phase, allowed for a reconstruction of past shoreline behavior which aids in the understanding of paleo-lake level change. Their analysis of different sample collection methods showed that sampling from an exposed stratigraphic profile, as opposed to sampling from cores, had the smallest effect on optical ages. This method will be further described in Section 3.2.

Similar to Argyilan et al. (2014), Thompson et al. (2011) used OSL primarily on Lake Huron shorelines to provide relevant dates during the rise and fall of the Nipissing phase. They successfully constrained ages for various transgressive phases, as well as how many years it took to form strandplain sequences. Additionally, they were able to confirm the age of the Nipissing's peak as 4500 years ago and that the water level subsequently fell more than four meters over the following 500 years. They demonstrate how OSL has applications in dating specific sections of dune and strandplain structures, which can help further define their evolution through time. Finally, their explanation of the rapid rate of water level change following the Nipissing phase provides context to both complete strandplain sequence development, as well as the internal architecture of some of the strandplains present along the Stockton Island tombolo.

3. METHODS

3.1. Selecting Sampling Sites

3.1.1. Preliminary Lidar and DEM Surveys

The overarching goal of this research was to study the Stockton Island tombolo's formation and evolution. To do this, in-field sample collection was necessary. However, before specific site reconnaissance could be conducted, it was crucial to obtain a general understanding of areas appropriate for sampling. Prior to conducting the 2020 site reconnaissance, Lidar images such as Figure 15, were used to determine potential collection sites based on elevation and slope. Figure 15 shows the tombolo's two strandplain sequences present along its eastern and western aspects. Since tombolos begin as sediment deposition in what becomes their center and then build beach ridges outward, the innermost ridges can offer ages that correlate to the initiation of the tombolo's formation. Because of this, the inner ridges of both sequences were selected as imperative collection areas. From there, general transects were identified along the eastern and western strandplains to act as a guiding reference that could be used during site reconnaissance.

Point A in Figure 15 corresponds to an area of low elevation that runs the entire extent of the eastern strandplain. Due to the presence of water in this part of the strandplain, it was assumed that there would be limited access to sampling in that area. Through a review of known geologic and hydrologic features (Booth et al., 2021), as well as an elevation map (Fig. 15) of the tombolo, the transect that was identified for the eastern strandplain accounted for the presence of a lagoon that would interrupt an otherwise sequential collection practice. Two general site areas were selected within a zone called The Barrens, which is an ecological area located along the lakeward aspect of the eastern strandplain (point B in Figure 15). One site was to be along the modern shoreline, and another on the innermost boundary of The Barrens. The intent of these

23

sites was to constrain the initiation age of the formation of The Barrens ecological area, which was of particular interest to the National Park Service (NPS). It also provided an opportunity to collect eastern strandplain samples in a numerical order, as the inner boundary of The Barrens would be the next closest ridge to the ridges exposed immediately adjoining the lagoon.

A feature of particular interest on the eastern strandplain was the ridge with the highest elevation (point C in Fig. 15). This ridge was hypothesized to correlate to the Nipissing phase (Thompson et al., 2014; 2011; see also Section 2.1.4.). Its topographic relief and high elevation were consistent with other topographic features indicative of the Nipissing shoreline present in the Great Lakes region. Based on the Lidar image shown in Figure 15, it appears that the eastern strandplain truncates the western near the southern base of the tombolo near Presque Isle (between points D and F in Fig. 15). The law of superposition would suggest that the western ridges truncated by the eastern strandplain would have been deposited prior to the eastern strandplain's formation. Typically, tombolo strandplain sequences form symmetrically, so this asymmetry led to further questions about the tombolo's evolution. Considering the ridge with the highest elevation is also the innermost ridge of the eastern strandplain (and is clearly seen as the first ridge to truncate the western strandplain), dating it would serve two purposes: first, it would determine whether the Nipissing phase left a topographic signature on the Stockton Island tombolo; second, it should provide further insight to the tombolo's evolution and how the eastern strandplain correlates chronologically to the western.
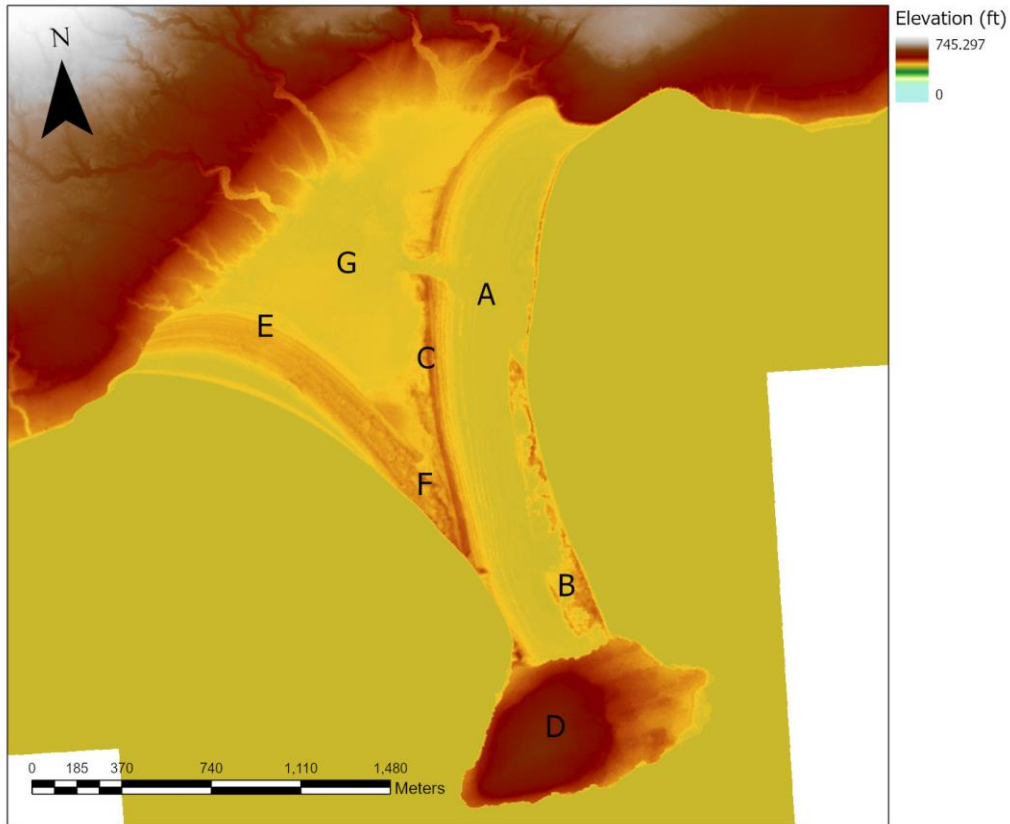
Figure 15. Elevation map of Stockton Island tombolo and Presque Isle. Lidar data from NOAA. (A) The lagoon, an area of low elevation in the eastern strandplain. (B) The Barrens Ecological Area. (C) The ridge with the highest elevation on the tombolo. (D) Presque Isle. (E) Innermost ridge on the western strandplain. (F) Area of hummocky topography in the western strandplain. (G) The bog, an aqueous, low lying, area located in the center of the tombolo.

Since the innermost ridge on the western strandplain (point E in Fig. 15) is both closest to the center of the tombolo and is truncated by the eastern strandplain, the law of superposition, again, would suggest that it is the oldest ridge on the tombolo. To determine whether this is correct, a transect was identified across the broadest part of the western strandplain with the intent of collecting samples from as many ridges in a sequence as possible. Doing so would provide dates that most accurately reflect the western strandplain's chronology. Furthermore, hummocky topography (point F in Fig. 15) is visible where the western ridges are cut off by the eastern strandplain. By choosing sites within the broadest section of the western strandplain,

25

collection efforts would be able to avoid any potential disturbance present near the truncation zone.

Following the 2020 in-field site reconnaissance and collection, the 2021 planning efforts focused on site selection to compensate for specific data gaps or address uncertain results in the 2020 data set. The ridge with the highest elevation (from the eastern strandplain) was of particular interest for this effort. Multiple locations were selected along the highest ridge and the next ridge directly adjoining it to the east. Separately, the NPS was interested in specific regions that could corroborate OSL ages with known archaeological sites. Those locations were included in the 2021 planning and field season.

3.1.2. In-Field Site Reconnaissance

Sites were selected based on relevant geomorphological features (previously discussed in Section 3.1.1.), their proximity to trail access, their distance from trees and thick vegetation, and whether or not they were accessible for digging due to areas influenced by a high water table. Upon arriving at the Stockton Island tombolo in 2020, it was discovered that the primary mode of transportation would be by foot, following two trails that run roughly parallel to the modern shorelines. While some areas were navigable off-trail, the majority of the tombolo was concealed beneath dense vegetation cover that greatly limited mobility. The tombolo's prolific growth of trees was in tandem with the dense vegetation. Because of this, sites were explicitly selected to avoid root systems that may have otherwise inhibited digging.

In the center of the tombolo is a triangular-shaped bog, surrounded on two sides by the strandplain sequences, and Stockton Island on the third side. The bog is at a slightly lower elevation than the strandplains, which allows the water table to influence its geology and vegetation. In the swales between the western strandplain's beach ridges, particularly those near

26

the bog, the water table was higher than what was accessible for sample collection. As will be shown in Section 4.1.1., Figure 16, sample SI2014 was collected along the innermost ridge of the western strandplain. Following SI2014 is a gap where sample collection was not possible due to the high water table.

Other than the highest ridge on the eastern strandplain, the overall relief of the Stockton Island Tombolo is relatively low; this aided in the observation of ridge and swale topography since beach ridges were the primary features that changed in visible relief. Once the lakeward aspect of beach ridges was identified, an auger was inserted at each potential site to ensure the location would allow access to foreshore deposits (see Section 2.2.1. for more details). After a site was selected, a marker was placed, and the site reconnaissance continued until a sufficient sequence of ridges along both strandplains were chosen to be dated. See Table 1 for a full list of all collection site locations.

Table 1. Site locations and related data.

Sample ID	Site Name	UTM's	Latitude	Longitude	Surface Elevation (m)	Sample depth (cm)
SI2007	Barrens West	E 686853 N 5198558	46.914860	-90.546230	185	28
SI2008	Barrens West	E 686853 N 5198559	46.914860	-90.546230	185	77
SI2009	Barrens East	E 686983 N 5198622	46.914787	-90.544377	188.7	98
SI2010	Modern shore - west strandplain	E 685689 N 5199543	46.923430	-90.560979	185.6	75
SI2011	West Strandplain	E 685697 N 5199642	46.924318	-90.560834	186.8	57
SI2012	West Strandplain	E 685704 N 5199666	46.924532	-90.560732	188.0	83
SI2013	West Strandplain	E 685727 N 5199690	46.924741	-90.560421	188.0	67
SI2014	West Strandplain	E 685724 N 5199903	46.926657	-90.560373	185.3	61
SI2015A	East Strandplain	E 686436 N 5199954	46.926916	-90.551000	185.3	49
SI2015B	East Strandplain	E 686436 N 5199954	46.926916	-90.551000	185.3	77
SI2016	East Strandplain	E 686380 N 5199938	46.926788	-90.551750	194.5	72
SI2017	East Strandplain	E 686364 N 5199924	46.926666	-90.551965	194.8	66
SI2018	East Strandplain	E 686334 N 5199944	46.926855	-90.552351	189.6	77
SI2116	East Strandplain	E 686407 N 5199218	46.920303	-90.551684	201.5	55
SI2117	East Strandplain	E 686392 N 5199224	46.920369	-90.551884	199.0	59
SI2118A	Presque Isle knob	E 6866354 N5198440	46.913253	-90.549031	189.6	62
SI2118B	Presque Isle knob	E 6866354 N5198440	46.913253	-90.549031	189.6	107
SI2119A	East Strandplain	E 686441 N 5198978	46.918140	-90.551336	206.7	76
SI2119B	East Strandplain	E 686441 N 5198978	46.918140	-90.551336	206.7	76

3.2. Sample Collection

The optimal dimensions of a sampling pit are 1 m^3; while actual pit sizes varied slightly from site to site, all were approximately consistent with 1 m^3. The upper layer of soil, primarily containing living plants and topsoil, was removed and set aside, as it would be used following pit in-fill to maintain the natural integrity of the sample area. Due to the archaeological significance of the Apostle Islands, each shovel full of sediment was sieved upon excavation by NPS archaeologist using a handheld screen. If any artifacts were identified, the excavation would cease until the NPS archaeologists gave further authorization.

Once a pit was approximately 1m in depth, its sampling face was cleaned using a hand trowel, which allowed for proper visual examination of the soil horizons. Sediment texture and color were then recorded for each horizon. Color was identified using the Munsell Soil Color System. All samples were collected from the B or C soil horizons; this varied depending on the site as foreshore deposits may be found in either. Closed-end metal canisters were inserted horizontally into the wall and sealed using aluminum foil and duct tape after being removed from the profile. Water content was evaluated and recorded from the canister's extraction point. Iron oxide staining was present in many of the pits; this staining was avoided for collection as much as possible. However, one set of samples (SI2119A and SI2119B) was collected intentionally to evaluate the effect, if any, of the iron oxide staining on OSL results.

3.3. Laboratory Chemical Processing

Unprocessed field samples are mixtures of various minerals and organic material. Quartz is the most reliable mineral that can be dated using OSL, so it is imperative that the other materials in the field sample are removed prior to OSL measurement. All samples were processed in the Optical Dating and Dosimetry (ODD) Lab at North Dakota State University.

Since any amount of light could have stimulated the resetting process of the crystals, samples were handled and stored in a light-controlled portion of the lab. Precautions were taken to ensure that light present outside the ODD Lab was unable to infiltrate the processing and OSL measurement rooms, and sodium vapor lamps were used to allow for visibility.

During the in-field sample collection, the upper and lower portion of each sample were exposed to sunlight; the upper was exposed following sample extraction, and the lower was exposed during the sample face analyses. Once in the ODD Lab, the upper one centimeter of each sample was removed, which was then dried at 35˚C. After it was dried, this portion of the sample was sent out for elemental analysis to determine each sample's dose rate (D') (as introduced in Section 2.3.1., this was calculated from U, K, Th, and Rb elemental concentrations). The following two centimeters of each sample were discarded to ensure any sediment used for OSL measurement had not been exposed to sunlight.

Approximately 100 mL of sediment was extracted from the central portion of the container. This was the sediment that had the lowest possibility of light exposure. To obtain fine and medium grain size fractions, sediment was wet sieved. Sieve sizes of 150, 250, and 355 μm were used to separate the size fractions from each other so they could be chemically processed individually. A large body of previous work at the ODD lab has shown that the 150-250 μm size fraction (fine sand) delivers the most accurate results, though the 250-355 μm fraction (medium sand) is retained in case additional measurements are needed.

The first step to obtaining pure quartz was to digest any residual organic material in a 30% hydrogen peroxide (H_2O_2) solution. In time-sensitive situations, this processing may take a minimum of 30 minutes to complete, however the recommended processing time is 24 hours. Between every step, samples were rinsed three times with distilled water; this thoroughly washed

the sediments clean of residual chemical solutions. Next, they were processed in a 10%

hydrochloric acid (HCl) solution to dissolve any carbonate minerals. The samples were then

ready to process in hydrofluoric acid (HF). HF etches off the outer 5 μm of each grain, removing

the layer that holds alpha radiation, which is not desirable for OSL age measurements. Etching

this layer exposes the internal portion of the grain that best releases UV light once stimulated.

HF also dissolves feldspars and any minerals other than quartz.

The samples were rinsed again in HCl after the HF treatment to dissolve any fluorides

that may have attempted to form. They were then treated with a sodium pyrophosphate solution

to remove any lingering clay minerals that may have resulted from feldspar digestion. The final

step was to rinse each sample with methanol. This helped to remove excess hydration, which

allowed the samples to dry faster. Once dry, they were ready to be prepared for OSL

measurement.

3.4. Data Collection and Analysis

All samples were measured using a Risø DA-15 automated TL/OSL reader system. This

system includes a 40 mCi ^{90}Sr/^{90}Y β-source, which irradiated at a rate between 0.1005 and

0.0989 Grays per second (Gy/s) (decreasing over the project period), a blue light diode array for

stimulation, and an EMI model 9235 QA photomultiplier tube with optical filtering to allow

signal measurement in the UV emission range (5 mm Hoya U-340) (supplement to Lepper et al.,

2007).

Prior to any stimulation tests or OSL measurements, all aliquots were prepared for

measurement following the same procedure. 24 aliquots were placed into a masking jig at one

time. A non-luminescent silicon adhesive was sprayed over the masking jig, which defined the

area in the center of each aliquot that retained grains. The aliquots were then dipped individually

into a portion of the desired samples and loaded onto the OSL reader's sample carousel for measurement.

Before OSL dating measurements could be made, all samples were screened using infrared stimulation (Short and Huntley, 1992). This step indicates if feldspars are still present in the sample following chemical processing. Since quartz does not respond to infrared light, a signal recorded during infrared stimulation would indicate the sample is not pure quartz and must be chemically re-processed (Duller, 2008). If the extraneous minerals are not removed, they could affect the signal responses measured by blue light stimulation for OSL dating, which would result in unreliable age data.

Data collection followed the SAR procedures (Murray and Wintle, 2000; Wintle and Murray, 2006) outlined in Section 2.3.2., with minor modifications (supplement to Lepper et al., 2007); individual check, regen, and test doses are provided in Appendix B, Table B1. D_e data was collected from 89 to 144 aliquots, depending on the field sample. The complete dataset of all 19 field samples includes approximately 2000 D_e values determined from over 23,000 individual OSL measurements.

The D_e datasets, from each sample, were filtered prior to age calculations to identify unreliable data. Aliquots were excluded from the final datasets if any stage of the SAR protocol yielded a negative, background subtracted, signal response, if any of the aliquot calibration curves were negative, and/or if the difference between the aliquots' administered check dose and the calibrated signal response (referred to as δD_c) was greater than 100 percent (Argyilan, 2014). Following the first three filtering steps, outlier D_e values were filtered out using a ± 2.5 standard deviation window around the mean D_e.

Each aliquot has an associated δD_c value, as previously mentioned, and the mean of δD_c values for the entire dataset is referred to as the dose recovery fidelity (see Section 4.2.); this parameter can be used as a screening method to identify potential systematic error. If a sample's dose recovery fidelity is less than or equal to 5.0%, then the mean D_e does not reflect the presence of significant systematic error. If a sample's dose recovery fidelity is greater than 5.0%, it does not necessarily confirm the presence of systematic error, however other contextual factors must be considered to determine whether or not the age may be considered reliable; these factors may include the dispersion (υ_t) of the sample's D_e values as well as a review of the ages of surrounding beach ridges near the sample in question.

After the datasets have been filtered, the mean D_e, standard deviation, standard error, mean/median ratio (M/m), and dispersion (υ_t) were calculated from the remaining D_e values. The M/m and υ_t parameters will determine whether it is most appropriate to calculate a sample's age using its mean D_e (for symmetric, well reset datasets) or Leading Edge representative dose (for positively asymmetric, poorly reset datasets), as discussed in Section 2.3.2. (supplement to Lepper et al., 2007).

Thirteen samples, collected during the 2020 field season, were sent to the Ohio State University Nuclear Reactor Laboratory for instrumental neutron activation analysis (INAA). Six samples, collected during the 2021 field season, were sent to the North Carolina State University Nuclear Reactor laboratory for INAA, and the same six samples from 2021 were also sent, along with four replicate samples from 2020, to the ALS Geochemistry laboratory to be analyzed using inductively coupled plasma mass spectrometry (ICP-MS). From these analyses, elemental concentrations of K, Rb, Th, and U were obtained and then used to calculate dose rates for each sample (Aitken 1995; 1998); these concentrations are presented in Section 4.3., and Appendix C.

Cosmic ray doses based on sample depth were calculated for all samples using the method of

Prescott and Hutton (1988; 1994); shallow depth adjustments were thus made for the cosmic

dose rates of samples collected at a depth of less than 75 centimeters (Prescott and Hutton,

1988).

4. RESULTS

4.1. Sample Characteristics

Defining the textures of clastic sediments can lead to a more comprehensive understanding of the sediments' mode of transport and deposition. Rounding can indicate the amount of time a grain has been in transport and possibly the mobile agent of the transport, while soil color reflects the degree of soil development and post-depositional influences on the horizon. Combining textural narratives of multiple samples can contribute to a larger geological context for a landform, which may further the understanding of the landform's evolution. A full list of sample characteristics are provided in Appendix D, Table D1., and sediment profiles for each sampling pit are provided in Appendix E.

4.1.1. The Barrens Ecological Area

Samples SI2007 and SI2008 were a stratigraphic pair, collected on the innermost boundary of The Barrens ecological area (Fig. 16). Color variation present in the collection pit was reflected in the color differences of the two samples. SI2007 was stratigraphically higher than SI2008 and was light brown (Munsell Color System: 7.5YR6/4), with subrounded to subangular sand grains; it was collected in an area of the sampling face that showed little to no influence of iron oxide staining. SI2008 was yellowish red (5YR5/6), with subangular to angular sand grains, and was collected in an area of the sampling face that was influenced by iron oxide mottles. Sample SI2009 was located on the modern shoreline of the eastern strandplain, which is also the eastern boundary of The Barrens. It was yellowish red (5YR5/6), with subangular sand grains, and there was no evidence of iron oxide staining present in the collection pit.
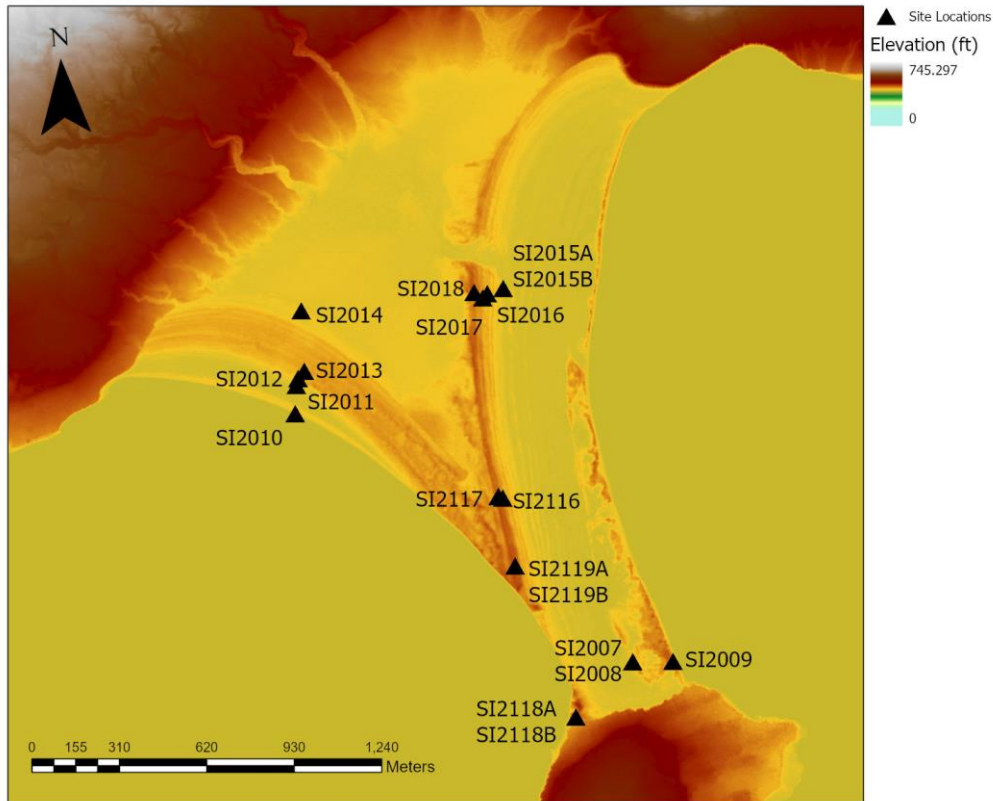
Figure 16. Elevation map of Stockton Island tombolo with sample site locations. Lidar data from NOAA.

4.1.2. The Western Strandplain

Sample SI2010 was located on the modern shoreline of the western strandplain (Fig. 16). It was reddish yellow (5YR6/6), with subangular sand grains. The collection pit showed no influence of iron oxide staining. Between samples SI2010 and SI2011 was a low-lying region with a high water table; this area also coincided with known archaeological sites. For these reasons, the area was avoided for sample collection. Sample SI2011 was located on the next sequential ridge following the low-lying region; it was yellowish red (5YR4/6), with subrounded sand grains. The collection pit showed mottles of iron oxide staining, however, sample collection was not done in an area of the sampling face associated with the staining. Sample SI2012 was located on the next innermost ridge; it was reddish yellow (5YR6/6), with rounded to

subrounded sand grains. The collection pit showed an influence of iron oxide staining, however

sample collection was not done in an area of the sampling face associated with the staining.

Following SI2012, on the next inner ridge, was sample SI2013. It was light reddish brown in

color (5YR6/4), with subrounded to subangular sand grains. The collection pit showed an

influence of iron oxide staining in the form of streaks, however sample collection was not done

in an area of the sampling face associated with the staining. While the ridges between samples

SI2013 and SI2014 were visible, their relief was low which made it difficult to discern distinct

ridge and swale topography. This area also had a high-water table, which made it impossible to

sample without digging into standing water. For these reasons, sample collection could no longer

continue following the natural sequence of the western strandplain's beach ridges. The final

sample collected on the western strandplain was SI2014; it was located on the innermost ridge of

the strandplain, directly next to the bog that is in the center of the tombolo; it was light brown in

color (7.5YR6/3), with rounded to subrounded sand grains. The collection pit showed no

influence of iron oxide staining.

4.1.3. The Eastern Strandplain

Samples SI2015A and SI2015B were a stratigraphic pair, located in the eastern

strandplain on the ridge closest to the western boundary of the lagoon (Fig. 16). SI2015A was

stratigraphically higher, collected from the collection pit's sampling face; SI2015B was collected

from the floor of the collection pit. Both samples were identical in appearance, showing a light

brown color (7.5YR6/4) and subrounded to subangular sand grains. There was no evidence of

iron oxide staining present in the collection pit. Sample SI2016 was the next inner ridge in the

eastern strandplain sequence; it was light reddish brown in color (5YR6/4), with subangular

grains. Sample SI2017 followed, located on the next inner ridge in the eastern strandplain. It

37

showed similar appearance characteristics to SI2016, with a light reddish brown color and subangular to angular sand grains. Sample SI2018 was located on the largest ridge on the tombolo. Similarly to SI2016 and SI2017, sample SI2018 was light reddish brown in color (5YR6/4), with subangular to subrounded sand grains. An influence of iron oxide staining, in the form of prominent reddened columns, were present in the collection pits of samples SI2016, SI2017, and SI2018, although sample collection was not done in areas associated with any such staining.

Sample SI2116 was collected along the same ridge as SI2017; it was yellowish red in color (5YR5/6), with subangular sand grains. Sample SI2117 was collected along the largest ridge on the tombolo, the same as SI2018. It was reddish yellow (5YR7/6), with subangular to subrounded sand grains. Both samples SI2116 and SI2117 showed evidence of iron oxide staining, however sample collection was not done in areas of the sampling faces associated with the staining. Samples SI2118A and SI2118B were a stratigraphic pair, collected on a sandy mound attached to Presque Isle. During excavation, archaeological material was exposed. SI2118A was collected slightly above the archaeological material; it was light reddish brown (5YR6/4), with subangular to subrounded sand grains. SI2118B was collected at the base of the pit where the foreshore deposits were located. It was reddish brown (5YR5/4), with subangular to subrounded sand grains. The collection pit showed an influence of iron oxide staining, although it was not columnar like the other collection pits on or near the large ridge. Samples SI2119A and SI2119B were a stratigraphic pair collected with the intention of evaluating the influence of iron oxide staining on OSL results. SI2119A was reddish brown in color (5YR5/4), with subrounded to rounded sand grains. SI2119B was red in color (5YR5/8), with subangular to subrounded sand grains and collected within an iron oxide column.

4.2. OSL Age Determinations

4.2.1. The Barrens Ecological Area

Samples SI2007 and SI2008 were a stratigraphic pair, with SI2007 stratigraphically higher than SI2008. Shown in Table 2, SI2007 yielded a symmetric distribution (M/m=1.04), with no significant systematic error (δD_c=2.2%). The mean D_e was 0.423±0.023 Gy, with a dose rate of 1.126±0.098 mGy/yr, which yielded an age of 380±20 yrs. SI2008 yielded a symmetric distribution (M/m=1.03), with no significant systematic error (δD_c=2.8%). The mean D_e was 0.418±0.025 Gy, with a dose rate of 0.692±0.060 mGy/yr, which yielded an age of 620±40 yrs. Sample SI2009, which is on the modern shoreline of the eastern strandplain, yielded a symmetric distribution (M/m=1.01), with no significant systematic error (δD_c=0.1%). Its mean D_e was 0.397±0.030 Gy, with a dose rate of 1.224±0.105 mGy/yr, which yielded an age of 320±30 yrs.

4.2.2. The Western Strandplain

Sample SI2010, located on the modern shoreline of the western strandplain, is one of the younger samples collected and showed an extremely low signal response during OSL measurements; because of this, SI2010 was analyzed in two ways. The first followed the filtering procedures described in Section 3.4., and yielded an abnormally negatively asymmetric distribution (M/m=0.54), with a dose recovery fidelity (δD_c) of 10.2%. The mean D_e was 0.048±0.041 Gy, with a dose rate of 0.850±0.070 mGy/yr, which yielded an age of 60±50 yrs. A dose recovery fidelity over 5% is typically an indicator that a sample may exhibit systematic error. This, coupled with the negatively asymmetric distribution, suggests the D_e dataset and thus this age (60±50 yrs) for SI2010 could be unreliable. To adjust for these discrepancies, the second analysis of sample SI2010 was conducted using a process that deviated from the filtering methods described in Section 3.4.

Table 2. OSL age results and related data.

Sample ID	Ridge #	N[1]	M/m^{2}	u_t[3]	dD_c[4]	Equivalent Dose[5] (Gy)	Dose Rate[6] (mGy/a)	Age (yr)	Uncert.[7] (yr)	OSL error[8] (yr)
SI2007	eolian	97/144	1.04	0.547	2.2%	0.423 ± 0.023	1.126 ± 0.098	**380**	40	20
SI2008	eolian	93/144	1.03	0.576	2.8%	0.418 ± 0.024	0.692 ± 0.060	**620**	70	40
SI2009	eolian	95/101	1.01	0.736	0.1%	0.397 ± 0.029	1.224 ± 0.105	**320**	40	30
SI2010	1	94/144	0.54	n/a	10.2%	0.048 ± 0.041	0.850 ± 0.070	**60**	50	50
SI2010†	1	"	1.00*	n/a	"	0.105 ± 0.011	"	**120**	20	10
SI2011 MS	4	73/96	**1.06**	0.520	3.0%	1.421 ± 0.119	0.858 ± 0.069	**1660**	140	190
SI2012 MS	6	77/96	**1.15**	0.617	6.8%	1.063 ± 0.126	0.708 ± 0.058	**1500**	180	220
SI2013	7	80/89	**1.06**	0.372	5.4%	1.911 ± 0.093	0.954 ± 0.079	**2000**	190	100
SI2014	16	94/96	1.01	0.300	0.2%	4.473 ± 0.139	0.903 ± 0.078	**4960**	450	150
SI2015A	8	89/96	**1.07**	0.424	0.0%	2.782 ± 0.183	1.316 ± 0.105	**2110**	220	140
SI2015B	8	87/96	**1.08**	0.542	1.3%	2.249 ± 0.136	1.120 ± 0.093	**2010**	210	120
SI2016	11	92/96	**1.10**	0.470	3.5%	3.664 ± 0.150	1.405 ± 0.117	**2610**	240	110
SI2017	12	86/96	1.03	0.402	1.5%	4.473 ± 0.194	1.241 + 0.091	**3600**	310	160
SI2018	13	91/96	0.98	0.374	0.5%	3.727 ± 0.146	0.998 ± 0.069	**3740**	295	150
SI2116	12	87/96	1.05	0.423	3.2%	5.139 ± 0.233	1.313 ± 0.087	**3490**	310	160
SI2117	13	84/96	1.05	0.468	10.1%	5.222 ± 0.267	1.405 ± 0.130	**3890**	370	200
SI2118A	13	92/96	1.05	0.349	0.8%	5.066 ± 0.184	1.370 ± 0.107	**4020**	370	150
SI2118B	13	85/96	0.95	0.427	0.5%	3.776 ± 0.175	0.981 ± 0.079	**3850**	360	180
SI2119A	13	73/96	1.03	0.559	4.6%	4.978 ± 0.324	1.579 ± 0.125	**3150**	320	210
SI2119B	13	88/96	1.06	0.351	1.9%	5.031 ± 0.205	1.582 ± 0.129	**3180**	290	130

[1] No. of aliquots used for OSL D_e calculation / no. of aliquots from which OSL data was collected (filtering criteria given in Lepper et al, 2003). [2] Mean/median ratio: a measure of dose distribution symmetry/asymmetry (supplement to Lepper et al., 2007). [3] Total dose distribution data dispersion (Std. dev/Mean). [4] Dose recovery fidelity (refer to "check dose" in Lepper et al., 2000 and supplement to Lepper et al., 2007). [5] Equivalent doses are based on the mean and std. err. Of the OSL D_e distribution. [6] Dose rates calculated following the methods described in Aitken (1985; 1998) and Prescott and Hutton (1988; 1994). [7] Fully propagated age uncertainty (Append. B, Aitken, 1985). [8] Age error based on std. err. Of the OSL D_e distribution (Lepper et al., 2011).

A single Gaussian function was assigned as a model for the primary peak of the D_e dataset (Appendix F, Fig. F4.), which gave a refined mean D_e and standard error. The second analysis yielded a symmetric distribution (M/m=1.00), with a dose recovery fidelity of 10.2%. It had a mean D_e of 0.105±0.011 Gy, with a dose rate of 0.850±0.070 mGy/yr, which yielded an age of 120 ±10 yrs. Considering the dose recovery fidelity value did not change between the two analysis methods, it could still suggest evidence of systematic error, however when the age of SI2010 was considered in the context of the entire strandplain, it was retained as it supported the rest of the dataset in creating the age model (Fig. 17).

Sample SI2011 had an asymmetric distribution (M/m=1.06), with no significant systematic error (δD_c=3.0%). Its Leading Edge representative dose was 1.421±0.119 Gy, with a dose rate of 0.859±0.069 mGy/yr, which yielded an age of 1660±140 yrs. Sample SI2012 had an asymmetric distribution (M/m=1.15), with a dose recovery fidelity of 6.8%. Its Leading Edge representative dose was 1.063±0.126 Gy, with a dose rate of 0.708±0.058 mGy/yr, which yielded an age of 1500±180 yrs. The dose recovery fidelity value could suggest evidence of systematic error, however, when the age of SI2012 was considered in the context of the entire strandplain, the age was retained as it supported the rest of the dataset in creating the age model for the strandplain. Sample SI2013 had an asymmetric distribution (M/m=1.06), with a dose recovery fidelity of 5.4%. Its Leading Edge representative dose was 1.911±0.093 Gy, with a dose rate of 0.954±0.079 mGy/yr, which yielded an age of 2000±100 yrs. The dose recovery fidelity value could suggest evidence of systematic error, however, when the age of SI2013 was considered in the context of the entire strandplain, the age was retained as it supported the rest of the dataset in creating the age model for the strandplain. Sample SI2014 had a symmetric distribution

(M/m=1.01), with no significant systematic error (δD_c=0.2%). Its mean D_e was 4.473±0.139 Gy, with a dose rate of 0.903±0.078 mGy/yr, which yielded an age of 4960±150 yrs.

The age model for the western strandplain (Fig. 17) shows a trendline representing a continuous relationship between the youngest sample, located on the modern shoreline, and the oldest sample, located on the innermost ridge near the bog. The regression equation in Figure 17 can thus be used to estimate the depositional age of any individual ridge in the western strandplain. The age model can also be used to estimate a ridge preservation rate of 1 ridge approximately every 320 years for this strandplain.

Sample#	Ridge#	Age (yr)	OSL error (yr)
SI2010	1	120	10
SI2011	4	1660	140
SI2012	6	1500	180
SI2013	7	2000	100
SI2014	16	4960	150
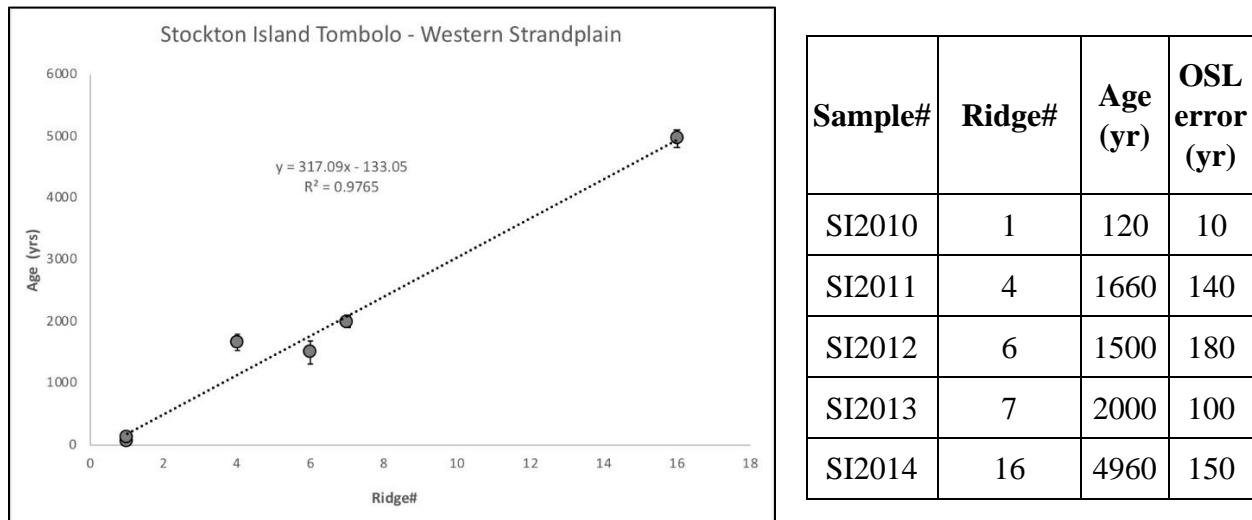
Figure 17. Age model (left) and associated data (right) for the entire western strandplain of the Stockton Island Tombolo.

4.2.3. The Eastern Strandplain

Samples SI2015A and SI2015B were a stratigraphic pair, located in the eastern strandplain on the ridge closest to the western boundary of the lagoon. SI2015A yielded a positively asymmetric distribution (M/m=1.07), with no indication of systematic error (δD_c=0.0%). Its Leading Edge representative dose was 2.782±0.183 Gy, with a dose rate of 1.316±0.105 mGy/yr, which yielded an age of 2110±140 yrs. SI2015B yielded a positively

asymmetric distribution (M/m=1.08), with no significant systematic error (δD_c=1.3%). Its

Leading Edge representative dose was 2.249±0.136 Gy, with a dose rate of 1.120±0.093 mGy/yr,

which yielded an age of 2010±120 yrs. SI2016, the next inner ridge, yielded a positively

asymmetric distribution (M/m=1.10), with no significant systematic error (δD_c=3.5%). Its

Leading Edge representative dose was 3.664±0.150 Gy, with a dose rate of 1.405±0.117 mGy/yr,

which yielded an age of 2610±110 yrs. SI2017 follows, and yielded a symmetric distribution

(M/m=1.03), with no significant systematic error (δD_c=1.5%). Its mean D_e was 4.473±0.194 Gy,

with a dose rate of 1.241±0.090 mGy/yr, which yielded an age of 3600±160 yrs. SI2018, which

was collected from the tombolo's highest ridge, yielded a symmetric distribution (M/m=0.98),

with no significant systematic error (δD_c=0.5%). Its mean D_e was 3.727±0.146 Gy, with a dose

rate of 0.998±0.069 mGy/yr, which yielded an age of 3740±150 yrs.

SI2116, which was collected from the same ridge as SI2017, yielded a symmetric

distribution (M/m=1.05), with no significant systematic error (δD_c=3.2%). Its mean D_e was

5.139±0.233 Gy, with a dose rate of 1.474±0.112 mGy/yr, which yielded an age of 3490±160

yrs. SI2117, which was collected from the same ridge as SI2018, yielded a symmetric

distribution (M/m=1.05), with a dose recovery fidelity of 10.1%. Its mean D_e was 5.222±0.267

Gy, with a dose rate of 1.342±0.106 mGy/yr, which yielded an age of 3890±200 yrs. The dose

recovery fidelity value could suggest evidence of systematic error, however when the age of

SI2117 was considered in the context of the entire strandplain; it was retained because it was

consistent with the rest of the dataset and helped create a robust age model for the strandplain.

SI2118A yielded a symmetric distribution (M/m=1.05), with no significant systematic error

(δD_c=0.8%). Its mean D_e was 5.066±0.184 Gy, with a dose rate of 1.260±0.105 mGy/yr, which

yielded an age of 4020±150 yrs. SI2118B yielded a symmetric distribution (M/m=0.95), with no

significant systematic error (δD_c=0.5%). Its mean D_e was 3.776±0.175 Gy, with a dose rate of 0.981±0.079 mGy/yr, which yielded an age of 3850±180 yrs. SI2119A yielded a symmetric distribution (M/m=1.03), with no significant systematic error (δD_c=4.6%). Its mean D_e was 4.978±0.324 Gy, with a dose rate of 1.579±0.125 mGy/yr, which yielded an age of 3150±210 yrs. SI2119B yielded a positively asymmetric distribution (M/m=1.06), with no significant systematic error (δD_c=1.9%). Although sample SI2119B was slightly positively asymmetric (the "gray zone" discussed in Section 2.3.2.), when its potential ages were considered in the context of the full data set, a more coherent age model resulted if this sample was treated as symmetric. Its mean D_e was 5.031±0.205 Gy, with a dose rate of 1.582±0.129 mGy/yr, which yielded an age of 3180±130 yrs.

Age models were constructed for each strandplain using the ages of each sample and the ridge numbers from which the samples were collected. The age model for the Eastern strandplain is shown in Figure 18. The regression equation can be used to estimate the depositional age of any individual ridge in the eastern strandplain. The age model can also be used to estimate a ridge preservation rate of 1 ridge approximately every 330 years for this strandplain. The preservation rate is somewhat different from the formation rate as ridges could form on shorter time intervals but be eroded or reworked until the relative lake level allows for the preservation of a ridge.
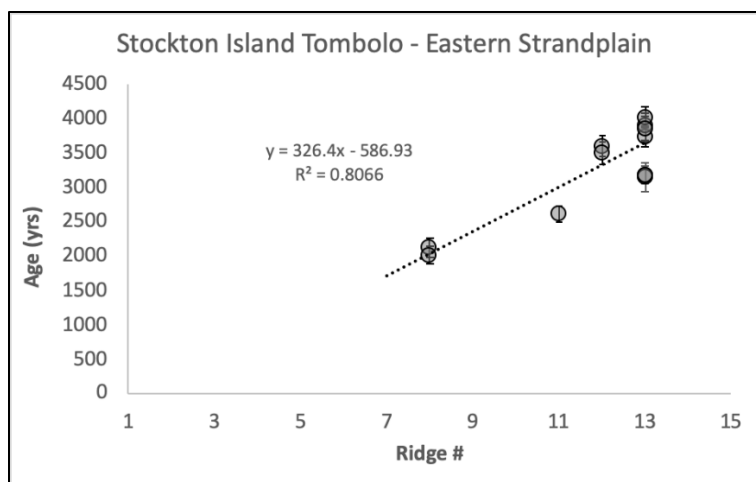
Sample #	Ridge #	Age (yr)	OSL err. (yr)
SI2015A	8	2110	140
SI2015B	8	2010	120
SI2016	11	2610	110
SI2017	12	3600	160
SI2116	12	3490	160
SI2117	13	3890	200
SI2118A	13	4020	150
SI2118B	13	3850	180
SI2018	13	3740	150
SI2119A	13	3150	210
SI2119B	13	3180	130

Figure 18. Age model (left) and associated data (right) for the entire eastern strandplain of the Stockton Island Tombolo.

4.3. Elemental Analysis Results

As introduced in Section 3.4., samples from both the 2020 and 2021 field seasons were submitted for INAA and ICP-MS analysis to obtain elemental concentration data for each sample. Thirteen samples from the 2020 field season were sent to the Ohio State University Nuclear Reactor Laboratory for INAA. Six samples from the 2021 field season were sent to the North Carolina State University Nuclear Reactor laboratory for INAA, and the same six samples, along with four replicates from the 2020 field season, were sent to the ALS Geochemistry laboratory for ICP-MS analysis. The replicates were used to compare ICP-MS results to INAA results. Elemental concentrations are shown below in Table 3.

Table 3. Supporting data for dosimetric analysis. Average elemental concentrations by INAA* and ICP-MS**.

Sample ID	Sample depth (cm)	H$_2$O (%)	N	K (ppm)	± K (ppm)	Rb (ppm)	± Rb (ppm)	Th (ppm)	± Th (ppm)	U (ppm)	± U (ppm)
SI2007	28	10±3	1/1	8222	700	24.11	2.84	1.548	0.151	0.563	0.055
SI2008	77	18±3	1/1	4239	363	12.44	2.02	1.260	0.124	0.519	0.045
SI2009	98	15±3	1/1	10553	890	30.79	3.35	1.797	0.173	0.503	0.046
SI2010	75	12±3	1/1	5207	441	14.28	2.09	1.830	0.171	0.614	0.049
SI2011	57	18±3	2/2	7022	496	17.09	2.16	1.440	0.141	0.432	0.042
SI2012	83	15±3	2/2	4616	330	18.59	2.63	1.618	0.160	0.436	0.046
SI2013	67	15±3	1/1	6805	576	16.90	2.25	1.904	0.181	0.591	0.050
SI2014	61	33±3	1/1	8695	735	24.29	3.55	1.512	0.145	0.516	0.046
SI2015A	49	15±3	1/1	10009	843	29.39	3.60	2.100	0.199	1.021	0.078
SI2015B	77	33±3	1/1	11038	932	33.31	4.01	1.899	0.186	0.755	0.064
SI2016	72	15±3	1/1	11873	1002	34.13	4.29	2.633	0.249	0.596	0.055
SI2017	66	12±3	2/2	11455	967	33.72	4.15	2.266	0.217	0.676	0.059
SI2018	77	12±3	1/2	10442	955	25.07	2.37	1.900	0.177	0.604	0.047
SI2116	55	12±3	2/2	10344	832	35.16	3.36	2.922	0.279	1.195	0.109
SI2117	59	10±3	2/2	9849	785	33.56	3.21	2.242	0.215	0.838	0.087
SI2118A	62	12±3	3/3	9408	820	32.54	3.09	2.488	0.236	0.689	0.073
SI2118B	107	12±3	2/2	6762	532	23.12	2.22	1.846	0.178	0.550	0.058
SI2119A	76	12±3	2/2	13288	1018	44.44	4.27	2.224	0.214	0.773	0.076
SI2119B	76	12±3	2/2	13761	1076	46.24	4.43	2.049	0.197	0.653	0.068

*INAA – Instrumental Neutron Activation Analysis
**ICP-MS – Inductively Coupled Plasma Mass Spectrometry

5. DISCUSSION

5.1. The Barrens Ecological Area

Previous research, conducted by Booth et al. (2021), suggests various fire episodes have occurred on the Stockton Island tombolo since its initiation. Fire is relevant to the formation of dunes because fires burn vegetation that typically keeps sediment from moving. By removing the stability from the vegetation, sediment can be more easily windblown, contributing to the formation of dunes. The presence of charcoal was observed in cores collected in the eastern strandplain lagoon (point A in Fig. 15), as well as the bog located in the center of the tombolo (point G in Fig. 15). Charcoal present in cores collected from the lagoon can be interpreted as records of fire on Stockton Island and/or the tombolo (Fig. 19); from these cores, Booth et al. (2021) were able to project the formation of the lagoon initiated between approximately 700 to 800 radiocarbon years ago.
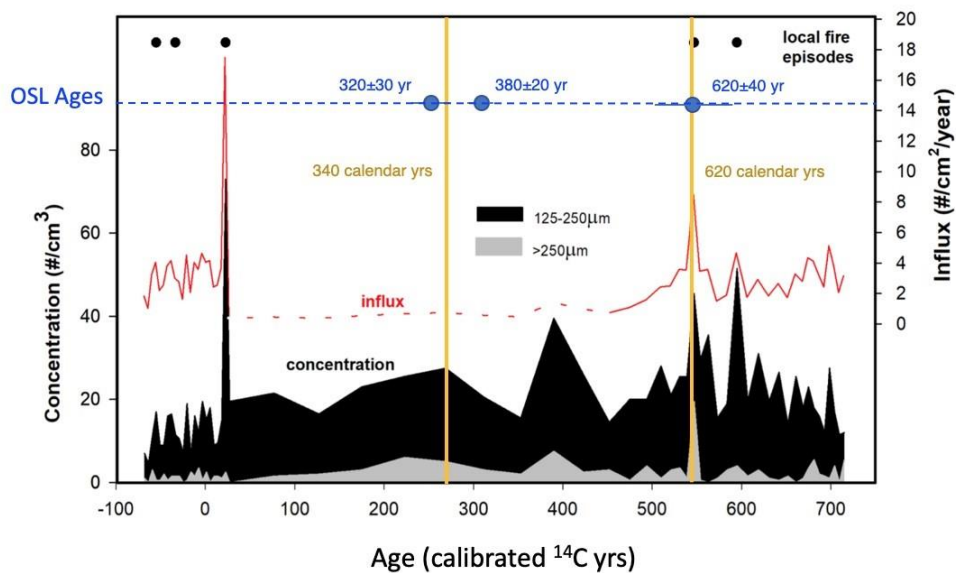
Figure 19. Diagram showing the correlation between OSL results and the concentration of charcoal found in cores collected from the lagoon present within the eastern strandplain. Vertical yellow lines with adjusted ages indicate charcoal concentration peaks (modified from Booth et al., 2021). Blue data points are the OSL ages obtained in this study.

47

All three samples collected in The Barrens Ecological Area (point B in Fig. 15) correlate strongly with charcoal concentration peaks in the lagoon (Fig. 19; Booth et al. 2021) at 340 and 620 calendar years ago. The age from sample SI2008, the deepest in the Barrens, is also consistent with the age of the initiation of the lagoon which, as previously noted, occurred between approximately 700 to 800 radiocarbon years ago.

5.2.   The Western Strandplain

Based on ages determined from the bog by Booth et al. (2021), the initiation of the tombolo dates to approximately 5000 radiocarbon years ago. The age of sample SI2014 (4960±150 yrs), from the beach ridge closest to the bog along the western strandplain, correlates well to this initiation age. The age model for the western strandplain (Fig. 17) shows a continuous linear trend, which suggests there were no significant gaps in time. This means there must be a ridge relating to the Nipissing phase present within the western strandplain, which implies it simply lacks a strong topographic expression.

5.3.   The Eastern Strandplain

As introduced in Section 2.1.4., the topographic signature of the Nipissing phase is a prominent ridge with a steep lakeward slope, separating it from surrounding beach ridges; this signature is visible throughout most of the Great Lakes region. During the 2020 field season, the ridge with the highest elevation (present along the eastern strandplain) was expected to yield ages indicative of the peak Nipissing phase, considering its topography appeared to be similar to that of the common Nipissing phase signature. Sample SI2018, collected from this ridge, yielded an age of 3740±150 years, which is significantly younger than the Nipissing phase's age of 4500 years. Sample SI2017, collected from the adjacent ridge immediately lakeward to that of the

ridge with the highest elevation, yielded a sequentially consistent age of 3600±160 years, which was also younger than what was initially expected.

Subsequent sampling in the 2021 field season attempted to resolve the difference between the OSL ages for the largest ridge and the expected Nipissing phase age. As described in Section 4.2.2., these samples from the prominent ridge yielded ages within a range of 3150 to 4020 years ago, which does not include the Nipissing phase age of 4500 years. These results answered the question of whether or not sample SI2018 was anomalous, however it led to further questions regarding the evolution of the ridge with the highest elevation.

Glacial isostatic adjustment (GIA) is expected to influence the rate of water level change within the Great Lakes region (see Section 2.1.3. for a more detailed description of GIA). Adjusting for GIA, Johnston et al. (2012) calculated the rate of water level change in Lake Superior that occurred between 4500 and 3000 years ago to be approximately -6cm/century. During this time, the rate of GIA for the southern end of Lake Superior was calculated to be approximately -33cm/century (Johnston et al., 2012; Mainville and Craymer, 2005), meaning the land surface was subsiding. Opersko (2021) created a paleohydrograph model specifically for the Stockton Island tombolo, based on preliminary OSL data from this project. The model constrained the GIA rate during the Nipissing phase to between -15 and -33 cm/century (Fig. 20). The difference between the rate of water level decline and the negative GIA rate could offer an explanation as to why and how the ridge with the highest elevation accumulated such a high amount of sediment after the peak of the Nipissing phase.
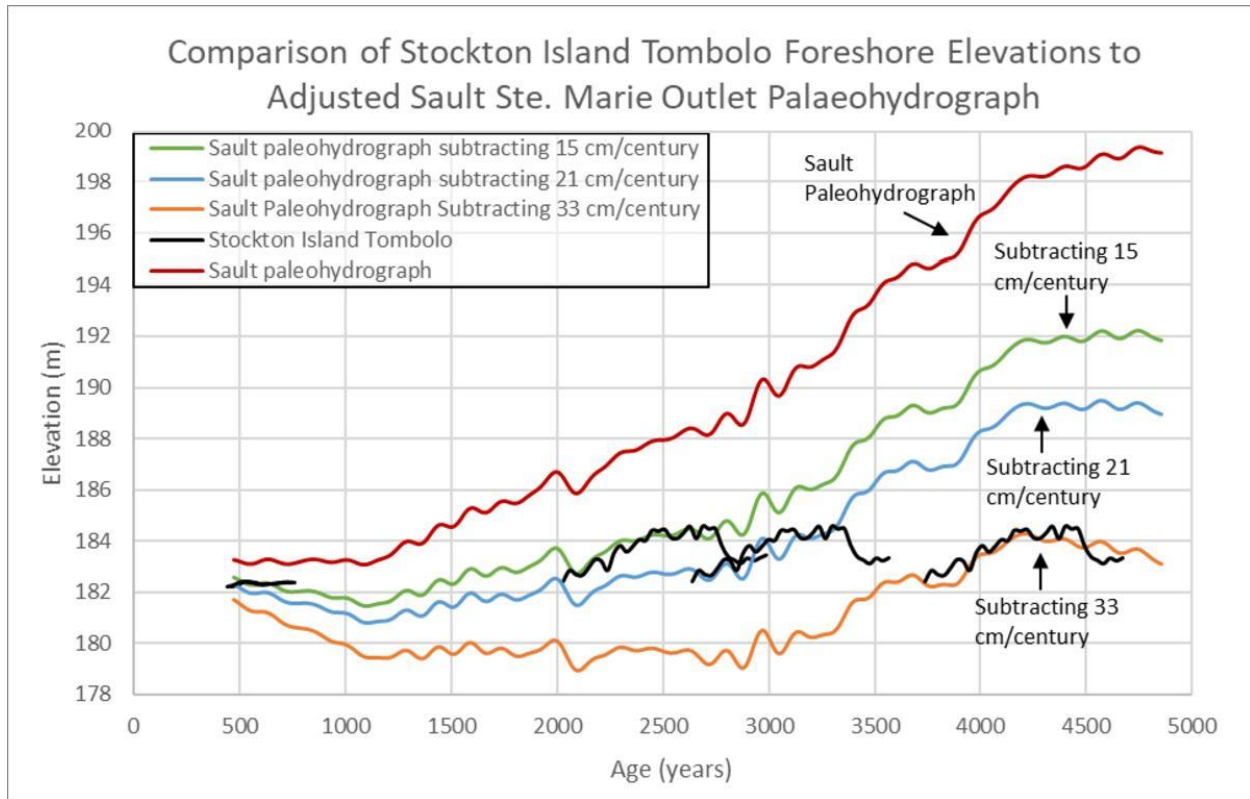
Figure 20. Paleohydrograph showing the relationship between the Stockton Island foreshore elevations compared to various water level phases (Opersko, 2021).

A depositional transgression would occur when the water level decreases slower than the GIA driven subsidence; beach ridges would subsequently form on top of each other, vertically and potentially landward, rather than building lakeward, or horizontally. The GIA subsidence rates reported by Johnston et al. (2012) and Mainville and Craymer (2005) are approximately three to five times faster than that of the water level decline rate following the Nipissing phase. This means the crust below and around the Apostle Islands National Lakeshore was subsiding faster than the water level was dropping. These conditions are conducive to the deposition of successive beach ridges building in a vertical and potentially landward manner. These conditions also suggest the reason why an OSL age could not be attributed to the peak of the Nipissing

phase; sediment associated with the Nipissing phase is expected to have been present at depths too deep to reach using the sampling methods discussed in Section 3.2.

Not only could this hypothesis offer an explanation as to how the ridge with the highest elevation formed while yielding ages younger than that of the peak of the Nipissing phase, but it also suggests an explanation that accounts for the apparent truncation of the western strandplain by the eastern strandplain. As the crustal elevation fell from negative GIA rates, younger beach ridges depositing in the eastern strandplain could have been deposited on top of the older beach ridges of the western strandplain, pushing the shoreline landward. The location of Stockton Island within the southwestern portion of Lake Superior suggests the greatest amount of wave energy likely affected the eastern strandplain more than the western. The western strandplain beach ridges may have been less substantive and thus would have been susceptible to the erosion or over-deposition of the eastern strandplain's beach ridges as the shoreline migrated inward.

6. CONCLUSION

OSL ages have been determined for 19 samples collected along the eastern and western strandplains of the Stockton Island tombolo. Three samples were collected from The Barrens Ecological Area, with each correlating to past fire episodes (Booth et al., 2021). OSL results from The Barrens also support initiation of the lagoon approximately 700 to 800 years ago.

Ages determined for the samples collected along the western strandplain were consistent with the initiation of the tombolo approximately 5000 years ago (Booth et al., 2021). The innermost ridge, closest to the bog in the center of the tombolo, yielded an age of just under 5000 years. While the collection of samples along a regularly-spaced transect was interrupted due to a high water table and low relief of ridge and swale topography, the western strandplain ages still resulted in a linear and continuous trend. An age model was produced for the western strandplain that can be used to estimate ages for the ridges that were not sampled. Among these ridges would be a ridge correlating to the Nipissing phase. While its topography is not as pronounced as the Nipissing phase's typical signature, it does not affect the overall interpretation of the evolution and formation of the Stockton Island tombolo.

A beach ridge correlating directly to the Nipissing high water level age of 4500 years was not confirmed in the eastern strandplain. A potential explanation for the ridge with the highest elevation relates to the relationship between water level decline following the Nipissing phase, and a negative GIA rate of the Apostle Islands region. The large ridge may have formed due to a depositional transgression, where beach ridges were stacked on top of each other as the crust of the Apostle Islands National Lakeshore subsided at approximately three to five times the rate as that of the declining water level. This could also account for the apparent truncation of the western strandplain by the eastern strandplain, as the beach ridges may have not only built on top

of each other but also built inward, overlaying previously deposited beach ridges along the western aspect of the tombolo.

This research has provided additional information regarding Holocene lake levels. The Stockton Island tombolo was previously dated by Booth et al. (2021) using radiocarbon dating techniques, however their collection strategy was not intended to date beach ridges. By providing OSL age determinations for the eastern and western strandplains, this research has further contributed to understanding the evolution of the Stockton Island tombolo over time. This research also draws attention to the relationship between the rate of water level change in Lake Superior and GIA rates in an area where both were negative.

REFERENCES CITED

Aitken, M.J., 1985. Thermoluminescence Dating: Academic Press, London, 359 p.

Aitken, M.J., 1998. An introduction to optical dating: Oxford University Press, New York, 267 p.

Argyilan, E.P., Forman, S.L., Johnston, J.W., Wilcox, D.A., 2005, Optically stimulated luminescence dating of late Holocene raised strandplain sequences adjacent to Lakes Michigan and Superior, Upper Peninsula, Michigan, USA: Quaternary Research, v. 63, p. 122-135.

Argyilan, E., Lepper. K., and Thompson, T., 2014. Analysis of intra-dune variability of optical ages yields a refined chronology of late Holocene coastal development along the southern shore of Lake Michigan, *in* Fisher, T. G., and Hansen, E. C., *Eds.,* Coastline and Dune Evolution along the Great Lakes: Geological Society of America Special Paper 508, p. 31-46.

Baedke, S.J., and Thompson, T.A., 2000, A 4,700-year record of lake level and isostasy for Lake Michigan: Journal of Great Lakes Research, v. 26, no. 4, p. 416-426.

Baedke, S.J., Thompson, T.A., Johnston, J.W., and Wilcox, D.A., 2004, Reconstructing paleo lake levels from relict shorelines along the Upper Great Lakes: Aquatic Ecosystem Health and Management, v. 7, no. 4, p. 435-449.

Booth, R.K., Huff, M.G., Bebout, J.A., Lynch, E.A., and Schuurman, G.W., 2021, Fire, vegetation, and water-level history from the Stockton Island tombolo: Apostle Islands National Lakeshore; Natural Resource Report. NPS/APIS/NRR—2021/2221. National Park Service. Fort Collins, Colorado, 37 p.

Curray, J.R., 1964. Transgressions and regressions, *in* Miller, R.L., *Ed.,* Papers in Marine
Geology. Macmillan, New York, p. 175-203.

Duller, G., 2008, Luminescence Dating: Guidelines on using luminescence dating in
archaeology: Swindon, English Heritage, 43 p.

Fairchild, L.M., Swanson-Hysell, N.L., Ramezani, J., Sprain, C.J., Bowring, S.A., 2017, The end
of Midcontinent Rift magmatism and the paleogeography of Laurentia: Lithosphere, v. 9,
no. 1, p. 117-133.

Huggett, R.J., 2011, Fundamentals of Geomorphology: Routledge, New York, 515 p.

Johnston, J.W., Argyilan, E.P., Thompson, T.A., Baedke, S.J., Lepper, K., Wilcox, D.A.,
Forman, S.L., 2012, A Sault-outlet-referenced mid- to late-Holocene paleohydrograph for
Lake Superior constructed from strandplains of beach ridges: Canadian Journal of Earth
Science, v. 49, p. 1263-1279.

Lepper, K., Agersnap-Larsen, N. and McKeever, S.W.S., 2000, Equivalent dose distribution
analysis of Holocene eolian and fluvial quartz sands from Central Oklahoma. Radiation
Measurements, 32: 603-608.

Lepper, K., 2001, Development of an objective dose distribution analysis method for
luminescence dating and pilot studies for planetary applications. Ph.D. Dissertation,
Oklahoma State University, Stillwater, OK, 288 p.

Lepper, K., Fisher, T.G., Hajdas, I., and Lowell, T.V., 2007, Ages for the Big Stone Moraine and
the oldest beaches of glacial Lake Agassiz: Implications for deglaciation chronology:
Geology, v. 35, no. 7, p. 667-670.

Mainville, A., and Craymer, M.R., 2005, Present-day tilting of the Great Lakes region based on
water level gauges: GSA Bulletin, v. 117, p. 1070-1080.

Morey, G.B., and Southwick, D.L., 1995, Allostratigraphic Relationships of Early Proterozoic
Iron-Formations in the Lake Superior Region: Economic Geology, v. 90, no. 7, p. 1983-
1993.

Murray, A.S., and Wintle, A.G., 2000, Luminescence dating of quartz using an improved single-
aliquot regenerative-dose protocol: Radiation Measurements, v. 32, p. 57-73.

Ojakangas, R.W., and Matsch, C.L., 1982, Minnesota's Geology: The University of Minnesota
Press, Minneapolis, 255 p.

Opersko, D.A., 2021, Remote paleohydrograph reconstruction of the Stockton Island Tombolo.
B.S. Thesis, University of Waterloo, Waterloo, Ontario, 80 p.

Payette, S., Eronen, M., Jasinksi, J.J., 2002, The circumboreal tundra-taiga interface: late
Pleistocene and Holocene changes: Ambio, v. 12, p. 15-22.

Prescott, J.R., Hutton, J.T., 1988, Cosmic-ray and gamma-ray dosimetry for TL and electron-
spin-resonance, Nuclear Tracks and Radiation Measurements, v. 14, p. 223–227.

Prescott, J.R., Hutton, J.T., 1994. Cosmic ray contributions to dose rates for luminescence and
ESR dating: Large depths and long-term time variations: Radiation Measurements, v. 23,
p. 497-500.

Schultz, K.J., and Cannon, W.F., 2007, The Penokean orogeny in the Lake Superior region:
Precambrian Research, v. 157, p. 4-25.

Sella, G.F., Stein, S., Dixon, T.H., Craymer, M., James, T.S., Mazzotti, S., Dokka, R.K., 2007,
Observation of glacial isostatic adjustment in "stable" North America with GPS:
Geophysical Research Letters, v. 34, p. 1-6.

Short, M.A., Huntley, D.J., 1992. Infrared stimulation of quartz: Ancient TL, v. 10, p. 19-21.

Thompson, T.A., Baedke, S.J., 1995, Beach-ridge development in Lake Michigan: shoreline

behavior in response: Journal of Great Lakes Research, v. 26, no. 4, p. 416-426.

Thompson, T.A., Lepper, K., Endres, A.L., Johnston, J.W., Baedke, S.J., Argyilan, E.P., Booth,

R.K., Wilcox, D.A., 2011, Mid Holocene lake level and shoreline behavior during the

Nipissing phase of the upper Great Lakes at Alpena, Michigan, USA: Journal of Great

Lakes Research, v. 37, no. 3, p. 567-576.

Thompson, T.A., Johnston, J.W., Lepper, K., 2014, The contemporary elevation of the peak

Nipissing phase at outlets of the upper Great Lakes, *in* Fisher, T. G., and Hansen, E. C.,

Eds., Coastline and Dune Evolution along the Great Lakes: Geological Society of

America Special Paper 508, p. 15-29.

Thornberry-Ehrlich, T. L. 2015. Apostle Islands National Lakeshore: Geologic resources

inventory report. Natural Resource Report NPS/NRSS/GRD/NRR—2015/972. National

Park Service, Fort Collins, Colorado, 79 p.

USGS, 2019, General Geologic Map Lake Superior: U.S. Geological Survey,

https://www.usgs.gov/media/images/general-geologic-map-lake-superior (accessed

August 22, 2022).

Wessa, P., 2015, Kernel Density Estimation (v. 1.0.12) in Free Statistics Software (v. 1.2.1),

Office for Research Development and Education,

URL http://www.wessa.net/rwasp_density.wasp/

Wintle, A.G., Murray, A., 2006. A review of quartz optically stimulated luminescence

characteristics and their relevance in single-aliquot regeneration dating protocols:

Radiation Measurement, v. 41, p. 369-391.

APPENDIX A. GEOLOGIC TIME SCALE

Eon	Era	Period	Epoch	MYA	Geologic Map Units	Apostle Islands NL Events
Phanerozoic	Cenozoic (CZ)	Quaternary (Q)	Holocene (H)	0.01	Qc and Qw deposited Qsm, Qp, Qou, Qgw, Qgl, Qgh, and Qb deposited Qgg, Qsc, Qsg, Qsu, and Qsuc deposited	Human history, shoreline change Continued erosion, stream incision Lake Superior forms Worldwide glaciation, periglacial conditions
			Pleistocene (PE)			
		Neogene (N)	Pliocene (PL)	2.6		Continued erosion and mass wasting
			Miocene (MI)	5.3		
		Paleogene (PG)	Oligocene (OL)	23.0		
			Eocene (E)	33.9		
			Paleocene (EP)	56.0		
				66.0		
	Mesozoic (MZ)	Cretaceous (K)		145.0		Erosion
		Jurassic (J)		201.3		Breakup of Pangaea begins; Atlantic Ocean opens
		Triassic (TR)		252.2		
	Paleozoic (PZ)	Permian (P)		298.9		Supercontinent Pangaea intact
		Pennsylvanian (PN)		323.2		
		Mississippian (M)		358.9		
		Devonian (D)		419.2		
		Silurian (S)		443.7		
		Ordovician (O)		485.4		Erosion and weathering of overlying sediments
		Cambrian (C)		541.0		
Proterozoic	Neoproterozoic (Z)	Precambrian (PC)				Supercontinent Rodinia rifted apart Burial and deformation of Bayfield Group
	Mesoproterozoic (Y)			1,000	PCo, PCdi, and PCch deposited PCf deposited Ync deposited Midcontinent rift volcanics (Yv) erupted	Erosion of granitic crust and deposition of Bayfield Group Midcontinent rift becomes inactive; basins subside Widespread volcanism in rift Midcontinent rift began to open Lake Superior basin developed
	Paleoproterozoic			1,600		Uplift, volcanism, widespread erosion
				2,500		Granitic crust formed, metamorphism
Archean				≈4,000		
Hadean				4,600	Formation of the Earth	

Figure A1. Geologic timescale showing the Proterozoic and Phanerozoic eons (Thornberry-Ehrlich, 2015).

APPENDIX B. APPLIED RADIATION DOSES

Table B1. Regen, check, and test doses used for each sample during OSL measurements.

Sample	Regen Dose (sec)	D_c (sec)	D_t (sec)
SI2007	2, 4, 6, 8	5	5
SI2008	2, 4, 6, 8	5	5
SI2009	4, 8, 12, 16	10	5
SI2010	4, 8, 12, 16	10	5
SI2011	10, 20, 30, 40	25	10
SI2012	10, 20, 30, 40	25	10
SI2013	15, 25, 35, 45	30	10
SI2014	25, 40, 55, 70	45	10
SI2015A	20, 35, 50, 65	40	10
SI2015B	25, 40, 55, 70	45	10
SI2016	25, 40, 55, 70	45	10
SI2017	25, 40, 55, 70	45	10
SI2018	25, 40, 55, 70	45	10
SI2116	25, 40, 55, 70	45	10
SI2117	25, 40, 55, 70	45	10
SI2118A	25, 40, 55, 70	45	10
SI2118B	25, 40, 55, 70	45	10
SI2119A	25, 40, 55, 70	45	10
SI2119B	25, 40, 55, 70	45	10

APPENDIX C. ELEMENTAL CONCENTRATIONS

Table C1. Elemental concentrations for each sample, including INAA, ICP-MS, and averages calculated in bold.

Type	Sample ID	K (ppm)	± K (ppm)	Rb (ppm)	± Rb (ppm)	Th (ppm)	± Th (ppm)	U (ppm)	± U (ppm)
Stockton Island Elemental Analysis Results									
INAA	SI2007	8222	700	24.1	2.84	1.548	0.151	0.563	0.055
INAA	SI2008	4239	363	12.4	2.02	1.260	0.124	0.519	0.045
INAA	SI2009	10553	890	30.8	3.35	1.797	0.173	0.503	0.046
INAA	SI2010	5207	441	14.3	2.09	1.830	0.171	0.614	0.049
INAA	SI2011	8339	710	17.9	2.69	1.540	0.147	0.455	0.042
ICP-MS	SI2011'	5645	282	16.30	1.63	1.340	0.134	0.410	0.041
Average	**SI2011**	**7022**	**496**	**17.09**	**2.16**	**1.440**	**0.141**	**0.432**	**0.042**
INAA	SI2012	5745	486	26.2	4.16	1.976	0.194	0.493	0.053
ICP-MS	SI2012'	3487	174	11.0	1.10	1.260	0.126	0.380	0.038
Average	**SI2012**	**4616**	**330**	**18.59**	**2.63**	**1.618**	**0.160**	**0.436**	**0.046**
INAA	SI2013	6805	576	16.9	2.25	1.904	0.181	0.591	0.050
INAA	SI2014	8695	735	24.3	3.55	1.512	0.145	0.516	0.046
INAA	SI2015A	10009	843	29.4	3.60	2.100	0.199	1.021	0.078
INAA	SI2015B	11038	932	33.3	4.01	1.899	0.186	0.755	0.064
INAA	SI2016	11873	1002	34.1	4.29	2.633	0.249	0.596	0.055
INAA	SI2017	8048	680	34.7	3.80	2.014	0.192	0.612	0.052
ICP-MS	SI2017'	11290	565	34.00	3.40	2.220	0.222	0.610	0.061
Average	**SI2017**	**9669**	**622**	**34.37**	**3.60**	**2.117**	**0.207**	**0.611**	**0.056**
~~INAA~~[*]	~~SI2018~~	~~10442~~	~~955~~	~~25.1~~	~~2.37~~	~~1.900~~	~~0.177~~	~~0.604~~	~~0.047~~
ICP-MS	**SI2018'**	**7139**	**357**	**23.30**	**2.33**	**1.670**	**0.167**	**0.600**	**0.060**
ICP-MS	SI2116	9962	498	30.80	3.08	1.970	0.197	0.870	0.087
INAA	SI2116'	10725	1167	39.51	3.64	3.874	0.360	1.521	0.132
Average	**SI2116**	**10344**	**832**	**35.16**	**3.36**	**2.922**	**0.279**	**1.195**	**0.109**
ICP-MS	SI2117	9879	494	30.30	3.03	1.940	0.194	0.630	0.063
INAA	SI2117'	9819	1076	36.82	3.40	2.544	0.237	1.047	0.112
Average	**SI2117**	**9849**	**785**	**33.56**	**3.21**	**2.242**	**0.215**	**0.838**	**0.087**
ICP-MS	SI2118A	10626	531	33.70	3.37	1.990	0.199	0.700	0.070
INAA	SI2118A"	9742	1067	35.28	3.25	3.436	0.319	0.694	0.076
INAA	SI2118A'	7856	862	28.63	2.65	2.038	0.190	0.673	0.072
Average	**SI2118A**	**9408**	**820**	**32.54**	**3.09**	**2.488**	**0.236**	**0.689**	**0.073**
ICP-MS	SI2118B	7056	353	22.40	2.24	1.750	0.175	0.570	0.057
INAA	SI2118B'	6469	712	23.84	2.21	1.942	0.181	0.530	0.060
Average	**SI2118B**	**6762**	**532**	**23.12**	**2.22**	**1.846**	**0.178**	**0.550**	**0.058**
ICP-MS	SI2119A	14445	722	44.20	4.42	2.120	0.212	0.780	0.078
INAA	SI2119A'	12130	1314	44.68	4.11	2.327	0.216	0.766	0.074
Average	**SI2119A**	**13288**	**1018**	**44.44**	**4.27**	**2.224**	**0.214**	**0.773**	**0.076**
ICP-MS	SI2119B	14279	714	43.60	4.36	1.920	0.192	0.640	0.064
INAA	SI2119B'	13242	1439	48.88	4.50	2.178	0.203	0.666	0.071
Average	**SI2119B**	**13761**	**1076**	**46.24**	**4.43**	**2.049**	**0.197**	**0.653**	**0.068**
*Strike-through indicates one analysis deemed an outlier and not used for age calculations									

APPENDIX D. SAMPLE CHARACTERISTICS

Table D1. Sample characteristics noted during in-field analysis and microscope analysis.

Sample	Soil Color	Fe-Oxide	Rounding	Frosting
SI2007	Light brown	No	Subrounded/subangular	no
SI2008	Yellowish red	Yes, mottles	Subangular/angular	Lightly so
SI2009	Yellowish red	No	Subangular	no
SI2010	Reddish yellow	No	Subrounded	no
SI2011	Yellowish red	Yes, mottles	Subrounded	Too difficult to tell
SI2012	Reddish yellow	Yes	Round/subrounded	Too difficult to tell
SI2013	Light reddish brown	Yes, streaks	Subrounded/subangular	Possible frosting, too difficult to tell
SI2014	Light brown	No	Round/subrounded	yes
SI2015A	Light brown	No	Subrounded/subangular	yes
SI2015B	Light brown	No	Subrounded/subangular	yes
SI2016	Light reddish brown	Yes, columns	Subangular	Possible frosting, too difficult to tell
SI2017	Light reddish brown	Yes, columns	Subangular/angular	Possible frosting, too difficult to tell
SI2018	Light reddish brown	Yes, columns	Subangular/subrounded	Possible frosting, too difficult to tell
SI2116	Yellowish red	Yes, columns	Angular/subangular	Yes, very dull
SI2117	Reddish yellow	Yes, columns	Subangular/subrounded	Yes, very dull
SI2118A	Light reddish brown	No	Subrounded/subangular	Yes, with some outliers
SI2118B	Reddish brown	Yes	Subrounded/subangular	yes
SI2119A	Reddish brown	Yes, columns	Round/subrounded	Yes, with some outliers
SI2119B	Red	Yes, columns	Subrounded/subangular	yes

APPENDIX E. SEDIMENT PROFILES
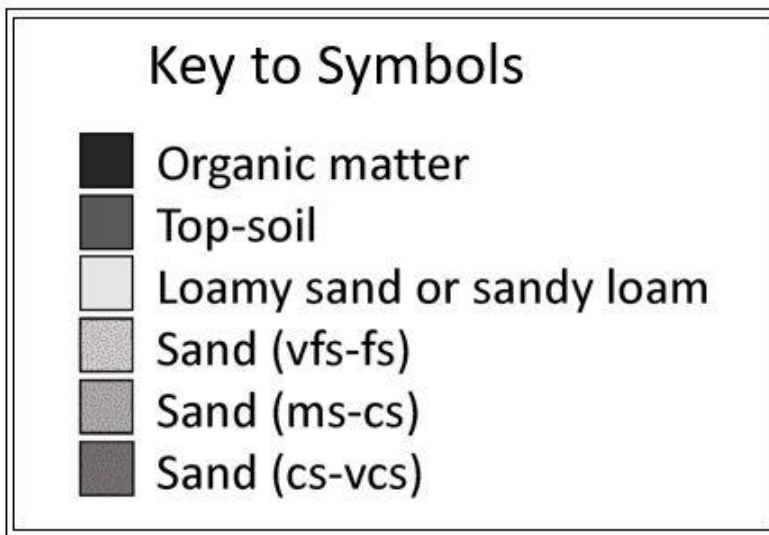
Figure E1. Key to sediment profile symbols.
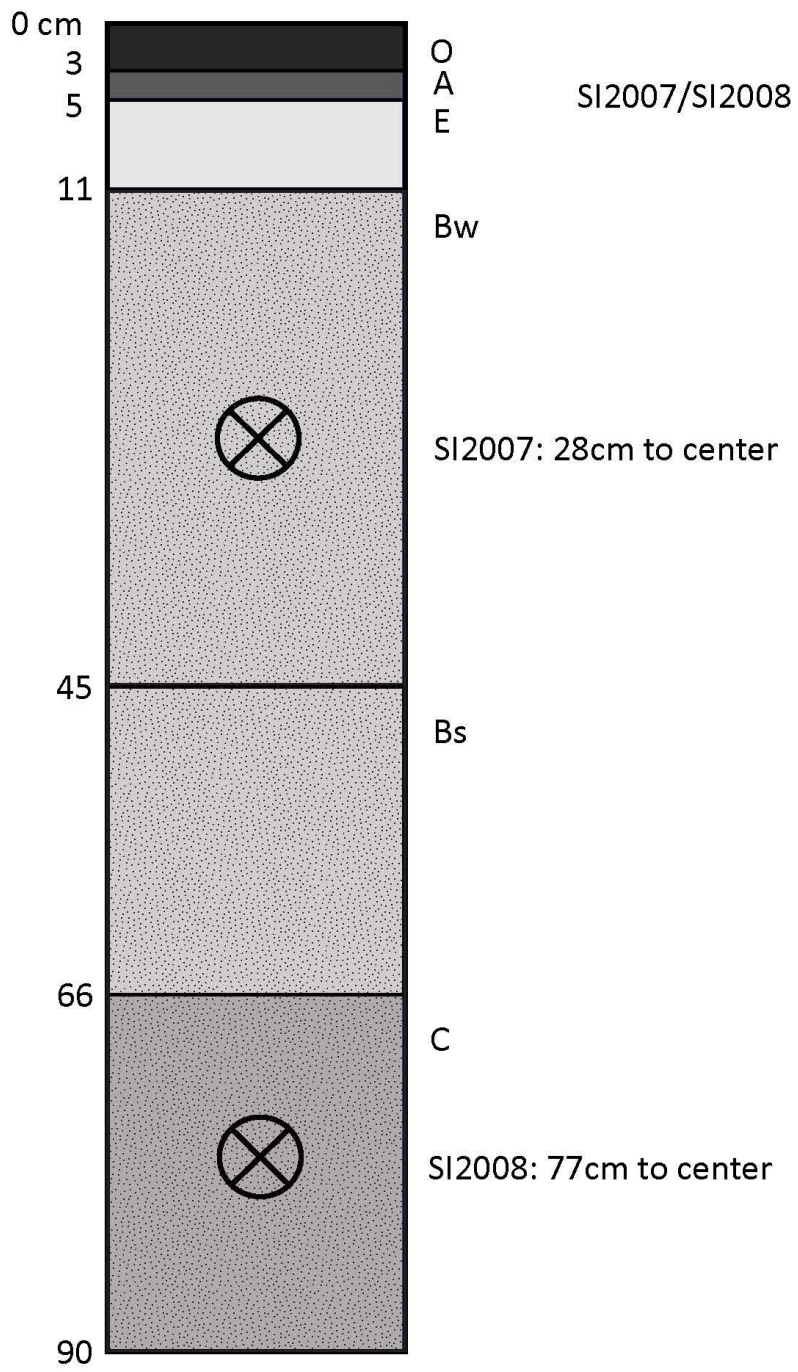
Figure E2. Sediment profile for samples SI2007 and SI2008.
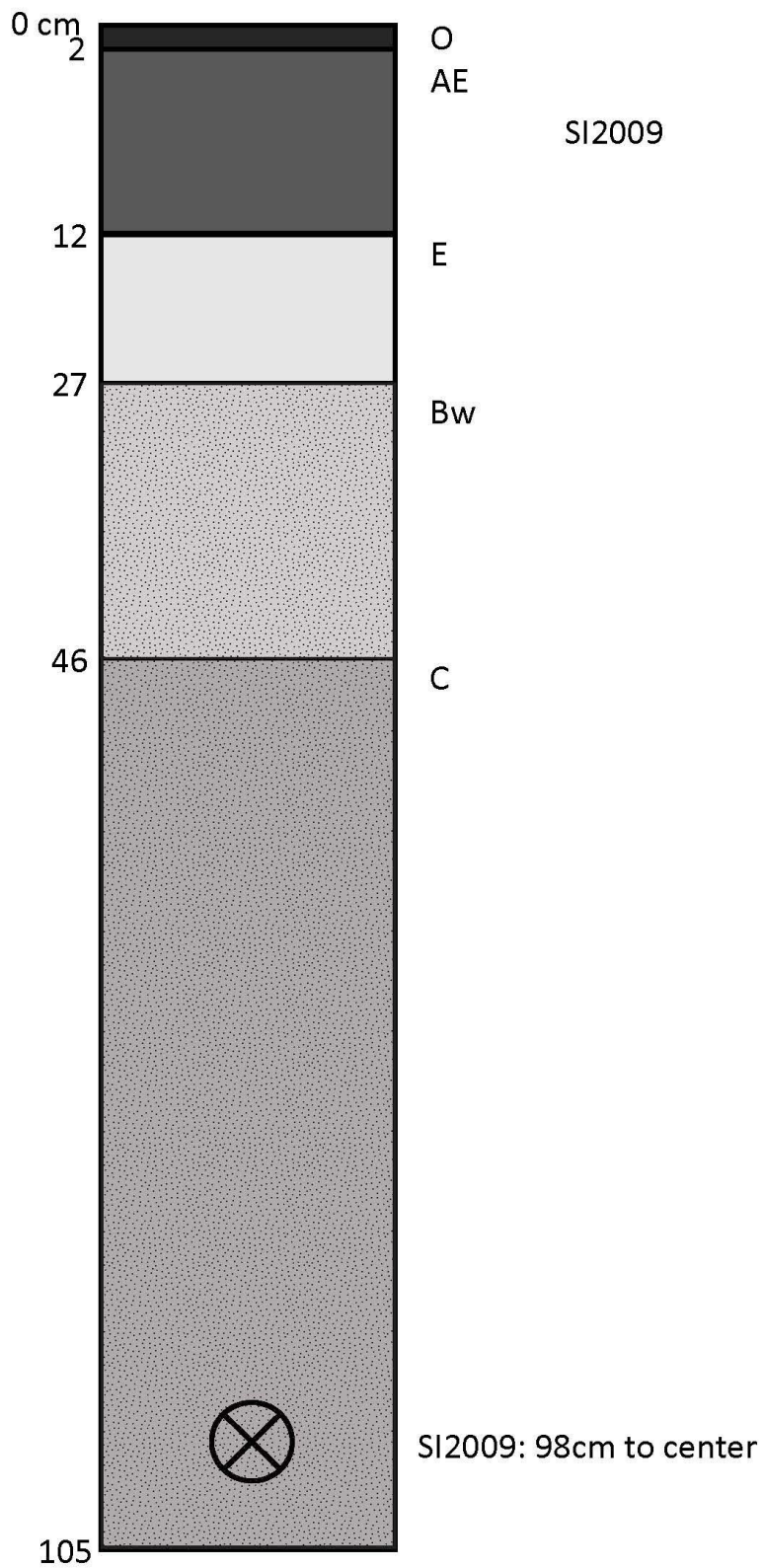
Figure E3. Sediment profile for sample SI2009.
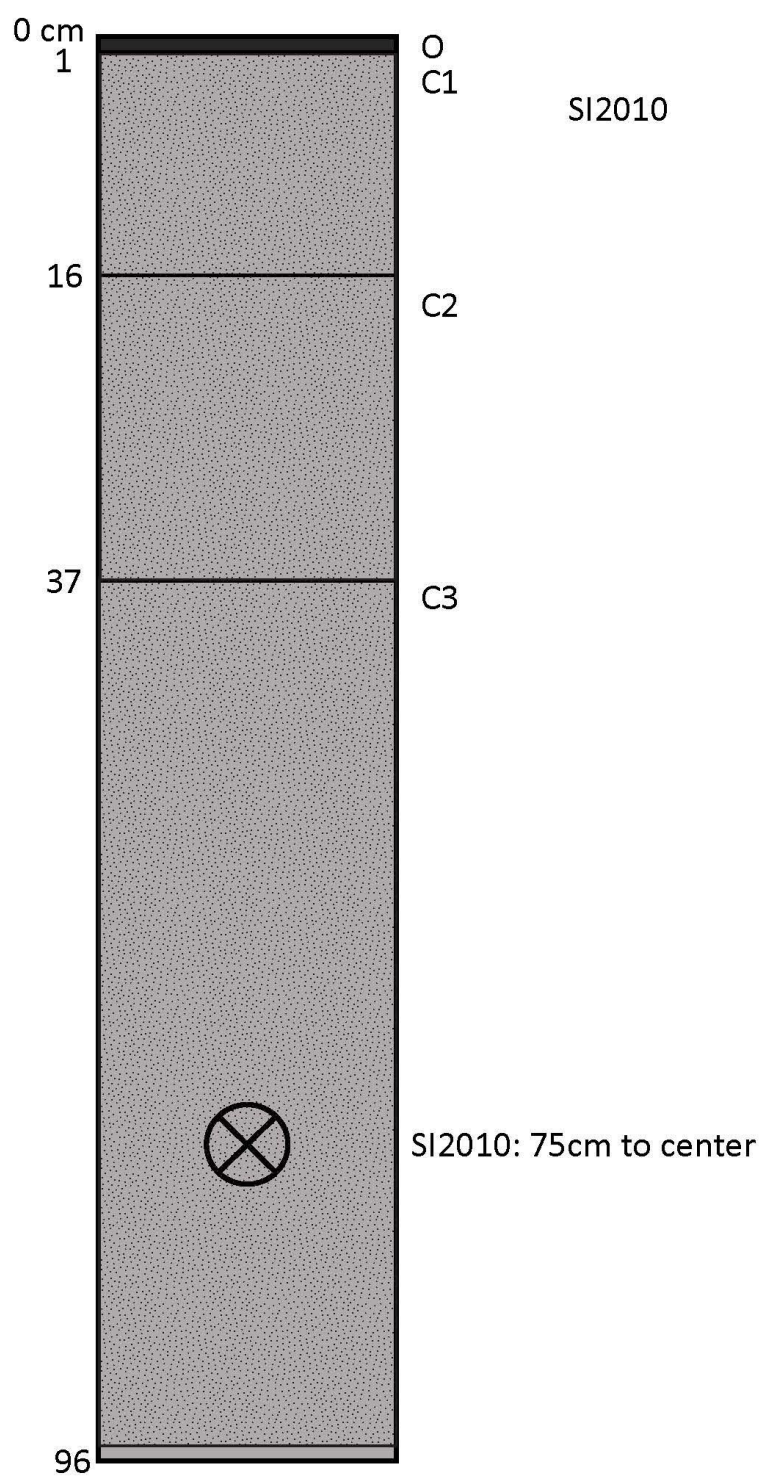
Figure E4. Sediment profile for sample SI2010.
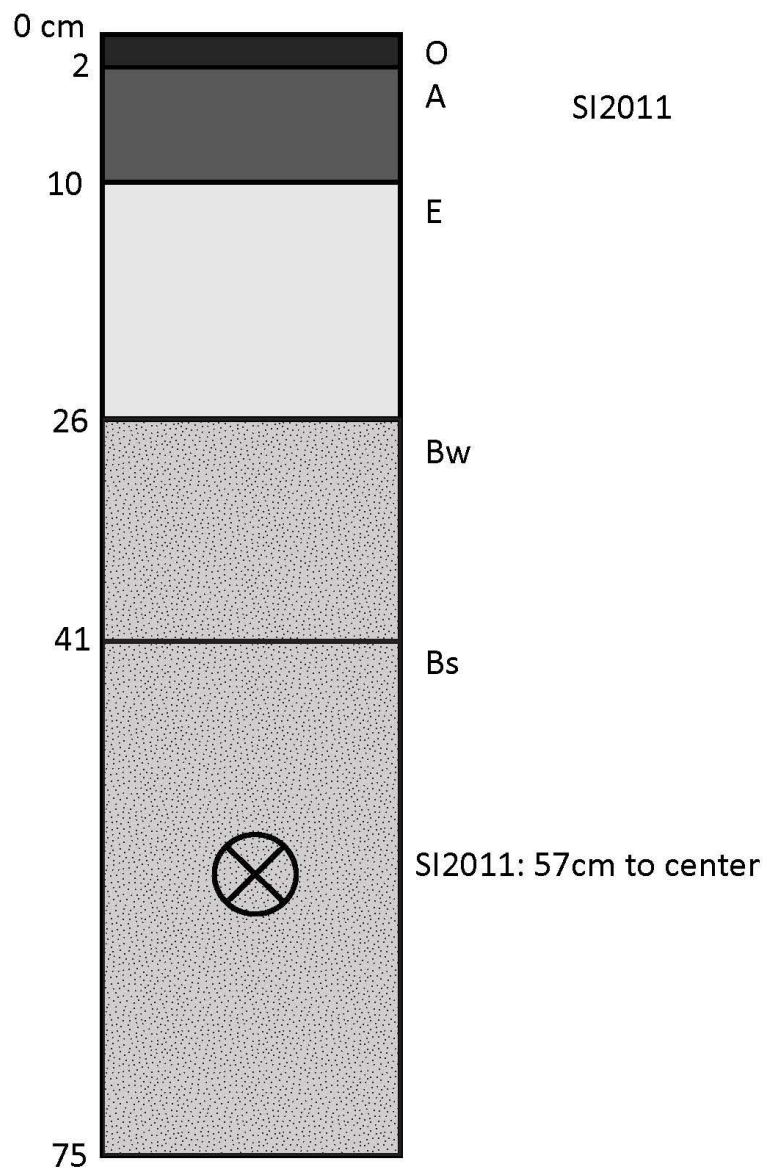
Figure E5. Sediment profile for sample SI2011.
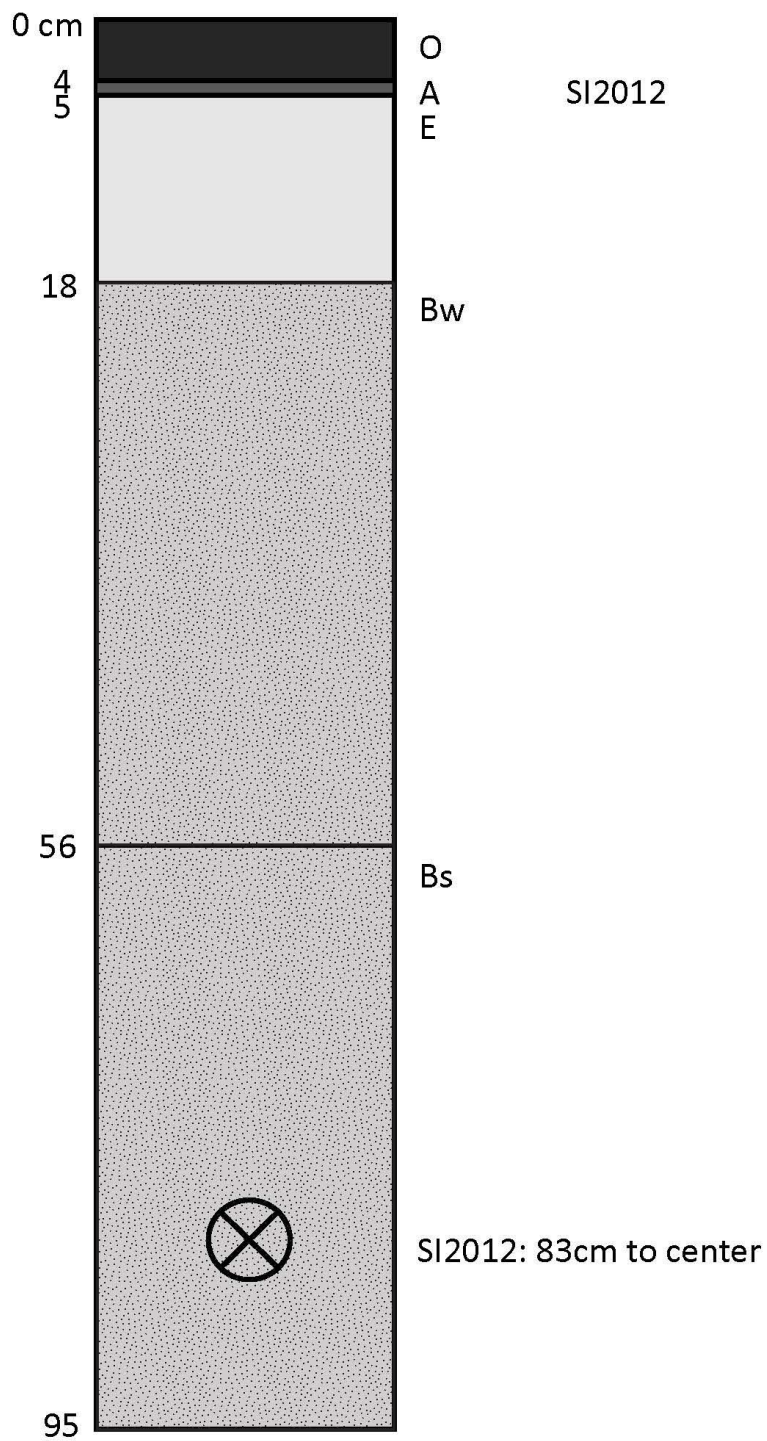
Figure E6. Sediment profile for sample SI2012.
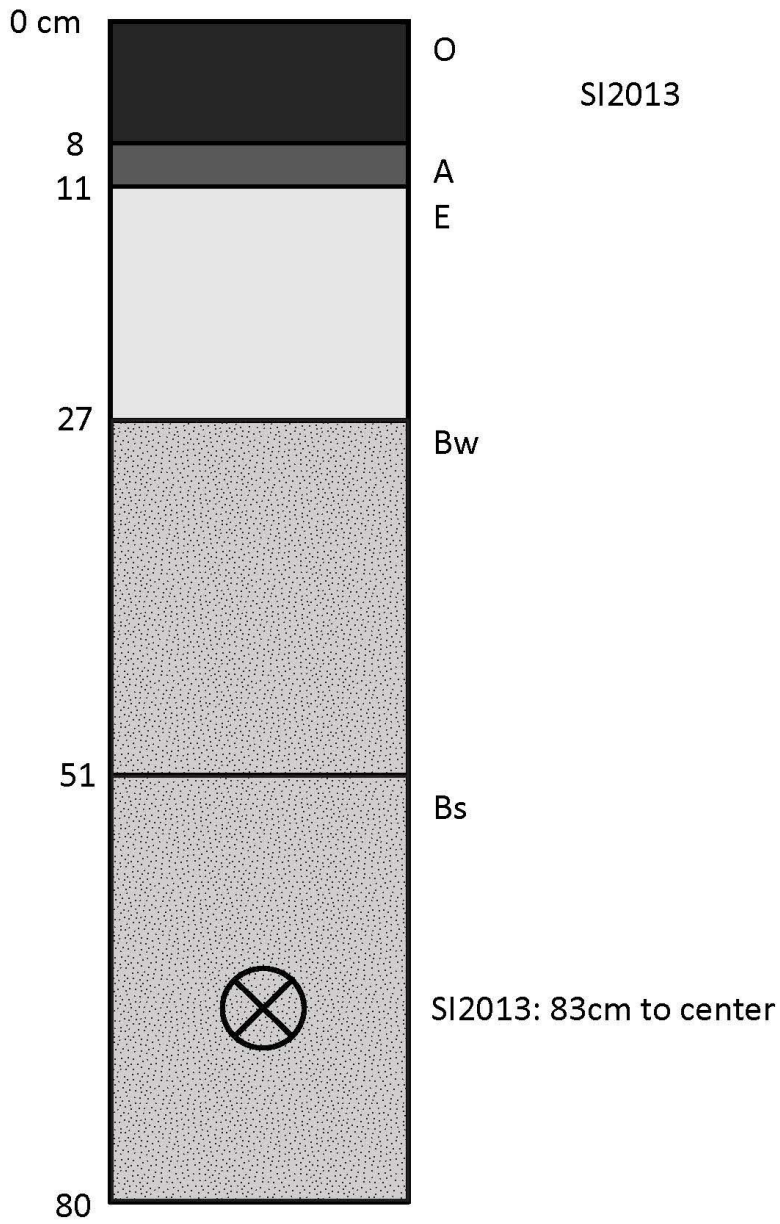
Figure E7. Sediment profile for sample SI2013.
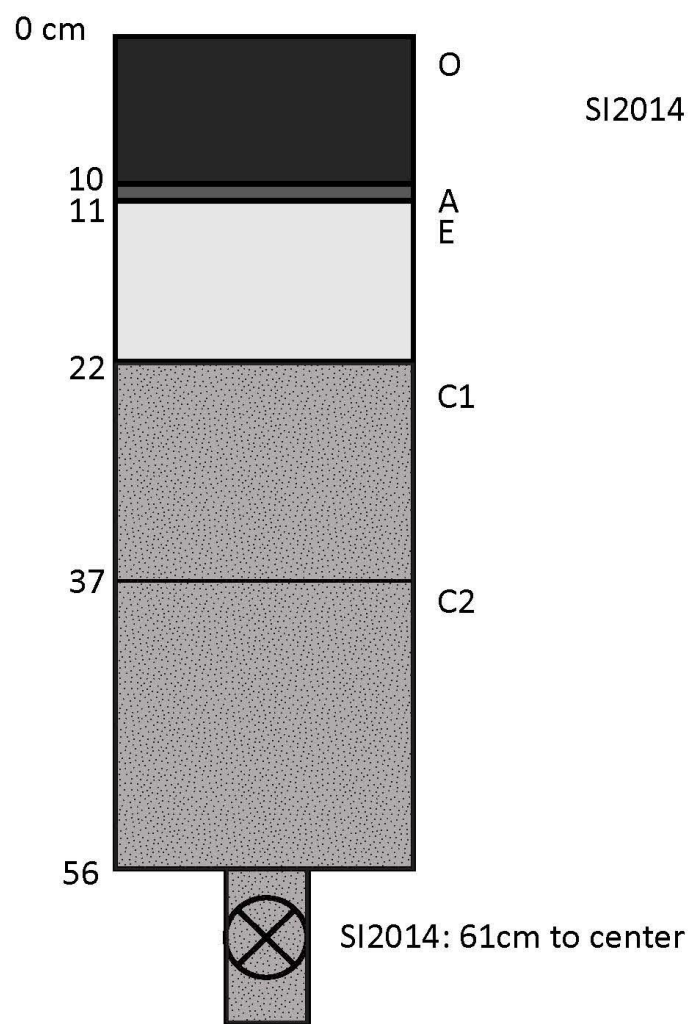
Figure E8. Sediment profile for sample SI2014.
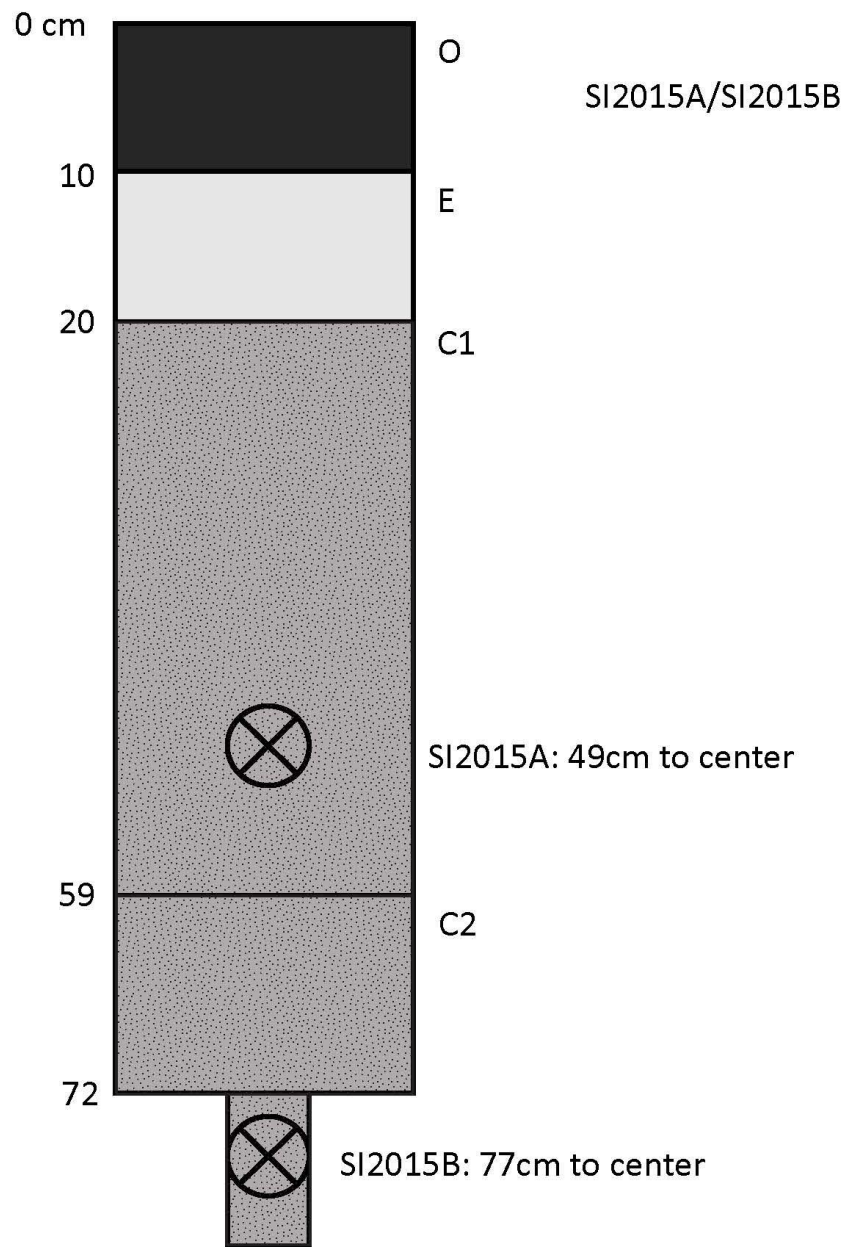
Figure E9. Sediment profile for samples SI2015A and SI2015B.
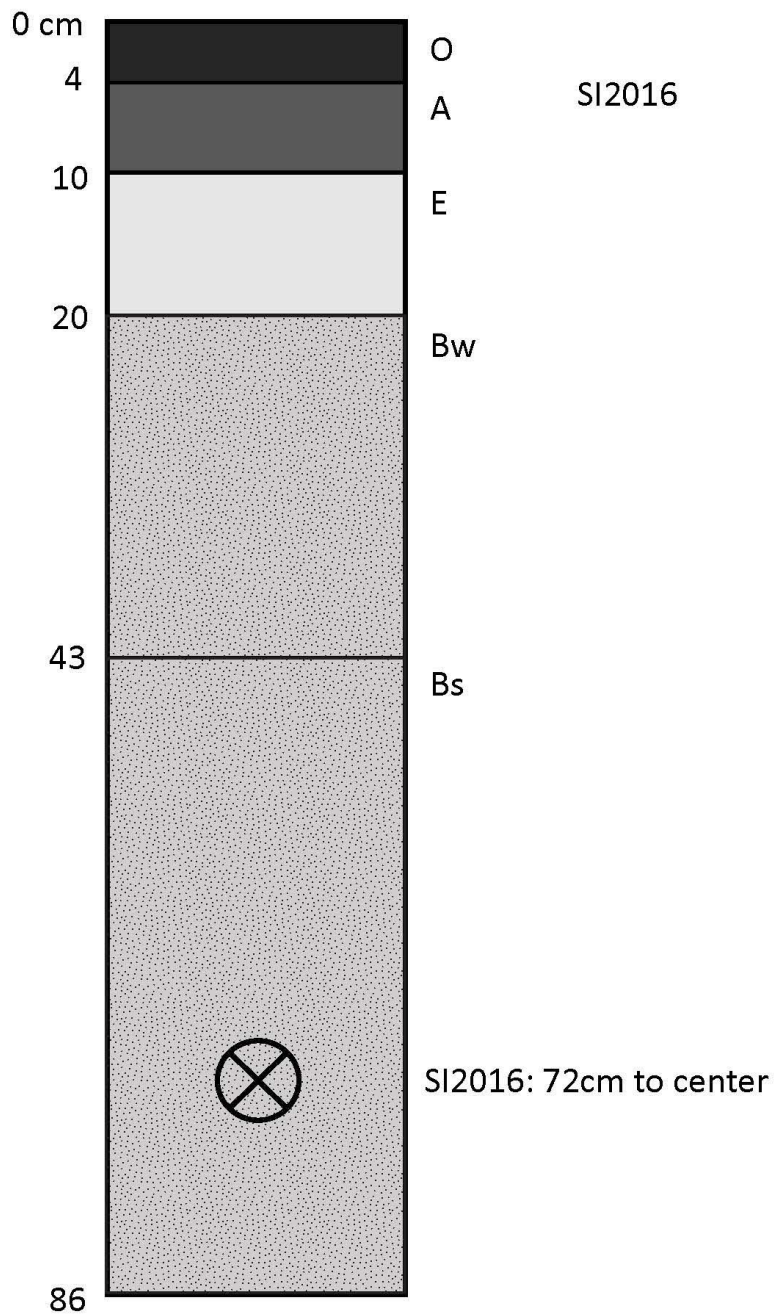
Figure E10. Sediment profile for sample SI2016.
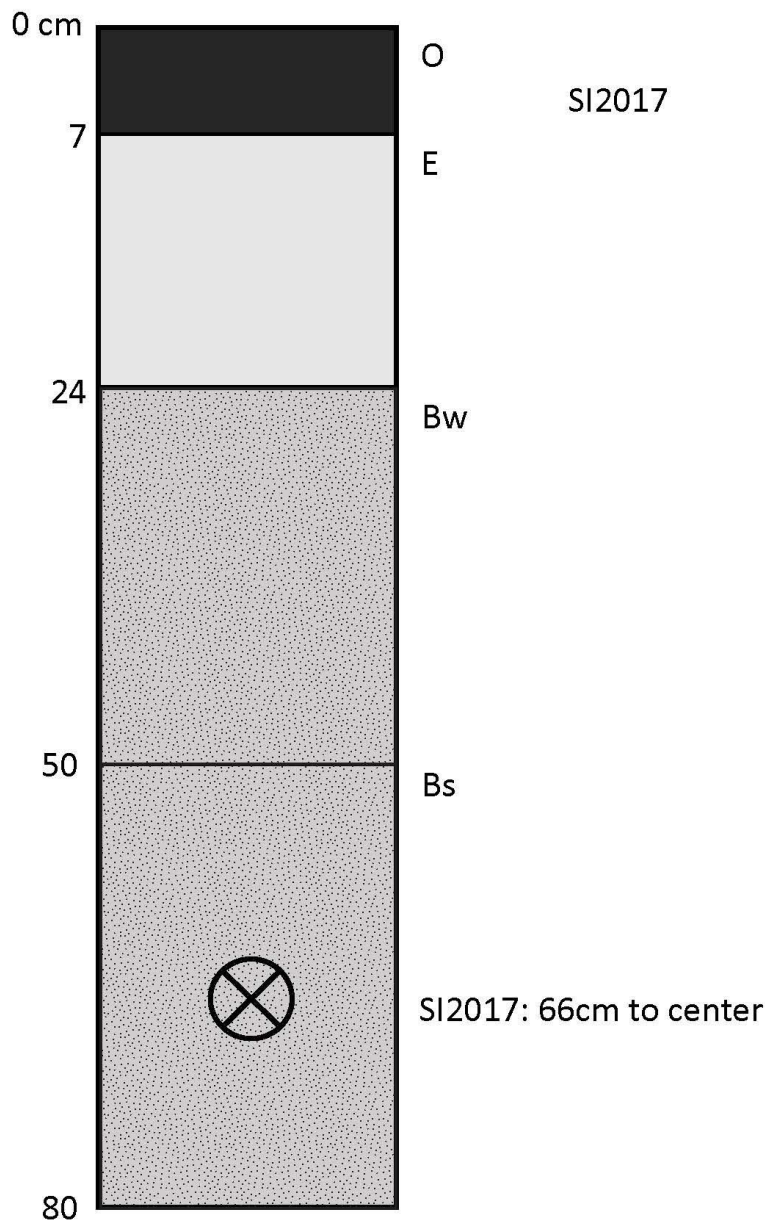
Figure E11. Sediment profile for sample SI2017.
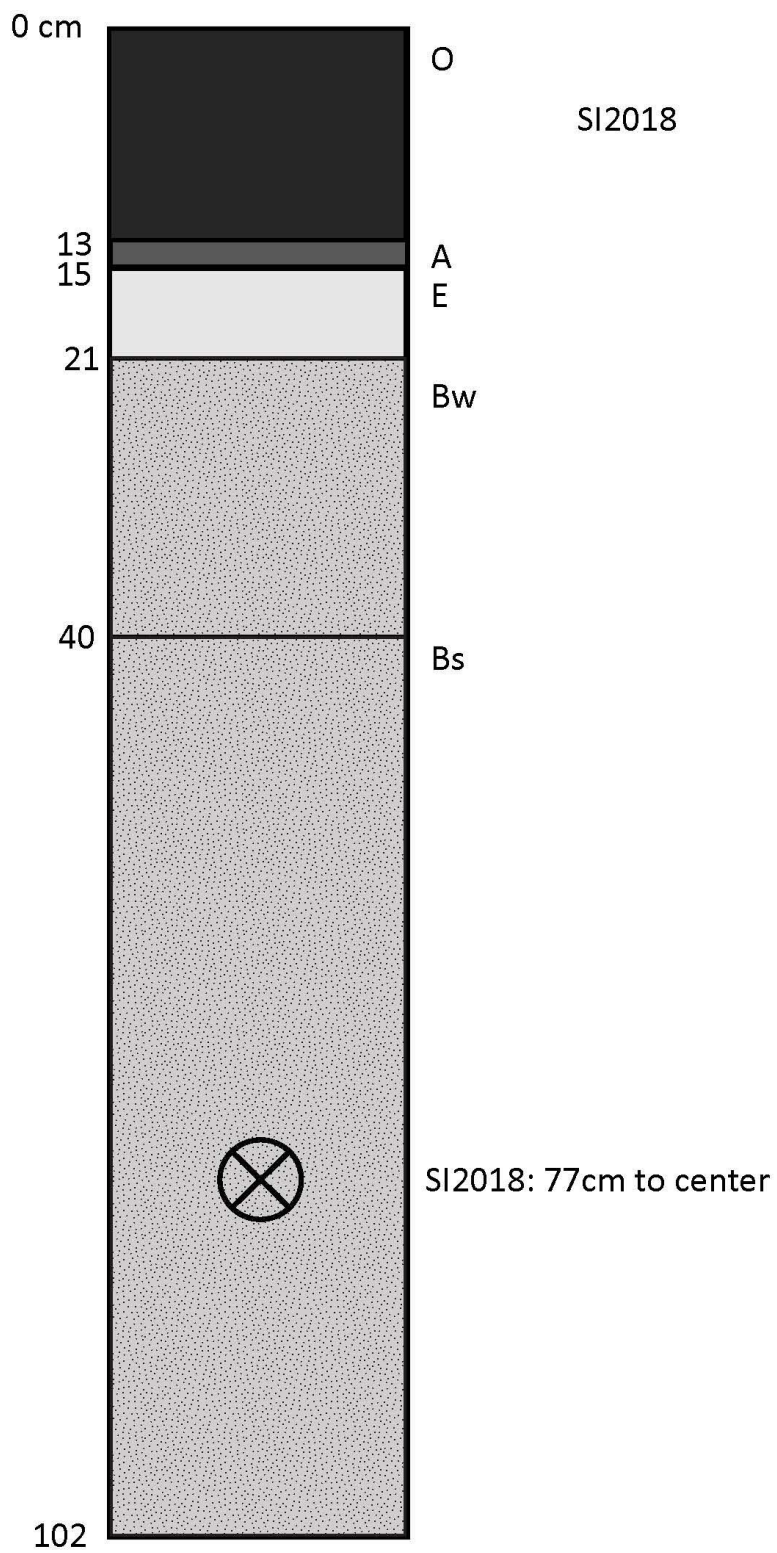
Figure E12. Sediment profile for sample SI2018.
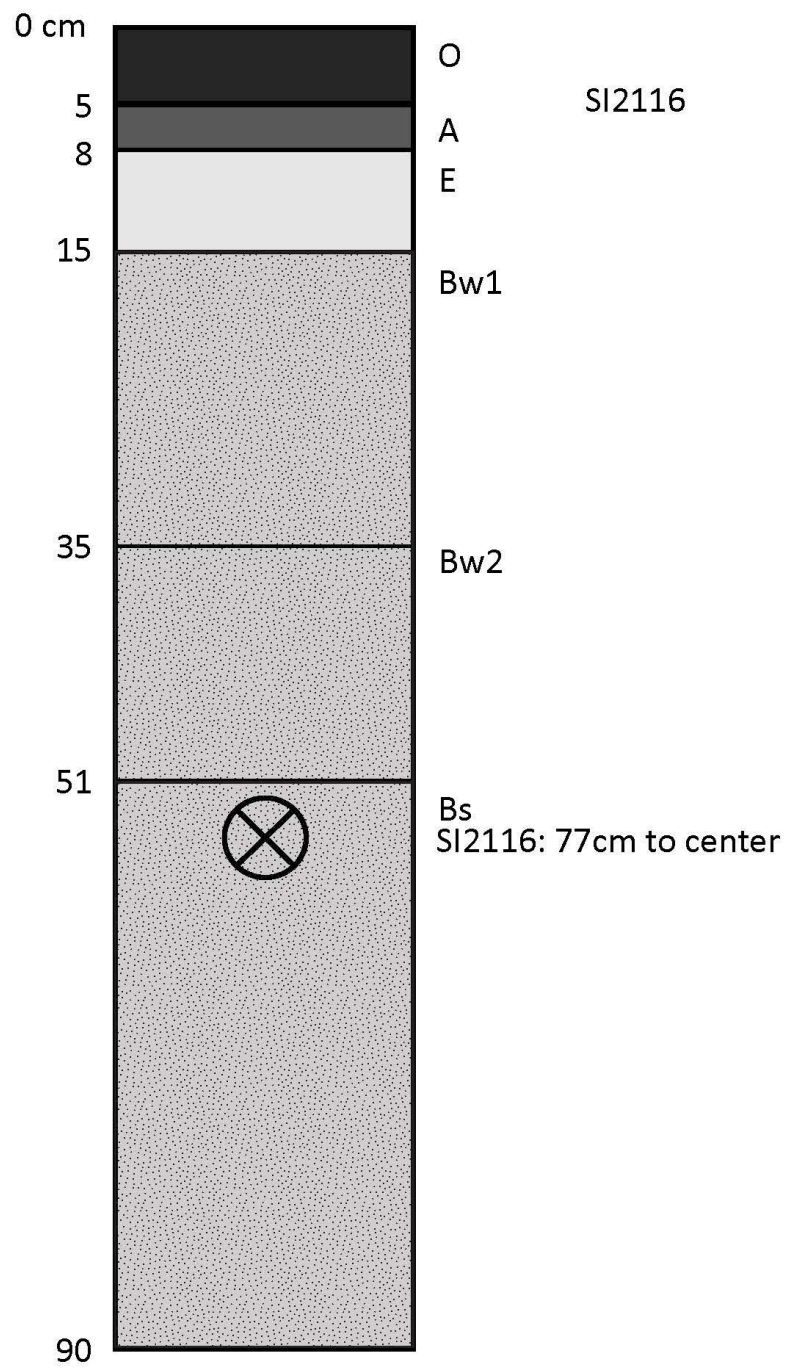
Figure E13. Sediment profile for sample SI2116.
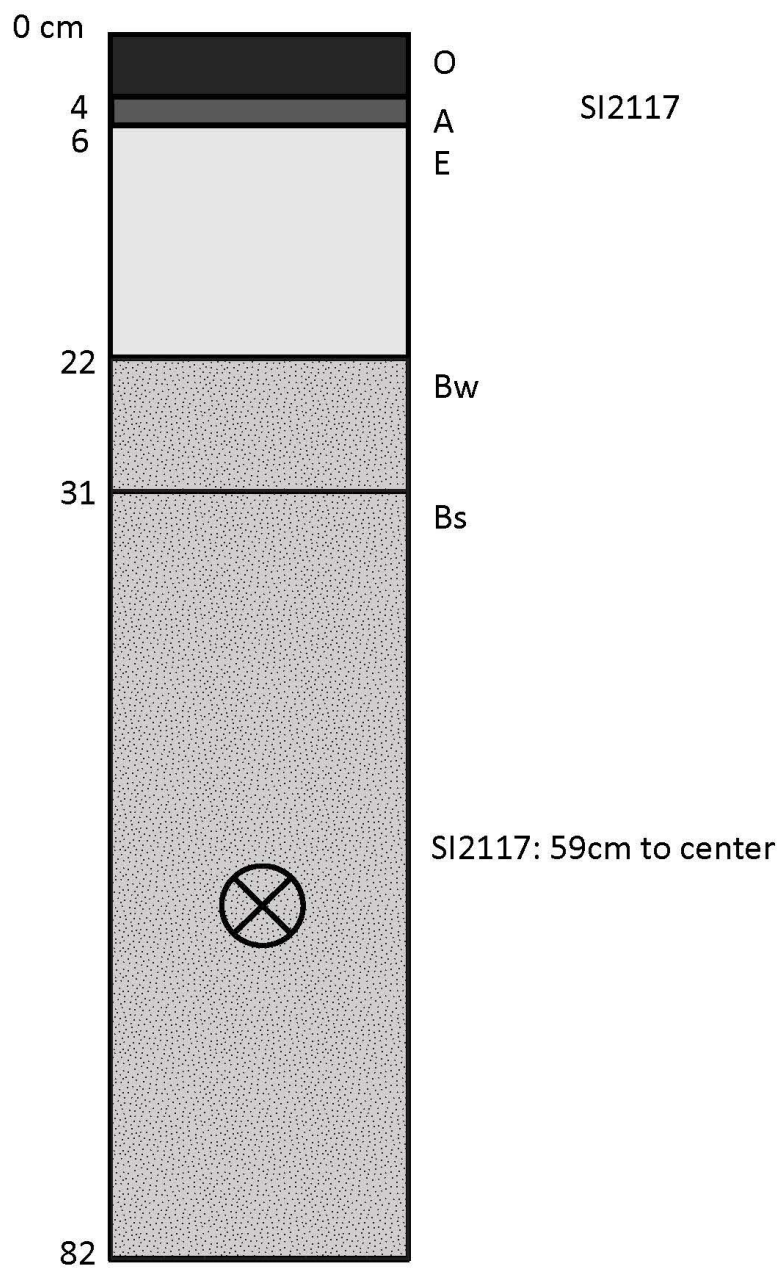
Figure E14. Sediment profile for sample SI2117.
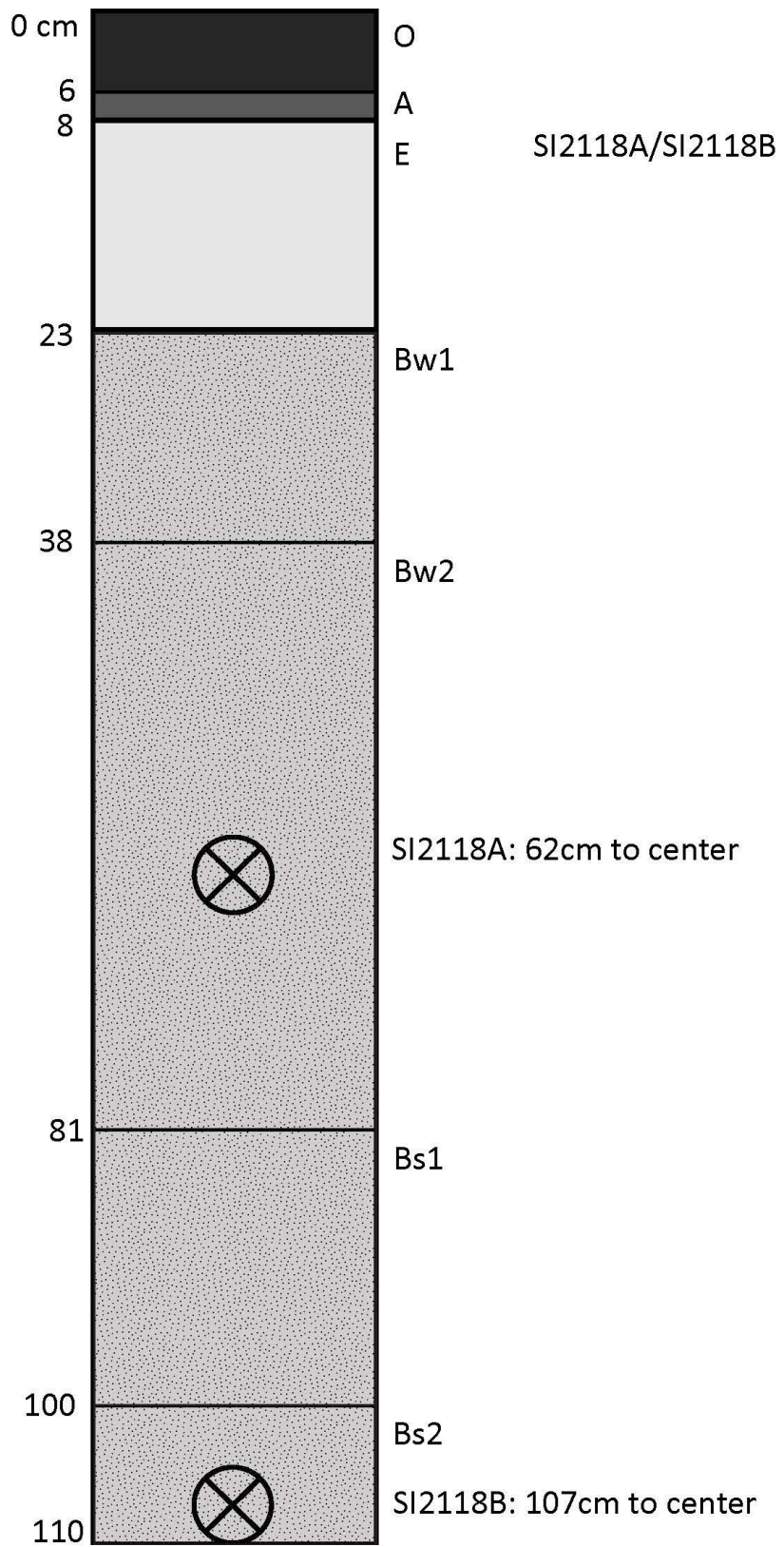
Figure E15. Sediment profile for samples SI2118A and SI2118B.
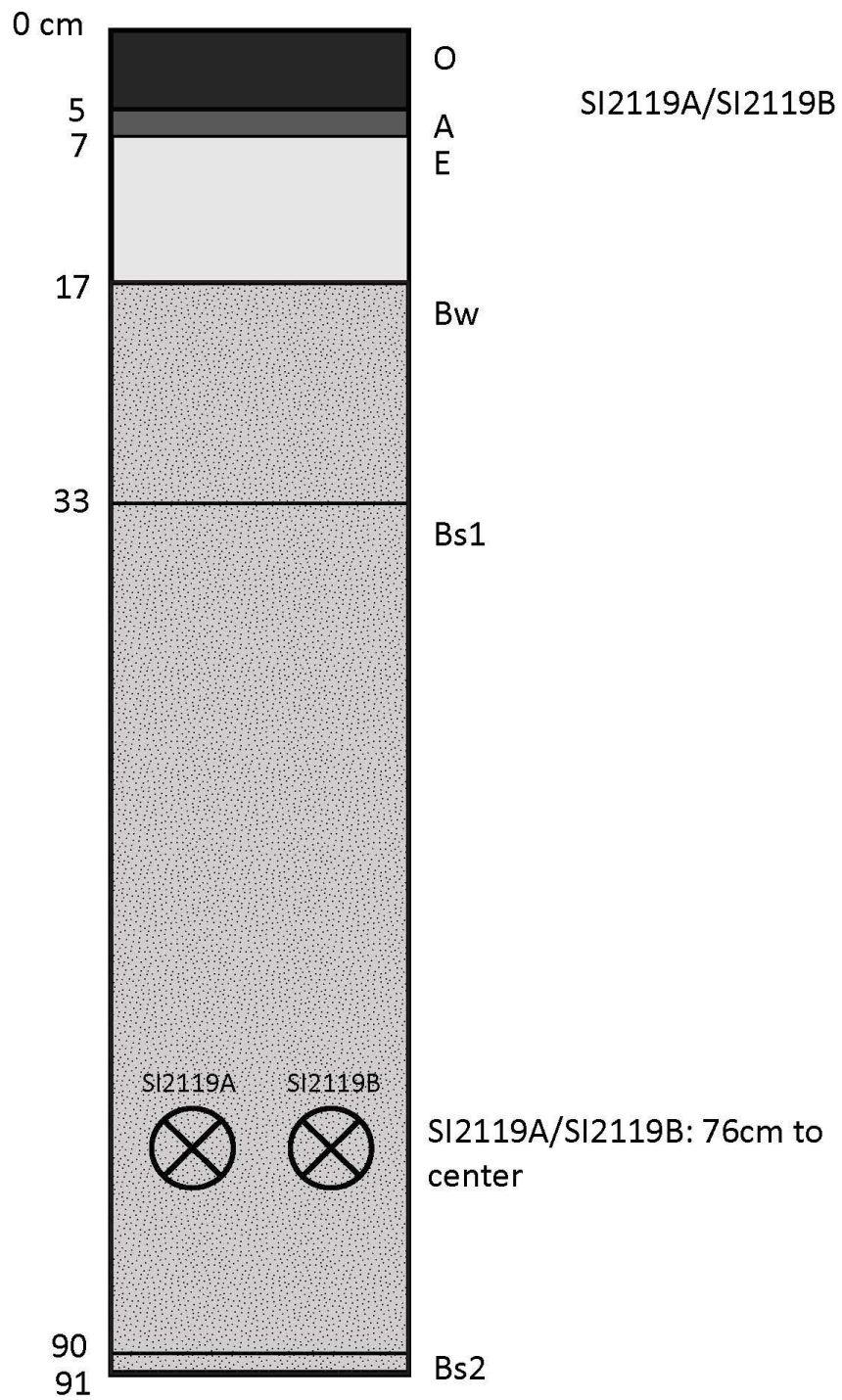
Figure E16. Sediment profile for samples SI2119A and SI2119B.

APPENDIX F. EQUIVALENT DOSE DISTRIBUTION DATA
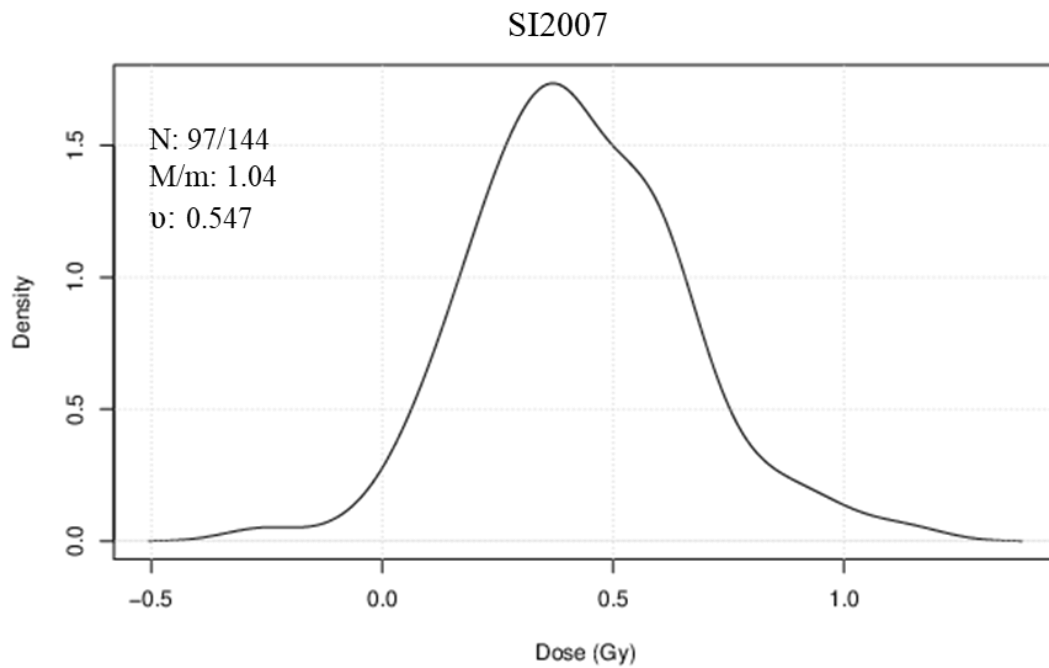
Figure F1. Equivalent dose distribution for sample SI2007 plotted as probability density. Computed by Gaussian kernel density estimation (Wessa, 2015).
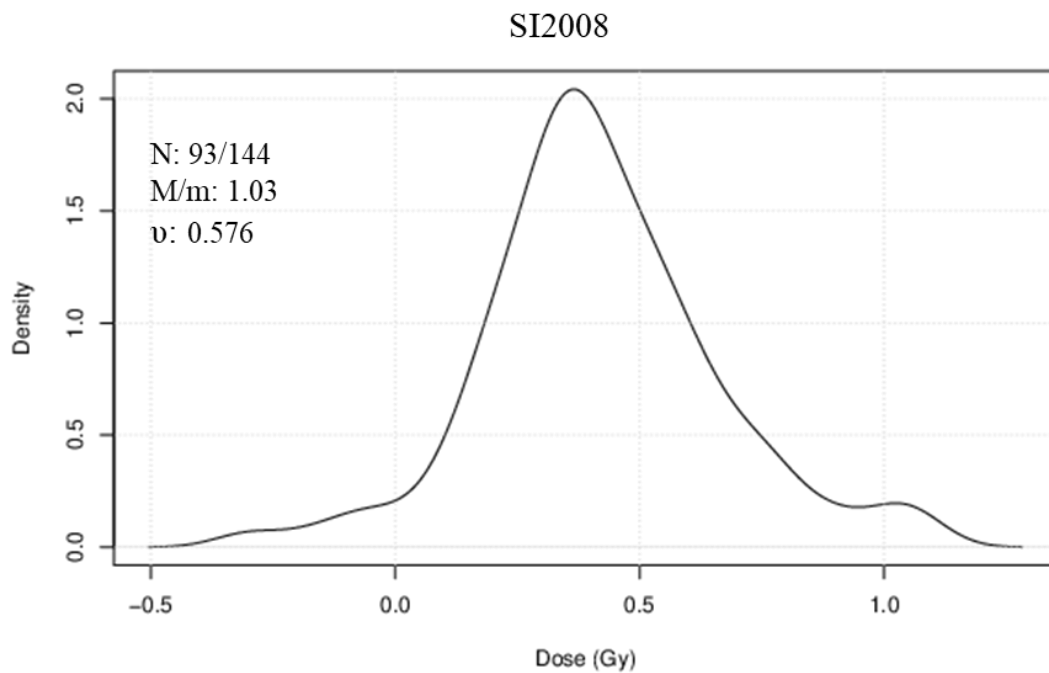
Figure F2. Equivalent dose distribution for sample SI2008 plotted as probability density. Computed by Gaussian kernel density estimation (Wessa, 2015).

84
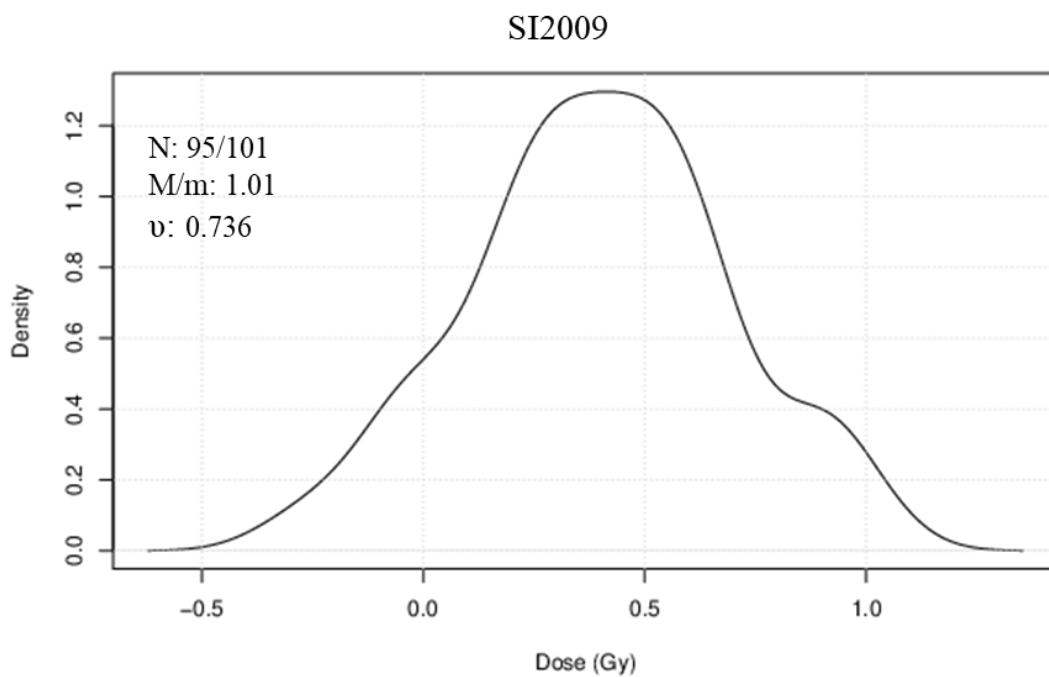
Figure F3. Equivalent dose distribution for sample SI2009 plotted as probability density. Computed by Gaussian kernel density estimation (Wessa, 2015).
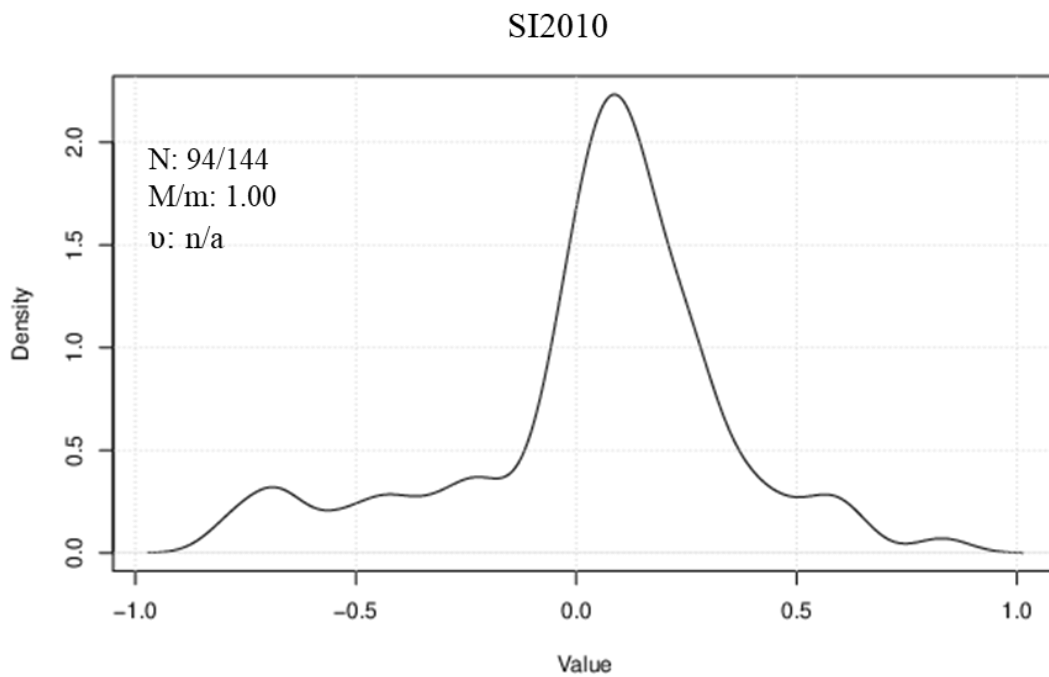
Figure F4. Equivalent dose distribution for sample SI2010 plotted as probability density. Computed by Gaussian kernel density estimation (Wessa, 2015).

SI2011MS

N: 73/96
M/m: 1.06
υ: 0.520
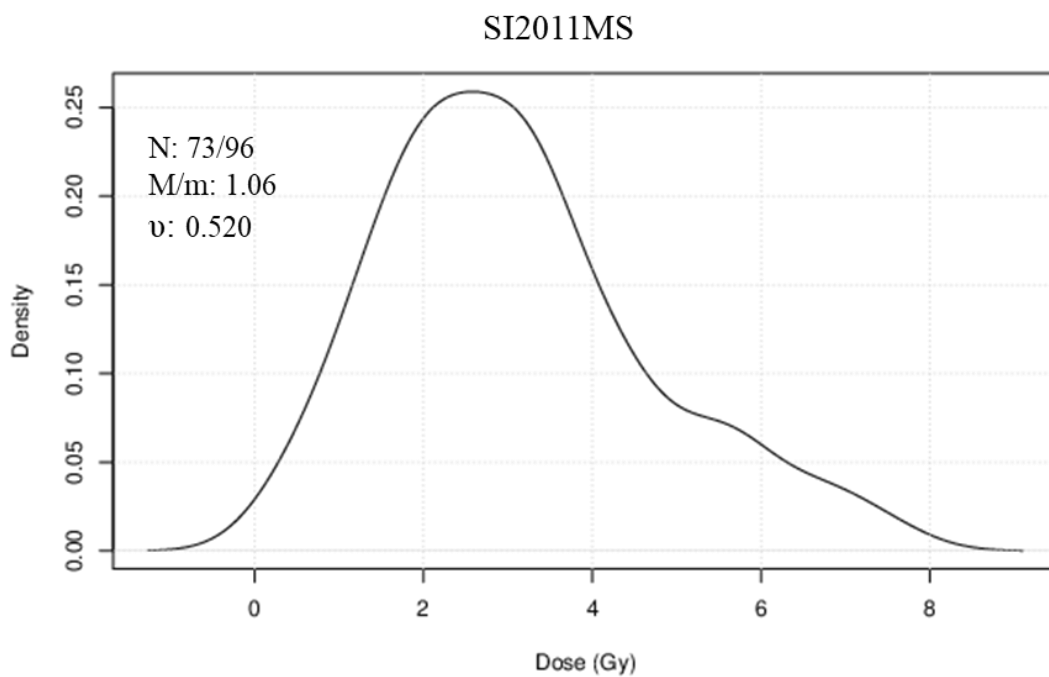
Figure F5. Equivalent dose distribution for sample SI2011 plotted as probability density. Computed by Gaussian kernel density estimation (Wessa, 2015).

SI2012MS

N: 77/96
M/m: 1.15
υ: 0.617
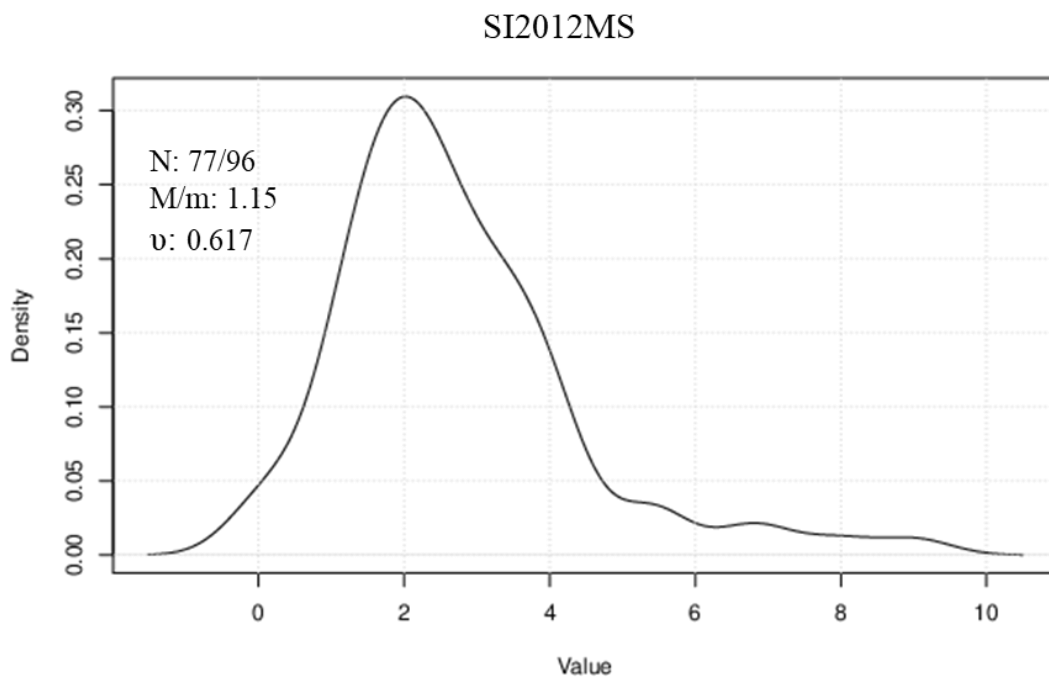
Figure F6. Equivalent dose distribution for sample SI2012 plotted as probability density. Computed by Gaussian kernel density estimation (Wessa, 2015).

SI2013

N: 80/89
M/m: 1.06
υ: 0.372
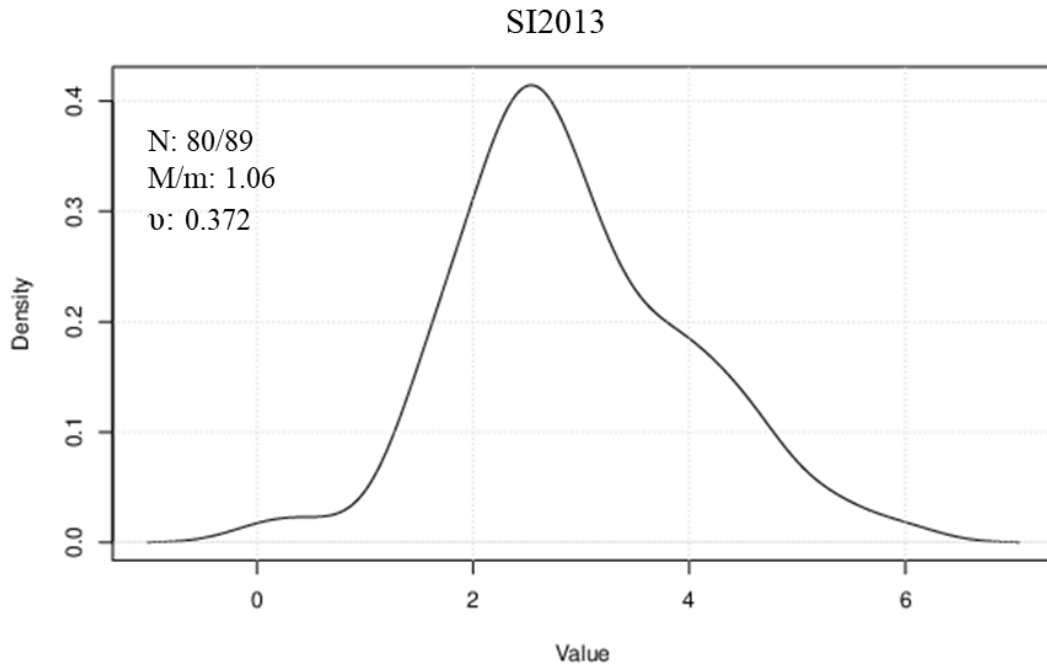
Figure F7. Equivalent dose distribution for sample SI2013 plotted as probability density. Computed by Gaussian kernel density estimation (Wessa, 2015).

SI2014

N: 94/96
M/m: 1.01
υ: 0.300
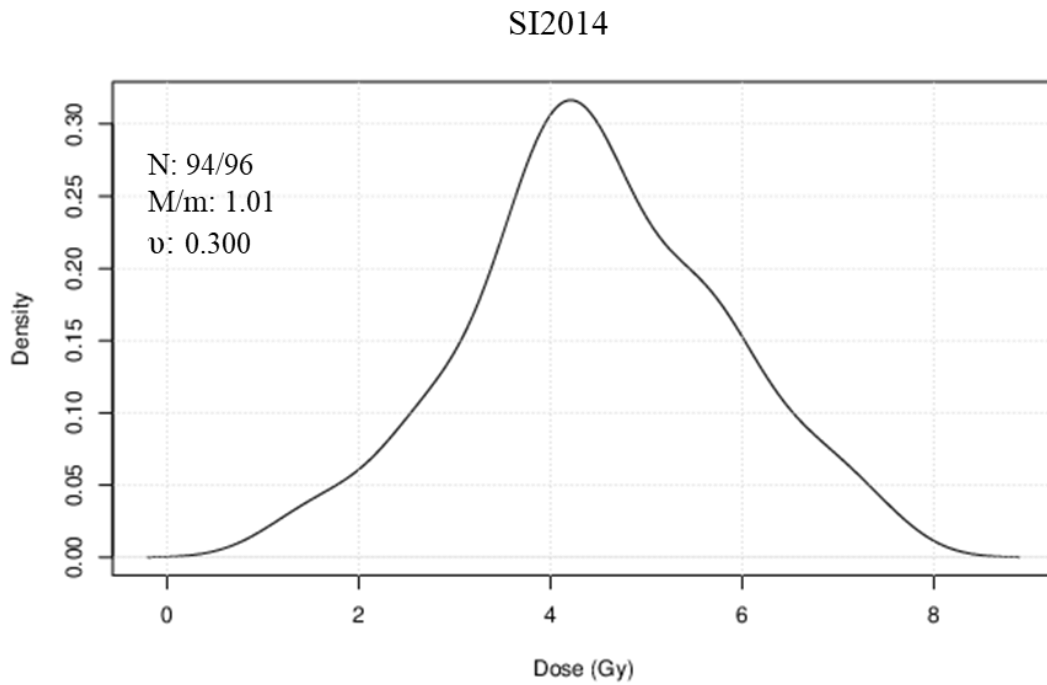
Figure F8. Equivalent dose distribution for sample SI2014 plotted as probability density. Computed by Gaussian kernel density estimation (Wessa, 2015).
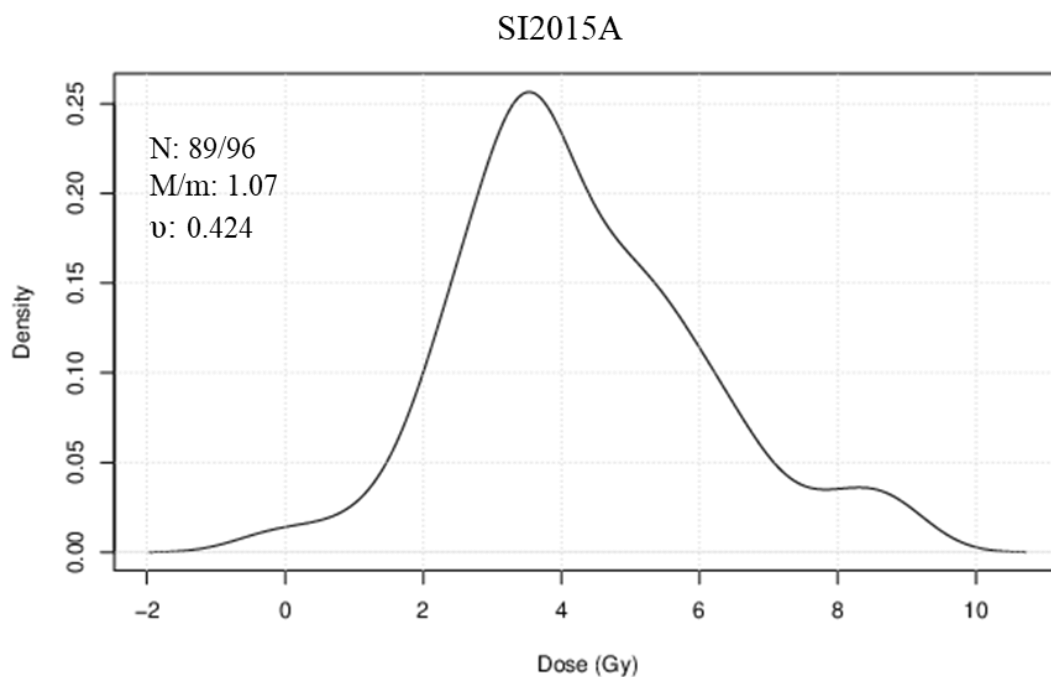
SI2015A

Figure F9. Equivalent dose distribution for sample SI2015A plotted as probability density. Computed by Gaussian kernel density estimation (Wessa, 2015).
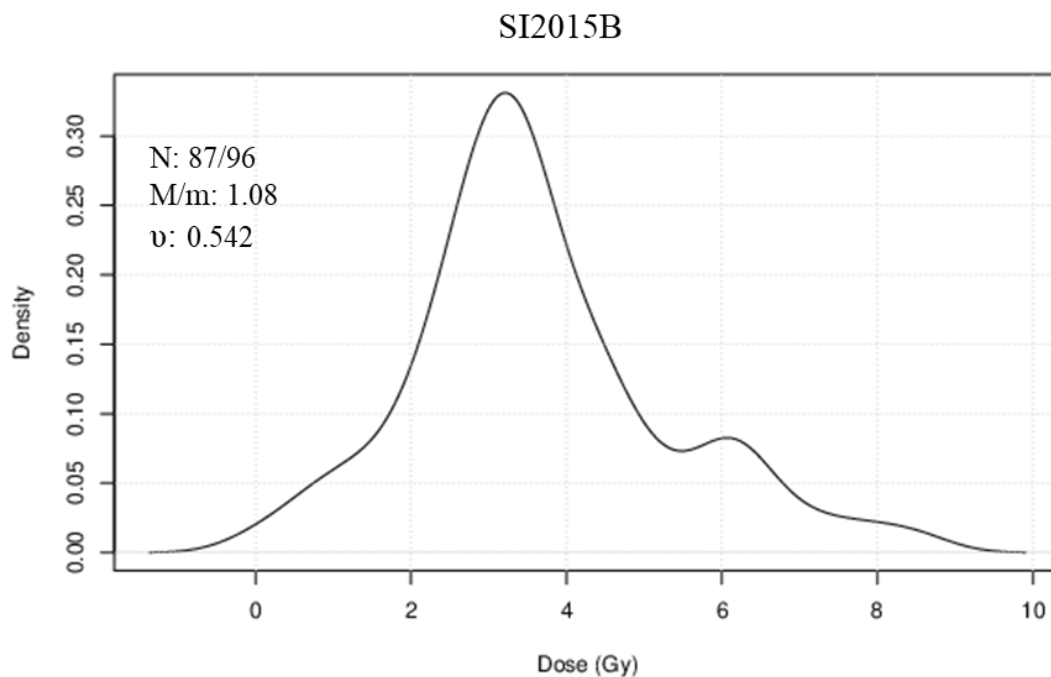
SI2015B

Figure F10. Equivalent dose distribution for sample SI2015B plotted as probability density. Computed by Gaussian kernel density estimation (Wessa, 2015).
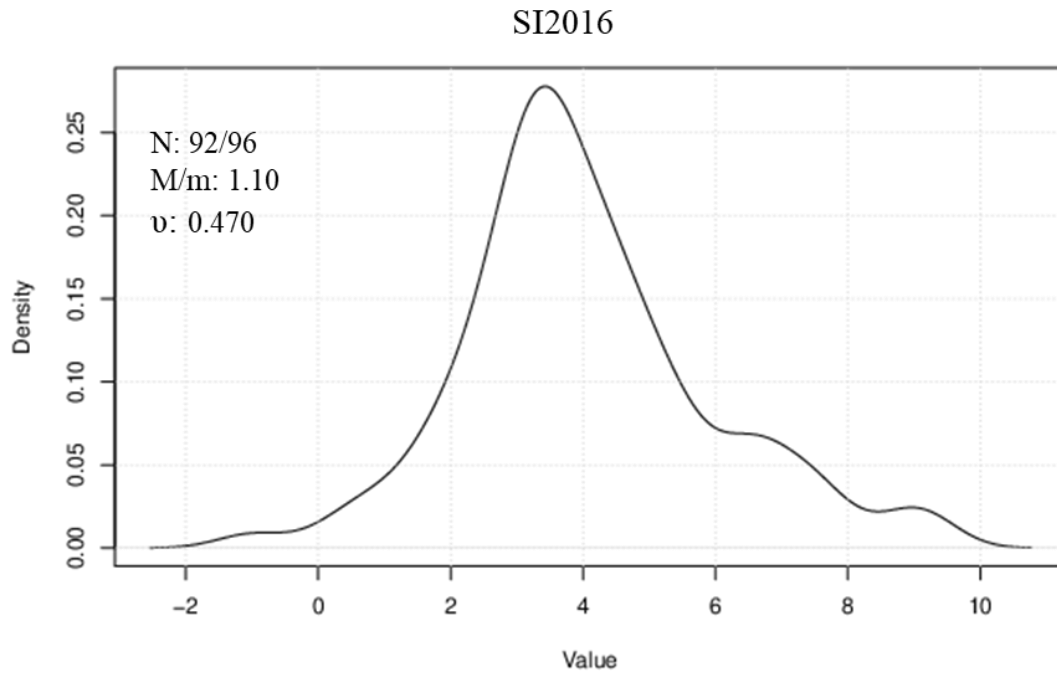
Figure F11. Equivalent dose distribution for sample SI2016 plotted as probability density. Computed by Gaussian kernel density estimation (Wessa, 2015).
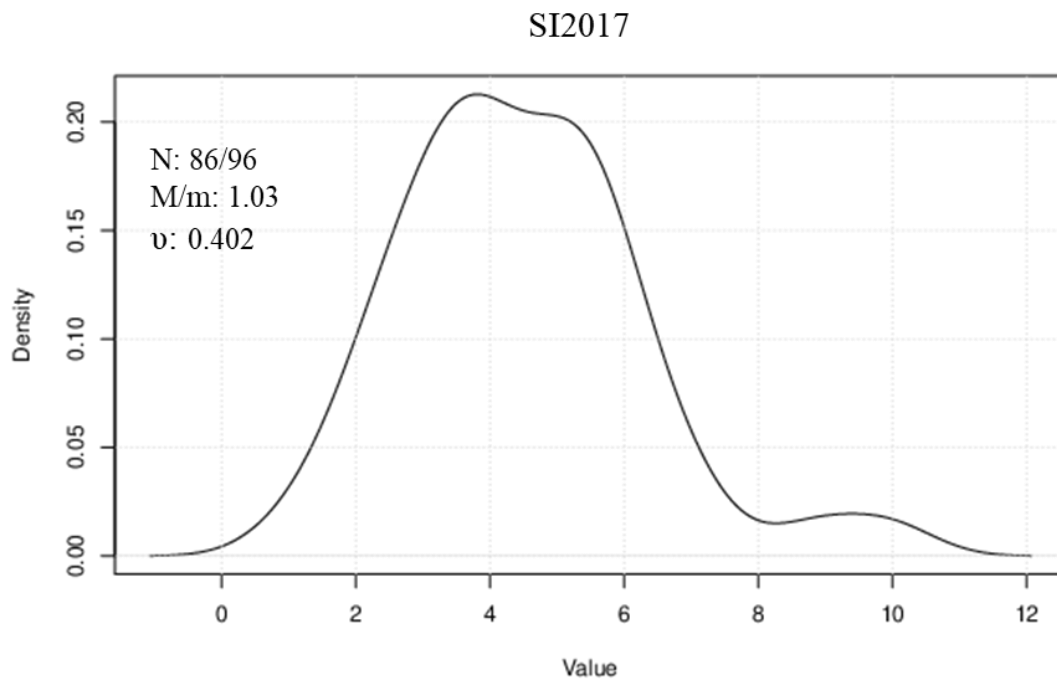
Figure F12. Equivalent dose distribution for sample SI2017 plotted as probability density. Computed by Gaussian kernel density estimation (Wessa, 2015).
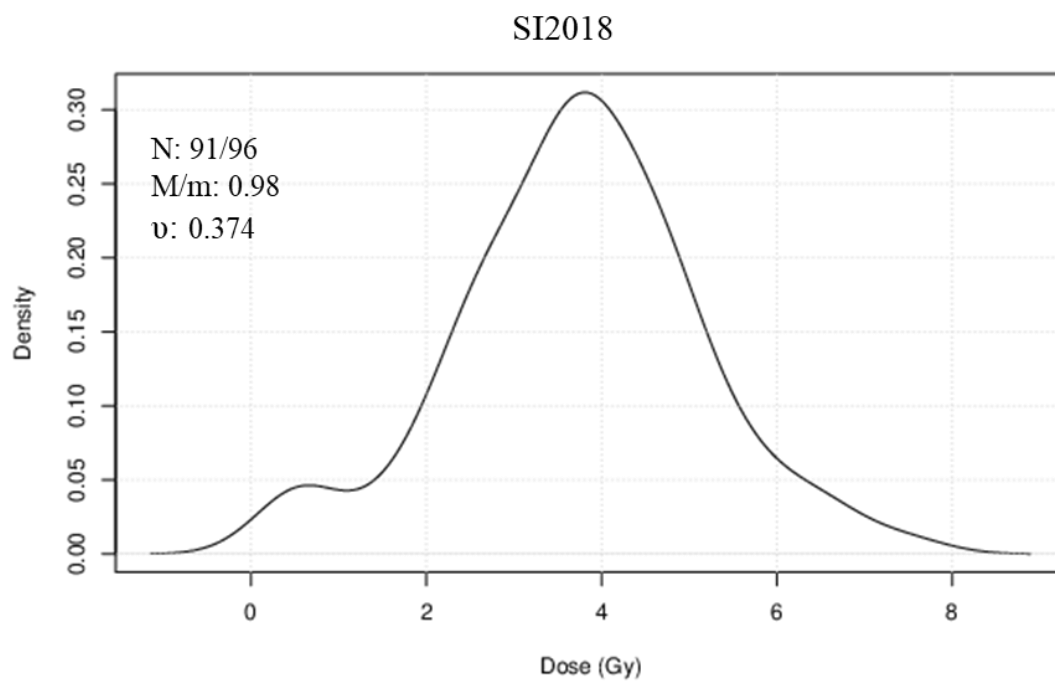
Figure F13. Equivalent dose distribution for sample SI2018 plotted as probability density. Computed by Gaussian kernel density estimation (Wessa, 2015).
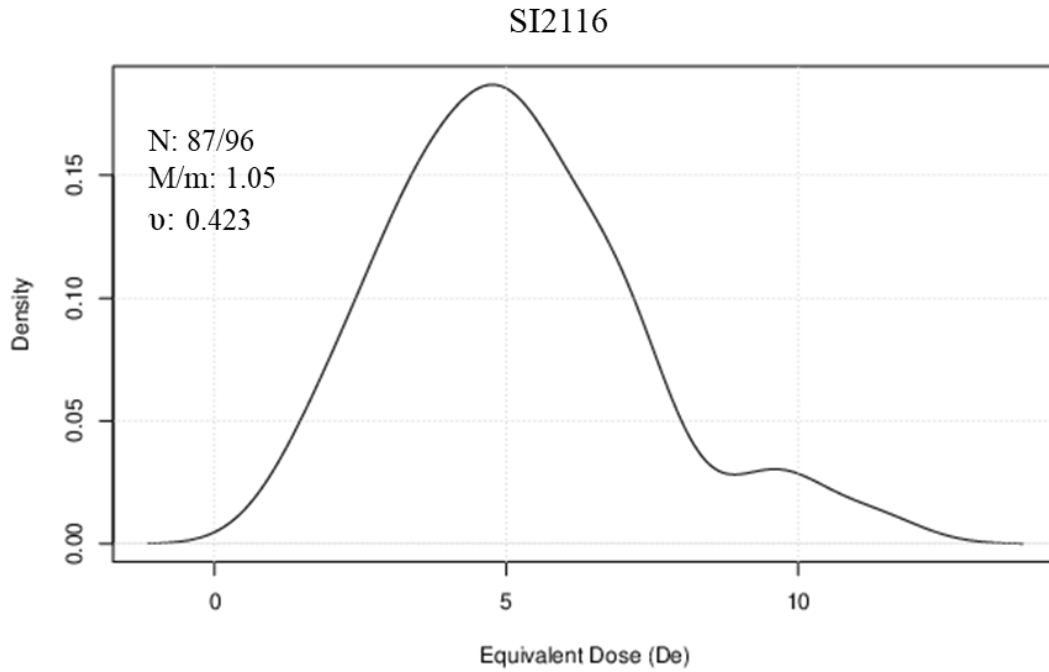
Figure F14. Equivalent dose distribution for sample SI2116 plotted as probability density. Computed by Gaussian kernel density estimation (Wessa, 2015).
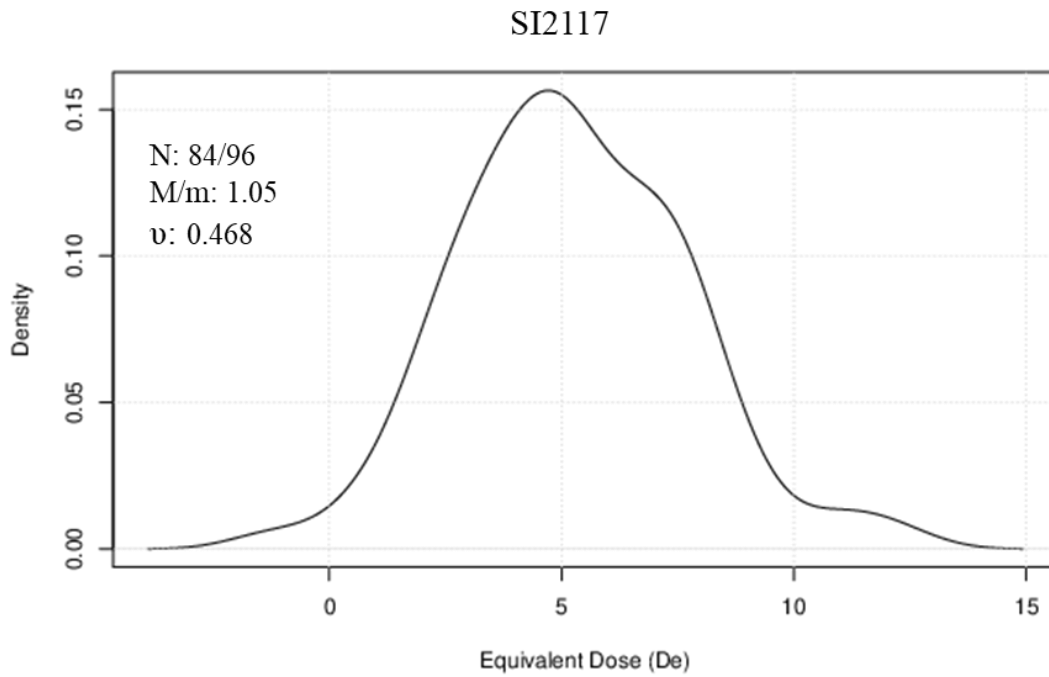
Figure F15. Equivalent dose distribution for sample SI2117 plotted as probability density. Computed by Gaussian kernel density estimation (Wessa, 2015).

SI2118A

N: 92/96
M/m: 1.05
υ: 0.349

Density

Dose (Gy)
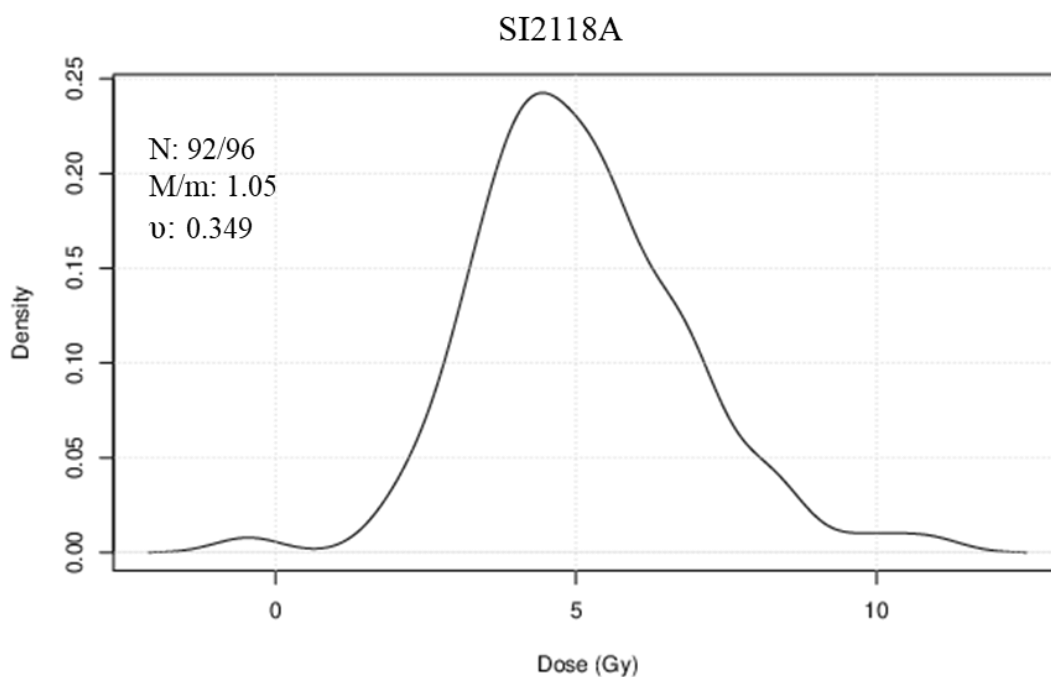
Figure F16. Equivalent dose distribution for sample SI2118A plotted as probability density. Computed by Gaussian kernel density estimation (Wessa, 2015).

SI2118B

N: 85/96
M/m: 0.95
υ: 0.427

Density

Dose (Gy)
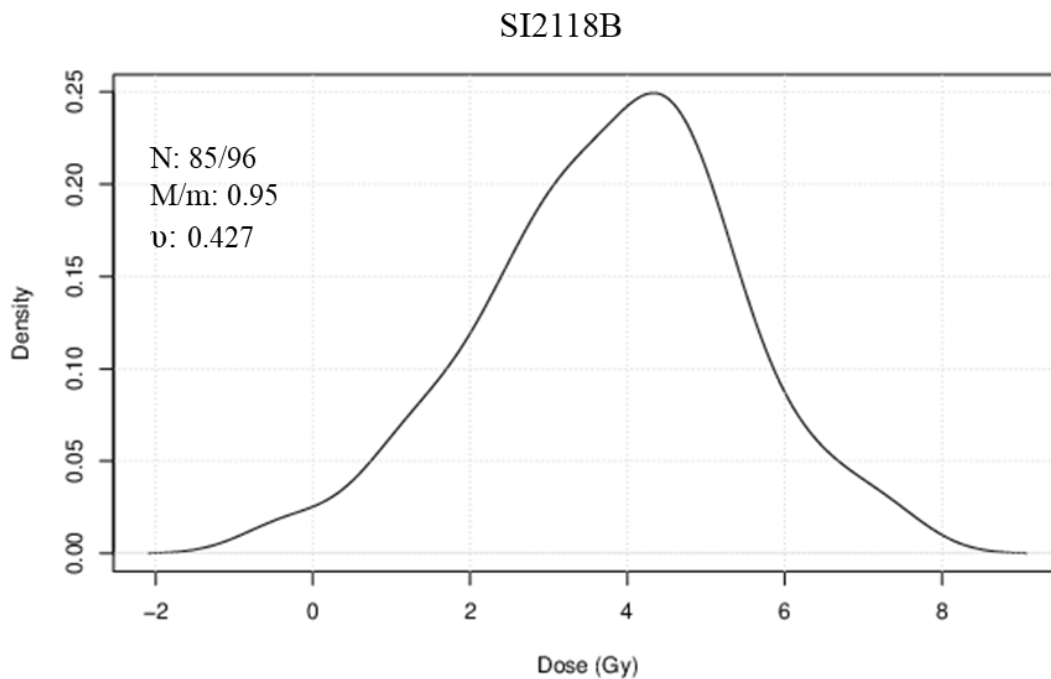
Figure F17. Equivalent dose distribution for sample SI2118B plotted as probability density. Computed by Gaussian kernel density estimation (Wessa, 2015).
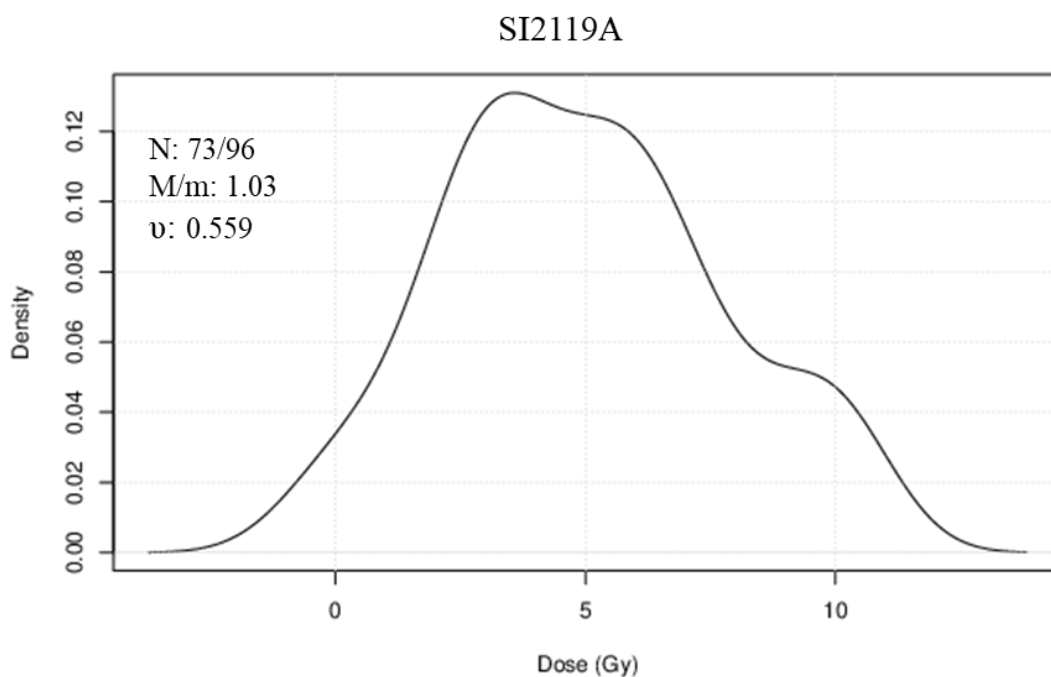
Figure F18. Equivalent dose distribution for sample SI2119A plotted as probability density. Computed by Gaussian kernel density estimation (Wessa, 2015).
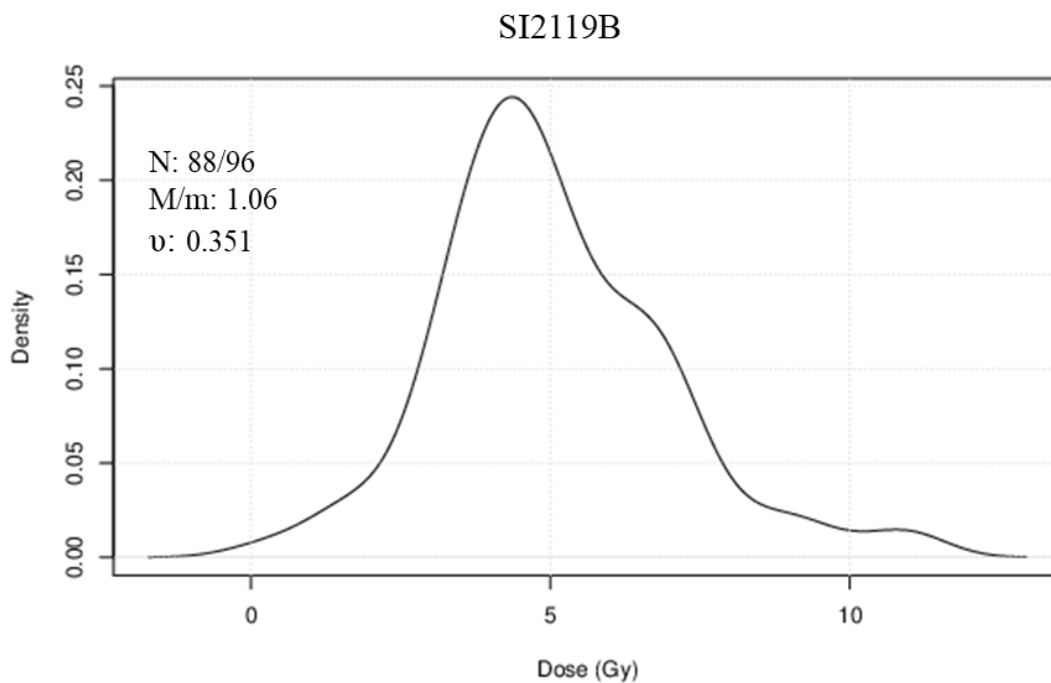
Figure F19. Equivalent dose distribution for sample SI2119B plotted as probability density. Computed by Gaussian kernel density estimation (Wessa, 2015).

APPENDIX G. AGE WORKSHEET DATA

Sample ID SI2007 (150-250 µm)   For samples no greater than 75 cm depth
D' = 0.1005 Gy/s; Calib16

Equivalent Dose Inputs (Gy)   De   se(De)   n   M/m
#1   Mean ± se   0.441   0.030   101/144   1.09
#2   Mean ± se (2.5sd filter)   0.423   0.023   97/144   1.04
#3   Leading edge ± se'
#4
#5

Dose Rate Inputs from INAA

	(ppm) ±	(ppm)	D(beta) ± (mGy/a)	(mGy/a)	D(gamma) ± (mGy/a)	(mGy/a)
K	8222	700	0.643	0.055	0.200	0.017
Rb	24.11	2.84	0.009	0.001	---	---
Th	1.548	0.151	0.042	0.004	0.074	0.007
U	0.563	0.055	0.082	0.008	0.064	0.006

Sample Depth (cm)   28   Depth in cm
Sed./Soil Bulk Density (g/cm3)   2.000 (Aitken, 1998)
Ave. Water Content, (% ± %)   10.0   3.0
Grain Size (range; µm)   150   250
Build-up Factor   1.00
Beta attenuation factor (BAF)   0.89

Cosmic Dose
Surface muon dose rate   0.220   (mGy/a)
Soft and hard component cosmic   0.234   (mGy/a)   This is the difference from the standard calculation.
     (depth*density   56.000)

Dose Rate Outputs / Effective Dose Rates (mGy/a)

	D(beta)	D(gamma)	D(cosmic)	D(totals)	
H2O correction factor	1.125	1.114	1.114		
K	0.509	0.179	-	0.688	BAF confirmed 02/23/12
Rb	0.007	-	-	0.007	
Th	0.033	0.066	-	0.100	
U	0.065	0.057	-	0.122	Dose rate error
Totals	0.614	0.303	0.210	**1.126 mGy/a**	0.098 mGy/a

Error Analysis

	Type	#1	#2	#3	#4	#5
sigma1	ED errors	6.80	5.44	#DIV/0!	#DIV/0!	#DIV/0!
sigma2	Dose rate errors	6.61				
sigma3	Stones in matrix	0.00				
sigma4	Calibaration errors	0.00				
sigma5	Parameter Uncertainties	3.04				
sigma6	U/Th uncertainty from α counting	0.00				
sigma7	Water content estimation errors	3.00				
sigma8	Uncertainty in cosmic ray dose	3.73				
overall 1sigma error (%)		11.05	10.26	#DIV/0!	#DIV/0!	#DIV/0!

Primary Output: SI2007 (150-250 µm)

	De (Gy)	se[De] (Gy)	Dose Rate (mGy/a)	Dose Rate Error (mGy/a)	Age (years)	Uncert. (years)	SE of Age Distribution	Delta Method Error
#1	0.441	0.030	1.126	0.098	391	43	27	43
#2	0.423	0.023	1.126	0.098	376	39	20	39
#3	0.000	0.000	1.126	0.098	0	#DIV/0!	0	0
#4	0.000	0.000	1.126	0.098	0	#DIV/0!	0	0
#5	0.000	0.000	1.126	0.098	0	#DIV/0!	0	0

Figure G1. Age worksheet for SI2007.

Sample ID SI2008 (150-250 microns)   D' = 0.1005 Gy/s; Calib16

Equivalent Dose Inputs (Gy)		De	se(De)	n	M/m
#1	Mean ± se	0.390	0.029	96/144	0.99
#2	Mean ± se (2.5sd filter)	0.418	0.025	93/144	1.03
#3	Leading Edge (DLE±se')				
#4					
#5	Prelim				

Dose Rate Inputs from INAA

	(ppm) ±	(ppm)	D(beta) ± (mGy/a)	(mGy/a)	D(gamma) ± (mGy/a)	(mGy/a)	27-Jul-17
K	4239	363	0.331	0.028	0.103	0.009 √ (Aitken, 1998)
Rb	12.44	2.02	0.005	0.001	---	--- √ (Aitken, 1998)
Th	1.260	0.124	0.034	0.003	0.060	0.006 √ (Aitken, 1998)
U	0.519	0.045	0.075	0.007	0.059	0.005 √ (Aitken, 1998)

Sample Depth (m)	0.770	
Sed./Soil Bulk Density (g/cm3)	2.000	(Aitken, 1998)
Ave. Water Content, (% ± %)	18.0	3.0
Grain Size (range; µm)	150	250
Build-up Factor	1.00	
Beta attenuation factor (BAF)	0.89	

Cosmic Dose

Surface muon dose rate	0.220	(mGy/a)
Coarse grain dating cosmic	0.198	**(mGy/a)**
(depth*density 1.540)		

Dose Rate Outputs / Effective Dose Rates (mGy/a)

	D(beta)	D(gamma)	D(cosmic)	D(totals)	
H2O correction factor	1.225	1.2052	1.2052		
K	0.241	0.085	-	0.326	BAF confirmed 02/23/12
Rb	0.003	-	-	0.003	
Th	0.025	0.050	-	0.075	
U	0.055	0.049	-	0.103	Dose rate error
Totals	0.324	0.184	0.164	**0.672 mGy/a**	0.059 mGy/a

Error Analysis

	Type	#1	#2	#3	#4	#5
sigma1	ED errors	7.44	5.98	#DIV/0!	#DIV/0!	#DIV/0!
sigma2	Dose rate errors	5.96				
sigma3	Stones in matrix	0.00				
sigma4	Calibaration errors	0.00				
sigma5	Parameter Uncertainties	2.77				
sigma6	U/Th uncertainty from α counting	0.00				
sigma7	Water content estimation errors	3.00				
sigma8	Uncertainty in cosmic ray dose	4.88				
overall 1sigma error (%)		11.46	10.57	#DIV/0!	#DIV/0!	#DIV/0!

Primary Output: 0

	De (Gy)	se[De] (Gy)	Dose Rate (mGy/a)	Dose Rate Error (mGy/a)	Age (years)	SE of Age Distribution	Uncert. (years)	Delta Method Error
#1	0.390	0.029	0.672	0.059	580	43	67	67
#2	0.418	0.025	0.672	0.059	622	37	66	66
#3	0.000	0.000	0.672	0.059	0	0	#DIV/0!	0
#4	0.000	0.000	0.672	0.059	0	0	#DIV/0!	0
#5	0.000	0.000	0.672	0.059	0	0	#DIV/0!	0

Figure G2. Age worksheet for SI2008.

Sample ID SI2009 (150-250 microns)   D' = 0.1005 Gy/s; Calib16

	Equivalent Dose Inputs (Gy)	De	se(De)	n	M/m
#1	Mean ± se				
#2	Mean ± se (2.5sd filter)	0.334	0.038	101/144	*0.87*
#3	Mean ± se (KDE filter)	0.397	0.030	95/144	1.01
#4	Leading Edge (DLE±se')				
#5	Prelim				

Dose Rate Inputs from INAA

	(ppm) ±	(ppm)	D(beta) ± (mGy/a)	(mGy/a)	D(gamma) ± (mGy/a)	(mGy/a)	27-Jul-17
K	10553	890	0.825	0.070	0.256	0.022	√ (Aitken, 1998)
Rb	30.79	3.35	0.012	0.001	---	---	√ (Aitken, 1998)
Th	1.797	0.173	0.049	0.005	0.086	0.008	√ (Aitken, 1998)
U	0.503	0.046	0.073	0.007	0.057	0.005	√ (Aitken, 1998)

Sample Depth (m)	0.980	
Sed./Soil Bulk Density (g/cm3)	2.000	(Aitken, 1998)
Ave. Water Content, (% ± %)	15.0	3.0
Grain Size (range; μm)	150	250
Build-up Factor	1.00	
Beta attenuation factor (BAF)	0.89	

Cosmic Dose

Surface muon dose rate	0.220	(mGy/a)
Coarse grain dating cosmic	0.192	**(mGy/a)**
(depth*density 1.960)		

Dose Rate Outputs / Effective Dose Rates (mGy/a)

	D(beta)	D(gamma)	D(cosmic)	D(totals)	
H2O correction factor	1.1875	1.171	1.171		
K	0.618	0.219	-	0.837	BAF confirmed 02/23/12
Rb	0.009	-	-	0.009	
Th	0.037	0.073	-	0.110	
U	0.055	0.049	-	0.103	Dose rate error
Totals	0.719	0.341	0.164	**1.224 mGy/a**	0.105 mGy/a

Error Analysis

	Type	#1	#2	#3	#4	#5
sigma1	ED errors	#DIV/0!	11.38	7.56	#DIV/0!	#DIV/0!
sigma2	Dose rate errors	6.80				
sigma3	Stones in matrix	0.00				
sigma4	Calibration errors	0.00				
sigma5	Parameter Uncertainties	3.25				
sigma6	U/Th uncertainty from α counting	0.00				
sigma7	Water content estimation errors	3.00				
sigma8	Uncertainty in cosmic ray dose	2.68				
	overall 1sigma error (%)	#DIV/0!	14.23	11.41	#DIV/0!	#DIV/0!

Primary Output: 0

	De (Gy)	se[De] (Gy)	Dose Rate (mGy/a)	Dose Rate Error (mGy/a)	Age (years)	SE of Age Distribution	Uncert. (years)	Delta Method Error
#1	0.000	0.000	1.224	0.105	0	0	#DIV/0!	0
#2	0.334	0.038	1.224	0.105	273	31	39	39
#3	0.397	0.030	1.224	0.105	324	25	37	37
#4	0.000	0.000	1.224	0.105	0	0	#DIV/0!	0
#5	0.000	0.000	1.224	0.105	0	0	#DIV/0!	0

Figure G3. Age worksheet for SI2009.

Sample ID SI2010 (150-250 microns)   D' = 0.1005 Gy/s; Calib16

Equivalent Dose Inputs (Gy)		De	se(De)	n	M/m
#1	Mean ± se				
#2	Mean ± se (2.5sd filter)	0.048	0.041	94/144	0.54
#3	Mean ± se (1 Pop Gaus. Fit	0.105	0.011	94/144	0.54
#4					
#5					

Dose Rate Inputs from INAA

	(ppm) ±	(ppm)	D(beta) ± (mGy/a)	(mGy/a)	D(gamma) ± (mGy/a)	(mGy/a)	27-Jul-17
K	5207	441	0.407	0.034	0.127	0.011	√ (Aitken, 1998)
Rb	14.28	2.09	0.005	0.001	---	---	√ (Aitken, 1998)
Th	1.830	0.171	0.050	0.005	0.087	0.008	√ (Aitken, 1998)
U	0.614	0.049	0.089	0.007	0.069	0.006	√ (Aitken, 1998)

Sample Depth (m)	0.750	
Sed./Soil Bulk Density (g/cm3)	2.000	(Aitken, 1998)
Ave. Water Content, (% ± %)	12.0	3.0
Grain Size (range; μm)	150	250
Build-up Factor	1.00	
Beta attenuation factor (BAF)	0.89	

Cosmic Dose

Surface muon dose rate	0.220	(mGy/a)
Coarse grain dating cosmic	0.198	**(mGy/a)**
(depth*density 1.500)		

Dose Rate Outputs / Effective Dose Rates (mGy/a)

	D(beta)	D(gamma)	D(cosmic)	D(totals)	
H2O correction factor	1.15	1.1368	1.1368		
K	0.315	0.111	-	0.426	BAF confirmed 02/23/12
Rb	0.004	-	-	0.004	
Th	0.039	0.077	-	0.115	
U	0.069	0.061	-	0.130	Dose rate error
Totals	0.427	0.249	0.174	**0.850 mGy/a**	0.070 mGy/a

Error Analysis

	Type	#1	#2	#3	#4	#5
sigma1	ED errors	#DIV/0!	85.42	10.48	#DIV/0!	#DIV/0!
sigma2	Dose rate errors	5.78				
sigma3	Stones in matrix	0.00				
sigma4	Calibaration errors	0.00				
sigma5	Parameter Uncertainties	2.91				
sigma6	U/Th uncertainty from α counting	0.00				
sigma7	Water content estimation errors	3.00				
sigma8	Uncertainty in cosmic ray dose	4.10				
	overall 1sigma error (%)	#DIV/0!	85.81	13.32	#DIV/0!	#DIV/0!

Primary Output: 0

	De (Gy)	se[De] (Gy)	Dose Rate (mGy/a)	Dose Rate Error (mGy/a)	Age (years)	SE of Age Distribution	Uncert. (years)	Delta Method Error
#1	0.000	0.000	0.850	0.070	0	0	#DIV/0!	0
#2	0.048	0.041	0.850	0.070	56	48	48	48
#3	0.105	0.011	0.850	0.070	123	13	16	16
#4	0.000	0.000	0.850	0.070	0	0	#DIV/0!	0
#5	0.000	0.000	0.850	0.070	0	0	#DIV/0!	0

Figure G4. Age worksheet for SI2010.

Sample ID SI2011 (250-355 microns)   D' = 0.1005 Gy/s; Calib 16

	Equivalent Dose Inputs (Gy)	De	se(De)	n	M/m
#1	Mean ± se	3.014	0.231	76	1.04
#2	Mean ± se (2.5sd filter)	3.098	0.189	73	1.06
#3	Leading Edge (DLE±se')	1.421	0.119	k=31	1.06
#4					
#5	Prelim				

Dose Rate Inputs from INAA

			D(beta) ±		D(gamma) ±		
	(ppm) ±	(ppm)	(mGy/a)	(mGy/a)	(mGy/a)	(mGy/a)	27-Jul-17
K	7022	496	0.549	0.039	0.171	0.012 √ (Aitken, 1998)
Rb	17.09	2.16	0.006	0.001	---	--- √ (Aitken, 1998)
Th	1.440	0.141	0.039	0.004	0.069	0.007 √ (Aitken, 1998)
U	0.432	0.042	0.063	0.006	0.049	0.005 √ (Aitken, 1998)

Sample Depth (m)	0.570	
Sed./Soil Bulk Density (g/cm3)	2.000	(Aitken, 1998)
Ave. Water Content, (% ± %)	18.0	3.0
Grain Size (range; μm)	250	355
Build-up Factor	1.00	
Beta attenuation factor (BAF)	0.84	

Cosmic Dose

Surface muon dose rate	0.220	(mGy/a)
Coarse grain dating cosmic	0.203	(mGy/a)
(depth*density 1.140)		

Dose Rate Outputs / Effective Dose Rates (mGy/a)

	D(beta)	D(gamma)	D(cosmic)	D(totals)	
H2O correction factor	1.225	1.2052	1.2052		
K	0.377	0.142	-	0.518	BAF confirmed 02/23/12
Rb	0.004	-	-	0.004	
Th	0.027	0.057	-	0.084	
U	0.043	0.041	-	0.083	Dose rate error
Totals	0.451	0.239	0.169	**0.859 mGy/a**	0.069 mGy/a

Error Analysis

	Type	#1	#2	#3	#4	#5
sigma1	ED errors	7.66	6.10	8.37	#DIV/0!	#DIV/0!
sigma2	Dose rate errors	5.56				
sigma3	Stones in matrix	0.00				
sigma4	Calibaration errors	0.00				
sigma5	Parameter Uncertainties	2.97				
sigma6	U/Th uncertainty from α counting	0.00				
sigma7	Water content estimation errors	3.00				
sigma8	Uncertainty in cosmic ray dose	3.93				
	overall 1sigma error (%)	11.09	10.07	11.59	#DIV/0!	#DIV/0!

Primary Output: 0

	De (Gy)	se[De] (Gy)	Dose Rate (mGy/a)	Dose Rate Error (mGy/a)	Age (years)	SE of Age Distribution	Uncert. (years)	Delta Method Error
#1	3.014	0.231	0.859	0.069	3510	269	389	389
#2	3.098	0.189	0.859	0.069	3608	220	363	363
#3	1.421	0.119	0.859	0.069	1655	139	192	192
#4	0.000	0.000	0.859	0.069	0	0	#DIV/0!	0
#5	0.000	0.000	0.859	0.069	0	0	#DIV/0!	0

Figure G5. Age worksheet for SI2011.

Sample ID SI2012 (250-355 microns)   D' = 0.1005 Gy/s; Calib 16

	Equivalent Dose Inputs (Gy)	De	se(De)	n	M/m
#1	Mean ± se	3.346	0.486	79	1.38
#2	Mean ± se (2.5sd filter)	2.707	0.190	77	1.15
#3	Leading Edge (DLE±se')	1.063	0.126	k=17	1.15
#4					
#5	Prelim				

Dose Rate Inputs from INAA

			D(beta) ±		D(gamma) ±		
	(ppm) ±	(ppm)	(mGy/a)	(mGy/a)	(mGy/a)	(mGy/a)	27-Jul-17
K	4616	330	0.361	0.026	0.112	0.008	√ (Aitken, 1998)
Rb	18.59	2.63	0.007	0.001	---	---	√ (Aitken, 1998)
Th	1.618	0.160	0.044	0.004	0.077	0.008	√ (Aitken, 1998)
U	0.436	0.046	0.063	0.007	0.049	0.005	√ (Aitken, 1998)

Sample Depth (m)	0.830	
Sed./Soil Bulk Density (g/cm3)	2.000	(Aitken, 1998)
Ave. Water Content, (% ± %)	15.0	3.0
Grain Size (range; μm)	250	355
Build-up Factor	1.00	
Beta attenuation factor (BAF)	0.84	

Cosmic Dose

Surface muon dose rate	0.220	(mGy/a)
Coarse grain dating cosmic	0.196	(mGy/a)
(depth*density 1.660)		

Dose Rate Outputs / Effective Dose Rates (mGy/a)

	D(beta)	D(gamma)	D(cosmic)	D(totals)	
H2O correction factor	1.1875	1.171	1.171		
K	0.255	0.096	-	0.351	BAF confirmed 02/23/12
Rb	0.005	-	-	0.005	
Th	0.031	0.066	-	0.097	
U	0.045	0.042	-	0.087	Dose rate error
Totals	0.336	0.204	0.167	**0.708 mGy/a**	0.058 mGy/a

Error Analysis

	Type	#1	#2	#3	#4	#5
sigma1	ED errors	14.52	7.02	11.85	#DIV/0!	#DIV/0!
sigma2	Dose rate errors	5.26				
sigma3	Stones in matrix	0.00				
sigma4	Calibaration errors	0.00				
sigma5	Parameter Uncertainties	2.78				
sigma6	U/Th uncertainty from α counting	0.00				
sigma7	Water content estimation errors	3.00				
sigma8	Uncertainty in cosmic ray dose	4.73				
	overall 1sigma error (%)	16.67	10.77	14.40	#DIV/0!	#DIV/0!

Primary Output: 0

	De (Gy)	se[De] (Gy)	Dose Rate (mGy/a)	Dose Rate Error (mGy/a)	Age (years)	SE of Age Distribution	Uncert. (years)	Delta Method Error
#1	3.346	0.486	0.708	0.058	4729	687	788	788
#2	2.707	0.190	0.708	0.058	3826	269	412	412
#3	1.063	0.126	0.708	0.058	1502	178	216	216
#4	0.000	0.000	0.708	0.058	0	0	#DIV/0!	0
#5	0.000	0.000	0.708	0.058	0	0	#DIV/0!	0

Figure G6. Age worksheet for SI2012.

Sample ID SI2013 (150-250 microns)   D' = 0.1005; Calib16

Equivalent Dose Inputs (Gy)		De	se(De)	n	M/m
#1	Mean ± se	3.091	0.154	83/89	1.12
#2	Mean ± se (2.5sd filter)	2.918	0.121	80/89	1.06
#3	Leading Edge (DLE±se')	1.911	0.093	k = 36	1.06
#4					
#5	Prelim				

Dose Rate Inputs from INAA

			D(beta) ±		D(gamma) ±		
	(ppm) ±	(ppm)	(mGy/a)	(mGy/a)	(mGy/a)	(mGy/a)	27-Jul-17
K	6805	576	0.532	0.045	0.165	0.014 √ (Aitken, 1998)
Rb	16.90	2.25	0.006	0.001	---	--- √ (Aitken, 1998)
Th	1.904	0.181	0.052	0.005	0.091	0.009 √ (Aitken, 1998)
U	0.591	0.050	0.086	0.007	0.067	0.006 √ (Aitken, 1998)

Sample Depth (m)	0.670	
Sed./Soil Bulk Density (g/cm3)	2.000	(Aitken, 1998)
Ave. Water Content, (% ± %)	15.0	3.0
Grain Size (range; μm)	150	250
Build-up Factor	1.00	
Beta attenuation factor (BAF)	0.89	

Cosmic Dose

Surface muon dose rate	0.220	(mGy/a)
Coarse grain dating cosmic	0.200	**(mGy/a)**
(depth*density 1.340)		

Dose Rate Outputs / Effective Dose Rates (mGy/a)

	D(beta)	D(gamma)	D(cosmic)	D(totals)	
H2O correction factor	1.1875	1.171	1.171		
K	0.399	0.141	-	0.540	BAF confirmed 02/23/12
Rb	0.005	-	-	0.005	
Th	0.039	0.078	-	0.117	
U	0.064	0.057	-	0.121	Dose rate error
Totals	0.507	0.276	0.171	**0.954 mGy/a**	0.079 mGy/a

Error Analysis

	Type	#1	#2	#3	#4	#5
sigma1	ED errors	4.98	4.15	4.87	#DIV/0!	#DIV/0!
sigma2	Dose rate errors	6.15				
sigma3	Stones in matrix	0.00				
sigma4	Calibaration errors	0.00				
sigma5	Parameter Uncertainties	3.02				
sigma6	U/Th uncertainty from α counting	0.00				
sigma7	Water content estimation errors	3.00				
sigma8	Uncertainty in cosmic ray dose	3.59				
	overall 1sigma error (%)	9.68	9.28	9.62	#DIV/0!	#DIV/0!

Primary Output: 0

	De (Gy)	se[De] (Gy)	Dose Rate (mGy/a)	Dose Rate Error (mGy/a)	Age (years)	SE of Age Distribution	Uncert. (years)	Delta Method Error
#1	3.091	0.154	0.954	0.079	3241	161	314	314
#2	2.918	0.121	0.954	0.079	3059	127	284	284
#3	1.911	0.093	0.954	0.079	2003	98	193	193
#4	0.000	0.000	0.954	0.079	0	0	#DIV/0!	0
#5	0.000	0.000	0.954	0.079	0	0	#DIV/0!	0

Figure G7. Age worksheet for SI2013.

Sample ID SI2014 (150-250 microns)   D' = 0.1005 Gy/s; Calib16

Equivalent Dose Inputs (Gy)		De	se(De)	n	M/m
#1	Mean ± se	4.432	0.143	95/96	1.00
#2	Mean ± se (2.5sd filter)	4.473	0.139	94/96	1.01
#3	Leading Edge (DLE±se')				
#4					
#5	Prelim				

Dose Rate Inputs from INAA

			D(beta) ±		D(gamma) ±		
	(ppm) ±	(ppm)	(mGy/a)	(mGy/a)	(mGy/a)	(mGy/a)	27-Jul-17
K	8695	735	0.680	0.057	0.211	0.018	√ (Aitken, 1998)
Rb	24.29	3.55	0.009	0.001	---	---	√ (Aitken, 1998)
Th	1.512	0.145	0.041	0.004	0.072	0.007	√ (Aitken, 1998)
U	0.516	0.046	0.075	0.007	0.058	0.005	√ (Aitken, 1998)

Sample Depth (m)	0.610	
Sed./Soil Bulk Density (g/cm3)	2.000	(Aitken, 1998)
Ave. Water Content, (% ± %)	33.0	3.0
Grain Size (range; μm)	150	250
Build-up Factor	1.00	
Beta attenuation factor (BAF)	0.89	

Cosmic Dose

Surface muon dose rate	0.220	(mGy/a)
Coarse grain dating cosmic	0.202	**(mGy/a)**
(depth*density 1.220)		

Dose Rate Outputs / Effective Dose Rates (mGy/a)

	D(beta)	D(gamma)	D(cosmic)	D(totals)	
H2O correction factor	1.4125	1.3762	1.3762		
K	0.428	0.154	-	0.582	BAF confirmed 02/23/12
Rb	0.006	-	-	0.006	
Th	0.026	0.052	-	0.078	
U	0.047	0.042	-	0.090	Dose rate error
Totals	0.507	0.248	0.147	**0.903 mGy/a**	0.078 mGy/a

Error Analysis

	Type	#1	#2	#3	#4	#5
sigma1	ED errors	3.23	3.11	#DIV/0!	#DIV/0!	#DIV/0!
sigma2	Dose rate errors	6.67				
sigma3	Stones in matrix	0.00				
sigma4	Calibaration errors	0.00				
sigma5	Parameter Uncertainties	3.13				
sigma6	U/Th uncertainty from α counting	0.00				
sigma7	Water content estimation errors	3.00				
sigma8	Uncertainty in cosmic ray dose	3.25				
	overall 1sigma error (%)	9.18	9.14	#DIV/0!	#DIV/0!	#DIV/0!

Primary Output: 0

	De (Gy)	se[De] (Gy)	Dose Rate (mGy/a)	Dose Rate Error (mGy/a)	Age (years)	SE of Age Distribution	Uncert. (years)	Delta Method Error
#1	4.432	0.143	0.903	0.078	4910	158	451	451
#2	4.473	0.139	0.903	0.078	4956	154	453	453
#3	0.000	0.000	0.903	0.078	0	0	#DIV/0!	0
#4	0.000	0.000	0.903	0.078	0	0	#DIV/0!	0
#5	0.000	0.000	0.903	0.078	0	0	#DIV/0!	0

Figure G8. Age worksheet for SI2014.

Sample ID SI2015A (150-250 microns)   D' = 0.1005 Gy/s; Calib16

Equivalent Dose Inputs (Gy)		De	se(De)	n	M/m
#1	Mean ± se	4.423	0.221	91/96	1.11
#2	Mean ± se (2.5sd filter)	4.263	0.192	89/96	1.07
#3	Leading Edge (DLE±se')	2.782	0.183	k = 27	1.07
#4					
#5	Prelim				

Dose Rate Inputs from INAA

	(ppm) ±	(ppm)	D(beta) ± (mGy/a)	(mGy/a)	D(gamma) ± (mGy/a)	(mGy/a)	27-Jul-17
K	10009	843	0.783	0.066	0.243	0.020	√ (Aitken, 1998)
Rb	29.39	3.60	0.011	0.001	---	---	√ (Aitken, 1998)
Th	2.100	0.199	0.057	0.005	0.100	0.009	√ (Aitken, 1998)
U	1.021	0.078	0.148	0.011	0.115	0.009	√ (Aitken, 1998)

Sample Depth (m)	0.490	
Sed./Soil Bulk Density (g/cm3)	2.000	(Aitken, 1998)
Ave. Water Content, (% ± %)	15.0	3.0
Grain Size (range; μm)	150	250
Build-up Factor	1.00	
Beta attenuation factor (BAF)	0.89	

Cosmic Dose

Surface muon dose rate	0.220	(mGy/a)
Coarse grain dating cosmic	0.206	**(mGy/a)**
(depth*density 0.980)		

Dose Rate Outputs / Effective Dose Rates (mGy/a)

	D(beta)	D(gamma)	D(cosmic)	D(totals)	
H2O correction factor	1.1875	1.171	1.171		
K	0.587	0.208	-	0.794	BAF confirmed 02/23/12
Rb	0.008	-	-	0.008	
Th	0.043	0.086	-	0.129	
U	0.111	0.099	-	0.209	Dose rate error
Totals	0.749	0.392	0.176	**1.316 mGy/a**	0.105 mGy/a

Error Analysis

	Type	#1	#2	#3	#4	#5
sigma1	ED errors	5.00	4.50	6.58	#DIV/0!	#DIV/0!
sigma2	Dose rate errors	6.12				
sigma3	Stones in matrix	0.00				
sigma4	Calibaration errors	0.00				
sigma5	Parameter Uncertainties	3.21				
sigma6	U/Th uncertainty from α counting	0.00				
sigma7	Water content estimation errors	3.00				
sigma8	Uncertainty in cosmic ray dose	2.67				
	overall 1sigma error (%)	9.43	9.18	10.35	#DIV/0!	#DIV/0!

Primary Output: 0

	De (Gy)	se[De] (Gy)	Dose Rate (mGy/a)	Dose Rate Error (mGy/a)	Age (years)	SE of Age Distribution	Uncert. (years)	Delta Method Error
#1	4.423	0.221	1.316	0.105	3360	168	317	317
#2	4.263	0.192	1.316	0.105	3239	146	297	297
#3	2.782	0.183	1.316	0.105	2114	139	219	219
#4	0.000	0.000	1.316	0.105	0	0	#DIV/0!	0
#5	0.000	0.000	1.316	0.105	0	0	#DIV/0!	0

Figure G9. Age worksheet for SI2015A.

Sample ID SI2105B (150-250 microns)   D' = 0.1005; Calib16

	Equivalent Dose Inputs (Gy)	De	se(De)	n	M/m
#1	Mean ± se	3.685	0.215	89/96	1.09
#2	Mean ± se (2.5sd filter)	3.648	0.177	87/96	1.08
#3	Leading Edge (DLE±se')	2.249	0.136	87/96	1.08
#4					
#5	Prelim				

Dose Rate Inputs from INAA

	(ppm) ±	(ppm)	D(beta) ± (mGy/a)	(mGy/a)	D(gamma) ± (mGy/a)	(mGy/a)	27-Jul-17
K	11038	932	0.863	0.073	0.268	0.023	√ (Aitken, 1998)
Rb	33.31	4.01	0.013	0.002	---	---	√ (Aitken, 1998)
Th	1.899	0.186	0.052	0.005	0.091	0.009	√ (Aitken, 1998)
U	0.755	0.064	0.109	0.009	0.085	0.007	√ (Aitken, 1998)

Sample Depth (m)	0.770	
Sed./Soil Bulk Density (g/cm3)	2.000	(Aitken, 1998)
Ave. Water Content, (% ± %)	33.0	3.0
Grain Size (range; μm)	150	250
Build-up Factor	1.00	
Beta attenuation factor (BAF)	0.89	

Cosmic Dose

Surface muon dose rate	0.220	(mGy/a)
Coarse grain dating cosmic	0.198	**(mGy/a)**
(depth*density 1.540)		

Dose Rate Outputs / Effective Dose Rates (mGy/a)

	D(beta)	D(gamma)	D(cosmic)	D(totals)	
H2O correction factor	1.4125	1.3762	1.3762		
K	0.544	0.195	-	0.739	BAF confirmed 02/23/12
Rb	0.008	-	-	0.008	
Th	0.033	0.066	-	0.098	
U	0.069	0.062	-	0.131	Dose rate error
Totals	0.653	0.323	0.144	**1.120 mGy/a**	0.093 mGy/a

Error Analysis

	Type	#1	#2	#3	#4	#5
sigma1	ED errors	5.83	4.85	6.05	#DIV/0!	#DIV/0!
sigma2	Dose rate errors	6.57				
sigma3	Stones in matrix	0.00				
sigma4	Calibration errors	0.00				
sigma5	Parameter Uncertainties	3.25				
sigma6	U/Th uncertainty from α counting	0.00				
sigma7	Water content estimation errors	3.00				
sigma8	Uncertainty in cosmic ray dose	2.57				
	overall 1sigma error (%)	10.16	9.63	10.29	#DIV/0!	#DIV/0!

Primary Output: 0

	De (Gy)	se[De] (Gy)	Dose Rate (mGy/a)	Dose Rate Error (mGy/a)	Age (years)	SE of Age Distribution	Uncert. (years)	Delta Method Error
#1	3.685	0.215	1.120	0.093	3290	192	334	334
#2	3.648	0.177	1.120	0.093	3257	158	314	314
#3	2.249	0.136	1.120	0.093	2008	121	207	207
#4	0.000	0.000	1.120	0.093	0	0	#DIV/0!	0
#5	0.000	0.000	1.120	0.093	0	0	#DIV/0!	0

Figure G10. Age worksheet for SI2015B.

Sample ID SI2016 (150-250 microns)   D' = 0.1005 Gy/s; CAlib16

Equivalent Dose Inputs (Gy)		De	se(De)	n	M/m
#1	Mean ± se	4.146	0.241	95/96	1.13
#2	Mean ± se (2.5sd filter)	4.035	0.198	92/95	1.10
#3	Leading Edge (DLE±se')	3.664	0.150	K = 65	1.10
#4					
#5	Prelim				

Dose Rate Inputs from INAA

	(ppm) ±	(ppm)	D(beta) ± (mGy/a)	(mGy/a)	D(gamma) ± (mGy/a)	(mGy/a)	27-Jul-17
K	11873	1002	0.928	0.078	0.289	0.024	√ (Aitken, 1998)
Rb	34.13	4.29	0.013	0.002	---	---	√ (Aitken, 1998)
Th	2.633	0.249	0.072	0.007	0.126	0.012	√ (Aitken, 1998)
U	0.596	0.055	0.086	0.008	0.067	0.006	√ (Aitken, 1998)

Sample Depth (m)	0.720	
Sed./Soil Bulk Density (g/cm3)	2.000	(Aitken, 1998)
Ave. Water Content, (% ± %)	15.0	3.0
Grain Size (range; µm)	150	250
Build-up Factor	1.00	
Beta attenuation factor (BAF)	0.89	

Cosmic Dose

Surface muon dose rate	0.220	(mGy/a)
Coarse grain dating cosmic	0.199	(mGy/a)
(depth*density 1.440)		

Dose Rate Outputs / Effective Dose Rates (mGy/a)

	D(beta)	D(gamma)	D(cosmic)	D(totals)	
H2O correction factor	1.1875	1.171	1.171		
K	0.696	0.246	-	0.942	BAF confirmed 02/23/12
Rb	0.010	-	-	0.010	
Th	0.054	0.107	-	0.161	
U	0.065	0.058	-	0.122	Dose rate error
Totals	0.824	0.411	0.170	**1.405 mGy/a**	0.117 mGy/a

Error Analysis

	Type	#1	#2	#3	#4	#5
sigma1	ED errors	5.81	4.91	4.09	#DIV/0!	#DIV/0!
sigma2	Dose rate errors	6.62				
sigma3	Stones in matrix	0.00				
sigma4	Calibaration errors	0.00				
sigma5	Parameter Uncertainties	3.28				
sigma6	U/Th uncertainty from α counting	0.00				
sigma7	Water content estimation errors	3.00				
sigma8	Uncertainty in cosmic ray dose	2.42				
	overall 1sigma error (%)	10.16	9.67	9.28	#DIV/0!	#DIV/0!

Primary Output: 0

	De (Gy)	se[De] (Gy)	Dose Rate (mGy/a)	Dose Rate Error (mGy/a)	Age (years)	SE of Age Distribution	Uncert. (years)	Delta Method Error
#1	4.146	0.241	1.405	0.117	2950	171	300	300
#2	4.035	0.198	1.405	0.117	2871	141	278	278
#3	3.664	0.150	1.405	0.117	2607	107	242	242
#4	0.000	0.000	1.405	0.117	0	0	#DIV/0!	0
#5	0.000	0.000	1.405	0.117	0	0	#DIV/0!	0

Figure G11. Age worksheet for SI2016.

Sample ID SI2017 (150-250 microns) D' = 0.1005 Gy/s; Calib 16

	Equivalent Dose Inputs (Gy)	De	se(De)	n	M/m
#1	Mean ± se	4.732	0.272	88	1.06
#2	Mean ± se (2.5sd filter)	4.473	0.194	86	1.03
#3	Leading Edge (DLE±se')				
#4					
#5	Prelim				

Dose Rate Inputs from INAA

	(ppm) ±	(ppm)	D(beta) ± (mGy/a)	(mGy/a)	D(gamma) ± (mGy/a)	(mGy/a)	27-Jul-17
K	9669	622	0.756	0.049	0.235	0.015	√ (Aitken, 1998)
Rb	34.37	3.60	0.013	0.001	---	---	√ (Aitken, 1998)
Th	2.117	0.207	0.058	0.006	0.101	0.010	√ (Aitken, 1998)
U	0.611	0.056	0.089	0.008	0.069	0.006	√ (Aitken, 1998)

Sample Depth (m)	0.660
Sed./Soil Bulk Density (g/cm3)	2.000 (Aitken, 1998)
Ave. Water Content, (% ± %)	12.0 3.0
Grain Size (range; μm)	150 250
Build-up Factor	1.00
Beta attenuation factor (BAF)	0.89

Cosmic Dose

Surface muon dose rate	0.220	(mGy/a)
Coarse grain dating	cosmic	0.201	**(mGy/a)**
(depth*density	1.320)	

Dose Rate Outputs / Effective Dose Rates (mGy/a)

	D(beta)	D(gamma)	D(cosmic)	D(totals)	
H2O correction factor	1.15	1.1368	1.1368		
K	0.585	0.207	-	0.792	BAF confirmed 02/23/12
Rb	0.010	-	-	0.010	
Th	0.045	0.089	-	0.134	
U	0.069	0.061	-	0.129	Dose rate error
Totals	0.709	0.356	0.177	**1.241 mGy/a**	0.090 mGy/a

Error Analysis

	Type	#1	#2	#3	#4	#5
sigma1	ED errors	5.75	4.34	#DIV/0!	#DIV/0!	#DIV/0!
sigma2	Dose rate errors	5.06				
sigma3	Stones in matrix	0.00				
sigma4	Calibration errors	0.00				
sigma5	Parameter Uncertainties	3.19				
sigma6	U/Th uncertainty from α counting	0.00				
sigma7	Water content estimation errors	3.00				
sigma8	Uncertainty in cosmic ray dose	2.85				
	overall 1sigma error (%)	9.27	8.47	#DIV/0!	#DIV/0!	#DIV/0!

Primary Output: 0

	De (Gy)	se[De] (Gy)	Dose Rate (mGy/a)	Dose Rate Error (mGy/a)	Age (years)	SE of Age Distribution	Uncert. (years)	Delta Method Error
#1	4.732	0.272	1.241	0.090	3812	219	353	353
#2	4.473	0.194	1.241	0.090	3603	156	305	305
#3	0.000	0.000	1.241	0.090	0	0	#DIV/0!	0
#4	0.000	0.000	1.241	0.090	0	0	#DIV/0!	0
#5	0.000	0.000	1.241	0.090	0	0	#DIV/0!	0

Figure G12. Age worksheet for SI2017.

Sample ID SI2018 (150-250 microns)   D' = 0.1005 Gy/s; Calib 16

Equivalent Dose Inputs (Gy)

		De	se(De)	n	M/m
#1	Mean ± se	3.823	0.158	93	1.00
#2	Mean ± se (2.5sd filter)	3.727	0.146	98	0.98
#3	Leading Edge (DLE±se')				
#4					
#5	Prelim				

Dose Rate Inputs from INAA

				D(beta) ±		D(gamma) ±		
	(ppm) ±	(ppm)		(mGy/a)	(mGy/a)	(mGy/a)	(mGy/a)	27-Jul-17
K	7139	357		0.558	0.028	0.173	0.009	√ (Aitken, 1998)
Rb	23.30	2.33		0.009	0.001	---	---	√ (Aitken, 1998)
Th	1.670	0.167		0.046	0.005	0.080	0.008	√ (Aitken, 1998)
U	0.600	0.060		0.087	0.009	0.068	0.007	√ (Aitken, 1998)

Sample Depth (m)	0.770	
Sed./Soil Bulk Density (g/cm3)	2.000	(Aitken, 1998)
Ave. Water Content, (% ± %)	12.0	3.0
Grain Size (range; μm)	150	250
Build-up Factor	1.00	
Beta attenuation factor (BAF)	0.89	

Cosmic Dose

Surface muon dose rate	0.220	(mGy/a)
Coarse grain dating cosmic	0.198	**(mGy/a)**
(depth*density 1.540)		

Dose Rate Outputs / Effective Dose Rates (mGy/a)

	D(beta)	D(gamma)	D(cosmic)	D(totals)	
H2O correction factor	1.15	1.1368	1.1368		
K	0.532	0.188	-	0.720	BAF confirmed 02/23/12
Rb	0.007	-	-	0.007	
Th	0.038	0.075	-	0.113	
U	0.068	0.060	-	0.127	Dose rate error
Totals	0.644	0.323	0.174	**1.141 mGy/a**	0.090 mGy/a

Error Analysis

	Type	#1	#2	#3	#4	#5
sigma1	ED errors	4.13	3.92	#DIV/0!	#DIV/0!	#DIV/0!
sigma2	Dose rate errors	5.79				
sigma3	Stones in matrix	0.00				
sigma4	Calibaration errors	0.00				
sigma5	Parameter Uncertainties	3.16				
sigma6	U/Th uncertainty from α counting	0.00				
sigma7	Water content estimation errors	3.00				
sigma8	Uncertainty in cosmic ray dose	3.05				
overall 1sigma error (%)		8.88	8.78	#DIV/0!	#DIV/0!	#DIV/0!

Primary Output: 0

	De (Gy)	se[De] (Gy)	Dose Rate (mGy/a)	Dose Rate Error (mGy/a)	Age (years)	SE of Age Distribution	Uncert. (years)	Delta Method Error
#1	3.823	0.158	0.998	0.069	3831	158	307	307
#2	3.727	0.146	0.998	0.069	3735	146	295	295
#3	0.000	0.000	0.998	0.069	0	0	#DIV/0!	0
#4	0.000	0.000	0.998	0.069	0	0	#DIV/0!	0
#5	0.000	0.000	0.998	0.069	0	0	#DIV/0!	0

Figure G13. Age worksheet for SI2018.

Sample ID SI2116 (150-250 microns)   D' = 0.0989 Gy/s; Calib 16

Equivalent Dose Inputs (Gy)		De	se(De)	n	M/m
#1	Mean ± se	5.339	0.305	88	1.08
#2	Mean ± se (2.5sd filter)	5.139	0.233	87	1.05
#3	Leading Edge (DLE±se')				
#4					
#5	Prelim				

Dose Rate Inputs from INAA

	(ppm) ±	(ppm)	D(beta) ± (mGy/a)	(mGy/a)	D(gamma) ± (mGy/a)	(mGy/a)	27-Jul-17
K	10344	832	0.809	0.065	0.251	0.020 √ (Aitken, 1998)
Rb	35.16	3.36	0.013	0.001	---	--- √ (Aitken, 1998)
Th	2.922	0.279	0.080	0.008	0.139	0.013 √ (Aitken, 1998)
U	1.195	0.109	0.173	0.016	0.135	0.012 √ (Aitken, 1998)

Sample Depth (m)	0.550	
Sed./Soil Bulk Density (g/cm3)	2.000 (Aitken, 1998)	
Ave. Water Content, (% ± %)	12.0	3.0
Grain Size (range; μm)	150	250
Build-up Factor	1.00	
Beta attenuation factor (BAF)	0.89	

Cosmic Dose

Surface muon dose rate	0.220	(mGy/a)
Coarse grain dating cosmic	0.204	**(mGy/a)**
(depth*density 1.100)		

Dose Rate Outputs / Effective Dose Rates (mGy/a)

	D(beta)	D(gamma)	D(cosmic)	D(totals)	
H2O correction factor	1.15	1.1368	1.1368		
K	0.626	0.221	-	0.847	BAF confirmed 02/23/12
Rb	0.010	-	-	0.010	
Th	0.062	0.123	-	0.184	
U	0.134	0.119	-	0.253	Dose rate error
Totals	0.832	0.463	0.179	**1.474 mGy/a**	0.112 mGy/a

Error Analysis

	Type	#1	#2	#3	#4	#5
sigma1	ED errors	5.71	4.53	#DIV/0!	#DIV/0!	#DIV/0!
sigma2	Dose rate errors	5.72				
sigma3	Stones in matrix	0.00				
sigma4	Calibration errors	0.00				
sigma5	Parameter Uncertainties	3.23				
sigma6	U/Th uncertainty from α counting	0.00				
sigma7	Water content estimation errors	3.00				
sigma8	Uncertainty in cosmic ray dose	2.43				
overall 1sigma error (%)		9.52	8.87	#DIV/0!	#DIV/0!	#DIV/0!

Primary Output: **0**

	De (Gy)	se[De] (Gy)	Dose Rate (mGy/a)	Dose Rate Error (mGy/a)	Age (years)	SE of Age Distribution	Uncert. (years)	Delta Method Error
#1	5.339	0.305	1.474	0.112	3622	207	345	345
#2	5.139	0.233	1.474	0.112	3486	158	309	309
#3	0.000	0.000	1.474	0.112	0	0	#DIV/0!	0
#4	0.000	0.000	1.474	0.112	0	0	#DIV/0!	0
#5	0.000	0.000	1.474	0.112	0	0	#DIV/0!	0

Figure G14. Age worksheet for SI2116.

Sample ID SI2117 (150-250 microns)   D' = 0.0989 Gy/s; Calib 16

Equivalent Dose Inputs (Gy)		De	se(De)	n	M/m
#1	Mean ± se	5.981	0.564	87	1.17
#2	Mean ± se (2.5sd filter)	5.222	0.267	84	1.05
#3	Leading Edge (DLE±se')				
#4					
#5	Prelim				

Dose Rate Inputs from INAA

	(ppm) ±	(ppm)	D(beta) ± (mGy/a)	(mGy/a)	D(gamma) ± (mGy/a)	(mGy/a)	27-Jul-17
K	9849	785	0.770	0.061	0.239	0.019	√ (Aitken, 1998)
Rb	33.56	3.21	0.013	0.001	---	---	√ (Aitken, 1998)
Th	2.242	0.215	0.061	0.006	0.107	0.010	√ (Aitken, 1998)
U	0.838	0.087	0.122	0.013	0.095	0.010	√ (Aitken, 1998)

Sample Depth (m)	0.590	
Sed./Soil Bulk Density (g/cm3)	2.000	(Aitken, 1998)
Ave. Water Content, (% ± %)	10.0	3.0
Grain Size (range; μm)	150	250
Build-up Factor	1.00	
Beta attenuation factor (BAF)	0.89	

Cosmic Dose

Surface muon dose rate	0.220	(mGy/a)
Coarse grain dating cosmic	0.203	(mGy/a)
(depth*density 1.180)		

Dose Rate Outputs / Effective Dose Rates (mGy/a)

	D(beta)	D(gamma)	D(cosmic)	D(totals)	
H2O correction factor	1.125	1.114	1.114		
K	0.609	0.215	-	0.824	BAF confirmed 02/23/12
Rb	0.010	-	-	0.010	
Th	0.048	0.096	-	0.144	
U	0.096	0.085	-	0.181	Dose rate error
Totals	0.764	0.396	0.182	**1.342 mGy/a**	0.106 mGy/a

Error Analysis

	Type	#1	#2	#3	#4	#5
sigma1	ED errors	9.43	5.11	#DIV/0!	#DIV/0!	#DIV/0!
sigma2	Dose rate errors	6.01				
sigma3	Stones in matrix	0.00				
sigma4	Calibaration errors	0.00				
sigma5	Parameter Uncertainties	3.21				
sigma6	U/Th uncertainty from α counting	0.00				
sigma7	Water content estimation errors	3.00				
sigma8	Uncertainty in cosmic ray dose	2.71				
overall 1sigma error (%)		12.32	9.43	#DIV/0!	#DIV/0!	#DIV/0!

Primary Output: **0**

	De (Gy)	se[De] (Gy)	Dose Rate (mGy/a)	Dose Rate Error (mGy/a)	Age (years)	SE of Age Distribution	Uncert. (years)	Delta Method Error
#1	5.981	0.564	1.342	0.106	4458	420	549	549
#2	5.222	0.267	1.342	0.106	3892	199	367	367
#3	0.000	0.000	1.342	0.106	0	0	#DIV/0!	0
#4	0.000	0.000	1.342	0.106	0	0	#DIV/0!	0
#5	0.000	0.000	1.342	0.106	0	0	#DIV/0!	0

Figure G15. Age worksheet for SI2117.

Sample ID SI2118A (150-250 microns)   D' = 0.0989 Gy/s; Calib 16

	Equivalent Dose Inputs (Gy)	De	se(De)	n	M/m
#1	Mean ± se	5.280	0.281	93	1.10
#2	Mean ± se (2.5sd filter)	5.066	0.184	92	1.05
#3	Leading Edge (DLE±se')				
#4					
#5	Prelim				

Dose Rate Inputs from INAA

			D(beta) ±		D(gamma) ±		
	(ppm) ±	(ppm)	(mGy/a)	(mGy/a)	(mGy/a)	(mGy/a)	27-Jul-17
K	9408	820	0.736	0.064	0.229	0.020	√ (Aitken, 1998)
Rb	32.54	3.09	0.012	0.001	---	---	√ (Aitken, 1998)
Th	2.488	0.236	0.068	0.006	0.119	0.011	√ (Aitken, 1998)
U	0.689	0.073	0.100	0.011	0.078	0.008	√ (Aitken, 1998)

Sample Depth (m)	0.620	
Sed./Soil Bulk Density (g/cm3)	2.000	(Aitken, 1998)
Ave. Water Content, (% ± %)	12.0	3.0
Grain Size (range; μm)	150	250
Build-up Factor	1.00	
Beta attenuation factor (BAF)	0.89	

Cosmic Dose

Surface muon dose rate	0.220	(mGy/a)
Coarse grain dating cosmic	0.202	**(mGy/a)**
(depth*density 1.240)		

Dose Rate Outputs / Effective Dose Rates (mGy/a)

	D(beta)	D(gamma)	D(cosmic)	D(totals)	
H2O correction factor	1.15	1.1368	1.1368		
K	0.569	0.201	-	0.770	BAF confirmed 02/23/12
Rb	0.010	-	-	0.010	
Th	0.053	0.104	-	0.157	
U	0.077	0.068	-	0.146	Dose rate error
Totals	0.709	0.374	0.178	**1.260 mGy/a**	0.105 mGy/a

Error Analysis

	Type	#1	#2	#3	#4	#5
sigma1	ED errors	5.32	3.63	#DIV/0!	#DIV/0!	#DIV/0!
sigma2	Dose rate errors	6.51				
sigma3	Stones in matrix	0.00				
sigma4	Calibaration errors	0.00				
sigma5	Parameter Uncertainties	3.18				
sigma6	U/Th uncertainty from α counting	0.00				
sigma7	Water content estimation errors	3.00				
sigma8	Uncertainty in cosmic ray dose	2.82				
overall 1sigma error (%)		9.89	9.09	#DIV/0!	#DIV/0!	#DIV/0!

Primary Output: **0**

	De (Gy)	se[De] (Gy)	Dose Rate (mGy/a)	Dose Rate Error (mGy/a)	Age (years)	SE of Age Distribution	Uncert. (years)	Delta Method Error
#1	5.280	0.281	1.260	0.105	4189	223	414	414
#2	5.066	0.184	1.260	0.105	4019	146	365	365
#3	0.000	0.000	1.260	0.105	0	0	#DIV/0!	0
#4	0.000	0.000	1.260	0.105	0	0	#DIV/0!	0
#5	0.000	0.000	1.260	0.105	0	0	#DIV/0!	0

Figure G16. Age worksheet for SI2118A.

110

Sample ID SI2118B (150-250 microns) D' = 0.0989 Gy/s; Calib 16

Equivalent Dose Inputs (Gy)		De	se(De)	n	M/m
#1	Mean ± se	3.849	0.250	87	0.96
#2	Mean ± se (2.5sd filter)	3.776	0.175	85	0.95
#3	Leading Edge (DLE±se')				
#4					
#5	Prelim				

Dose Rate Inputs from INAA

	(ppm) ±	(ppm)	D(beta) ± (mGy/a)	(mGy/a)	D(gamma) ± (mGy/a)	(mGy/a)	27-Jul-17
K	6762	532	0.529	0.042	0.164	0.013	√ (Aitken, 1998)
Rb	23.12	2.22	0.009	0.001	---	---	√ (Aitken, 1998)
Th	1.846	0.178	0.050	0.005	0.088	0.008	√ (Aitken, 1998)
U	0.550	0.058	0.080	0.008	0.062	0.007	√ (Aitken, 1998)

Sample Depth (m)	1.070	
Sed./Soil Bulk Density (g/cm3)	2.000	(Aitken, 1998)
Ave. Water Content, (% ± %)	10.0	3.0
Grain Size (range; μm)	150	250
Build-up Factor	1.00	
Beta attenuation factor (BAF)	0.89	

Cosmic Dose

Surface muon dose rate	0.220	(mGy/a)
Coarse grain dating cosmic	0.190	(mGy/a)
(depth*density 2.140)		

Dose Rate Outputs / Effective Dose Rates (mGy/a)

	D(beta)	D(gamma)	D(cosmic)	D(totals)	
H2O correction factor	1.125	1.114	1.114		
K	0.418	0.148	-	0.566	BAF confirmed 02/23/12
Rb	0.007	-	-	0.007	
Th	0.040	0.079	-	0.119	
U	0.063	0.056	-	0.119	Dose rate error
Totals	0.528	0.282	0.170	**0.981 mGy/a**	0.079 mGy/a

Error Analysis

	Type	#1	#2	#3	#4	#5
sigma1	ED errors	6.50	4.63	#DIV/0!	#DIV/0!	#DIV/0!
sigma2	Dose rate errors	5.88				
sigma3	Stones in matrix	0.00				
sigma4	Calibration errors	0.00				
sigma5	Parameter Uncertainties	3.05				
sigma6	U/Th uncertainty from α counting	0.00				
sigma7	Water content estimation errors	3.00				
sigma8	Uncertainty in cosmic ray dose	3.47				
	overall 1sigma error (%)	10.35	9.30	#DIV/0!	#DIV/0!	#DIV/0!

Primary Output: 0

	De (Gy)	se[De] (Gy)	Dose Rate (mGy/a)	Dose Rate Error (mGy/a)	Age (years)	SE of Age Distribution	Uncert. (years)	Delta Method Error
#1	3.849	0.250	0.981	0.079	3924	255	406	406
#2	3.776	0.175	0.981	0.079	3849	178	358	358
#3	0.000	0.000	0.981	0.079	0	0	#DIV/0!	0
#4	0.000	0.000	0.981	0.079	0	0	#DIV/0!	0
#5	0.000	0.000	0.981	0.079	0	0	#DIV/0!	0

Figure G17. Age worksheet for SI2118B.

Sample ID SI2119A (150-250 microns)　　　　　　　　D' = 0.0989 Gy/s; Calib 16

Equivalent Dose Inputs (Gy)		De	se(De)	n	M/m
#1	Mean ± se	5.080	0.336	74	1.03
#2	Mean ± se (2.5sd filter)	4.978	0.324	73	1.03
#3	Leading Edge (DLE±se')				
#4					
#5	Prelim				

Dose Rate Inputs from INAA

			D(beta) ±		D(gamma) ±		
	(ppm) ±	(ppm)	(mGy/a)	(mGy/a)	(mGy/a)	(mGy/a)	27-Jul-17
K	13288	1018	1.039	0.080	0.323	0.025 √ (Aitken, 1998)
Rb	44.44	4.27	0.017	0.002	---	--- √ (Aitken, 1998)
Th	2.224	0.214	0.061	0.006	0.106	0.010 √ (Aitken, 1998)
U	0.773	0.076	0.112	0.011	0.087	0.009 √ (Aitken, 1998)

Sample Depth (m)	0.760	
Sed./Soil Bulk Density (g/cm3)	2.000	(Aitken, 1998)
Ave. Water Content, (% ± %)	12.0	3.0
Grain Size (range; μm)	150	250
Build-up Factor	1.00	
Beta attenuation factor (BAF)	0.89	

Cosmic Dose

Surface muon dose rate	0.220	(mGy/a)
Coarse grain dating　cosmic	0.198	**(mGy/a)**
(depth*density　1.520)		

Dose Rate Outputs / Effective Dose Rates (mGy/a)

	D(beta)	D(gamma)	D(cosmic)	D(totals)	
H2O correction factor	1.15	1.1368	1.1368		
K	0.804	0.284	-	1.088	BAF confirmed 02/23/12
Rb	0.013	-	-	0.013	
Th	0.047	0.093	-	0.140	
U	0.087	0.077	-	0.164	Dose rate error
Totals	0.951	0.454	0.174	**1.579 mGy/a**	0.125 mGy/a

Error Analysis

	Type	#1	#2	#3	#4	#5
sigma1	ED errors	6.61	6.51	#DIV/0!	#DIV/0!	#DIV/0!
sigma2	Dose rate errors	6.12				
sigma3	Stones in matrix	0.00				
sigma4	Calibaration errors	0.00				
sigma5	Parameter Uncertainties	3.34				
sigma6	U/Th uncertainty from α counting	0.00				
sigma7	Water content estimation errors	3.00				
sigma8	Uncertainty in cosmic ray dose	2.21				
	overall 1sigma error (%)	10.30	10.24	#DIV/0!	#DIV/0!	#DIV/0!

Primary Output:　　　　　　　　　　　　　**0**

	De (Gy)	se[De] (Gy)	Dose Rate (mGy/a)	Dose Rate Error (mGy/a)	Age (years)	SE of Age Distribution	Uncert. (years)	Delta Method Error
#1	5.080	0.336	1.579	0.125	3216	213	331	331
#2	4.978	0.324	1.579	0.125	3152	205	323	323
#3	0.000	0.000	1.579	0.125	0	0	#DIV/0!	0
#4	0.000	0.000	1.579	0.125	0	0	#DIV/0!	0
#5	0.000	0.000	1.579	0.125	0	0	#DIV/0!	0

Figure G18. Age worksheet for SI2119A.

Sample ID SI2119B (150-250 microns)   D' = 0.0989 Gy/s; Calib 16

Equivalent Dose Inputs (Gy)		De	se(De)	n	M/m
#1	Mean ± se	5.242	0.280	92	1.13
#2	Mean ± se (2.5sd filter)	5.031	0.205	88	1.06
#3	Leading Edge (DLE±se')				
#4					
#5	Prelim				

Dose Rate Inputs from INAA

	(ppm) ±	(ppm)	D(beta) ± (mGy/a)	(mGy/a)	D(gamma) ± (mGy/a)	(mGy/a)	27-Jul-17
K	13761	1076	1.076	0.084	0.334	0.026	√ (Aitken, 1998)
Rb	46.24	4.43	0.018	0.002	---	---	√ (Aitken, 1998)
Th	2.049	0.197	0.056	0.005	0.098	0.009	√ (Aitken, 1998)
U	0.653	0.068	0.095	0.010	0.074	0.008	√ (Aitken, 1998)

Sample Depth (m)	0.760	
Sed./Soil Bulk Density (g/cm3)	2.000	(Aitken, 1998)
Ave. Water Content, (% ± %)	12.0	3.0
Grain Size (range; μm)	150	250
Build-up Factor	1.00	
Beta attenuation factor (BAF)	0.89	

Cosmic Dose

Surface muon dose rate	0.220	(mGy/a)
Coarse grain dating cosmic	0.198	(mGy/a)
(depth*density 1.520)		

Dose Rate Outputs / Effective Dose Rates (mGy/a)

	D(beta)	D(gamma)	D(cosmic)	D(totals)	
H2O correction factor	1.15	1.1368	1.1368		
K	0.833	0.294	-	1.127	BAF confirmed 02/23/12
Rb	0.014	-	-	0.014	
Th	0.043	0.086	-	0.129	
U	0.073	0.065	-	0.138	Dose rate error
Totals	0.963	0.445	0.174	**1.582 mGy/a**	0.129 mGy/a

Error Analysis

	Type	#1	#2	#3	#4	#5
sigma1	ED errors	5.34	4.07	#DIV/0!	#DIV/0!	#DIV/0!
sigma2	Dose rate errors	6.40				
sigma3	Stones in matrix	0.00				
sigma4	Calibaration errors	0.00				
sigma5	Parameter Uncertainties	3.35				
sigma6	U/Th uncertainty from α counting	0.00				
sigma7	Water content estimation errors	3.00				
sigma8	Uncertainty in cosmic ray dose	2.20				
	overall 1sigma error (%)	9.73	9.09	#DIV/0!	#DIV/0!	#DIV/0!

Primary Output: 0

	De (Gy)	se[De] (Gy)	Dose Rate (mGy/a)	Dose Rate Error (mGy/a)	Age (years)	SE of Age Distribution	Uncert. (years)	Delta Method Error
#1	5.242	0.280	1.582	0.129	3313	177	322	322
#2	5.031	0.205	1.582	0.129	3180	130	289	289
#3	0.000	0.000	1.582	0.129	0	0	#DIV/0!	0
#4	0.000	0.000	1.582	0.129	0	0	#DIV/0!	0
#5	0.000	0.000	1.582	0.129	0	0	#DIV/0!	0

Figure G19. Age worksheet for SI2119B.